National Aeronautics and Space Administration

Design and Testing of a Prototype Lunar or Planetary Surface Landing Research Vehicle *(LPSLRV)*

An Engineering Senior Design Capstone Course Sponsored by the NASA Office of Education, the NASA Exploration Mission Directorate (ESMD), and the NASA Space Grant Consortium

Course Handbook, Academic Year 2009-2010

Utah State University, Department of Mechanical and Aerospace Engineering
UMC 4130, Logan UT 84322-4130

Instructor: Stephen A. Whitmore
Instructor Phone: 435-797-2951
Instructor Email: Stephen.whitmore@usu.edu
Office: ENGR 419F

Abstract

This handbook describes a two-semester senior design course sponsored by the NASA Office of Education, the Exploration Systems Mission Directorate (ESMD), and the NASA Space Grant Consortium. The course was developed and implemented by the Mechanical and Aerospace Engineering Department (MAE) at Utah State University. The course final outcome is a packaged senior design course that can be readily incorporated into the instructional curriculum at universities across the country. The course materials adhere to the standards of the Accreditation Board for Engineering and Technology (ABET), and is constructed to be relevant to key research areas identified by ESMD.

The design project challenged students to apply systems engineering concepts to define research and training requirements for a terrestrial-based lunar landing simulator. This project developed a flying prototype for a Lunar or Planetary Surface Landing Research Vehicle *(LPSRV)*. Per NASA specifications the concept accounts for reduced lunar gravity, and allows the terminal stage of lunar descent to be flown either by remote pilot or autonomously. This free-flying platform was designed to be sufficiently-flexible to allow both sensor evaluation and pilot training.

This handbook outlines the course materials, describes the systems engineering processes developed to facilitate design fabrication, integration, and testing. This handbook presents sufficient details of the final design configuration to allow an independent group to reproduce the design. The design evolution and details regarding the verification testing used to characterize the system are presented in a separate project final design report. Details of

the experimental apparatus used for system characterization may be found in Appendix F, G, and I of that report. A brief summary of the ground testing and systems verification is also included in Appendix A of this report. Details of the flight tests will be documented in a separate flight test report. This flight test report serves as a complement to the course handbook presented here.

This project was extremely ambitious, and achieving all of the design and test objectives was a daunting task. The schedule ran slightly longer than a single academic year with the complete design closure not occurring until early April. Integration and verification testing spilled over into late May and the first flight did not occur until mid to late June. The academic year at Utah State University ended on May 8, 2010. Following the end of the academic year, testing and integration was performed by the faculty advisor, paid research assistants, and volunteer student help.

Table of Contents

List of Tables

List of Figures

I.

I. Introduction

The Accreditation Board for Engineering and Technology, Inc. (ABET) is recognized by the U.S. Government as the accreditation organization for higher-education programs in applied sciences, engineering, and technology. In the year 2000 ABET established a new program for accreditation review termed Engineering Criteria 2000" (EC2000), EC2000 changed the review perspective from qualitative evaluation to one based on program-defined missions, outcomes, and objectives. The primary EC2000 emphasis is on program "outcomes."

A. ABET Benchmark Criteria

A major content of EC2000 for academic year 2009-2010 is the list of 9 "criteria" that are used to benchmark an academic program for certification. These criteria are [1]

1. *Students*
2. *Program Educational Objectives*
3. *Program Outcomes*
4. *Continuous Improvement*
5. *Curriculum*
6. *Faculty*
7. *Facilities*
8. *Institutional Support*
9. *Program Criteria*

B. ABET Curriculum Requirements

Of particular interest here is criterion 5, "Curriculum." The curriculum requirements specify subject areas appropriate to engineering but do not prescribe specific courses. There is one specific requirement stated by ABET "Students must be prepared for engineering practice through a curriculum culminating in a major design experience based on the knowledge and skills acquired in earlier course work and incorporating appropriate engineering standards and multiple realistic constraints."

As defined by ABET "Engineering design is the multi-disciplinary process of devising a system, component, or process to meet desired needs. It is a decision-making process (often iterative), in which the basic sciences, mathematics, and the engineering sciences are applied to convert resources optimally to meet these stated needs." This definition clearly delineates the differences between a *design project* and a *research project*. Here students are expected to engage in a culminating major design experience that requires cross-disciplinary efforts and a physical design realization. This broad-based comprehensive approach is not the objective of typical fundamental research efforts which are directed and specific in nature.

C. The "Senior Design Conundrum"

Many university engineering programs satisfy this criterion to varying degrees of success by requiring a "capstone" senior design class or project. This capstone design project is often at odds with university promotion and tenure process (P&T) requirements for faculty. Capstone design projects are incredibly time consuming, and have the potential to detract from faculty time that would otherwise be dedicated to specific research projects. Senior tenured faculty with large research programs often "buy out" of class instruction, and undergraduate course instruction responsibilities often fall to junior untenured faculty.

Since the university P&T process emphasizes publishable, funded research. Faculty -- especially untenured faculty -- who participate in senior design capstone courses risk promotion advancement and could potentially jeopardize tenure. Thus exists the "senior design conundrum" – ABET requires a well developed senior design curriculum for program certification, but general university P&T processes discount its relative importance. These conflicting instructional requirements lead many university departments to do a 'minimal" job on senior design by substituting a senior year research project for a full-scale capstone course. Programs that *substitute* the capstone senior-year design with a senior year research project or a junior-year design course risk *losing* or not achieving accreditation.

D. Senior Design Project Achievability and Sustainability

Selecting a design concept that allows a small-scale prototype-demonstrator to be constructed within the time and budget constraints of a university-based senior-design project was a major challenge. To be achievable, a design project must have sufficient funding to allow a final hardware realization of the design. Achieving a design of sufficient sophistication to allow formal publication of at least some aspect of the results is a very desirable outcome and will support the sustainability of the project.

A balance between "achievability" and "creativity" must be struck to meet the program constraints. It is important that the design space for a senior design course not be too broad and that the design process not be too malleable. In industry, much of this structure is provided by the client. In an academic design class, the instructor of the senior

design course must limit the design space, requirements, objectives, and systems engineering approach to a level appropriate for undergraduates to accomplish in an academic year.

E. Top-Level Design Course Objectives

Design must be the major component of the course. Student teams should explore and evaluate possible design alternatives. Each member of each team should play an active role in the design activities. In this design class the students learn how to integrate engineering skills to solve complex engineering problems, present engineering designs in oral presentations, and document the design in a written report that is the basis of their engineering portfolio. This design experience is the final course that prepares students to enter the mechanical engineering profession.

Upon completion of this design class students will be able to synthesize mathematics, science, engineering fundamentals, and laboratory and work-based experiences to formulate and solve engineering problems in both thermal and mechanical systems areas. Students will have proficiency in computer-based engineering, including modern numerical methods, software design and development, and the use of computational tools. Students will be prepared to communicate and work effectively on team-based engineering projects. Students will recognize the importance of, and have the skills for, continued independent learning.

F. Student Design Team Experience Level

Instructors wishing to "take on" a larger scale 1-year design project must also be aware of the skill limitations of the students entering into their senior year. The vast majority of these students have only been exposed to only fundamental undergraduate materials where recitation and "test-skills" are emphasized and the open-ended nature of the design task can be very intimidating.

With an excessively open-ended senior design course, students must be responsible for inventing client requirements, the design methodology, and then eventually constructing a design to meet their own requirements. This is an approach fraught with danger. Care must be taken, however, not to "hijack" the design away from the students. Too many constraints or mandates from the instructor prevent students from developing a sense of ownership for the final design project. A strong sense of responsibility and ownership is critical to both motivation and the overall project experience.

Many of the required technical skills must be taught "on the fly" with students learning materials or subjects required to accommodate the design formalization. Thus formal instructor-lead lecture materials must be balanced with student lead-"brainstorming" sessions.

G. National Space Grant College and Fellowship Program Higher Education

In 2006, NASA's Exploration Systems Mission Directorate (ESMD) launched two new educational projects administered by the Educational Office at Kennedy Space Center:

1. *The ESMD Space Grant Student Project; and*
2. *The ESMD Space Grant Faculty Project.*

The Space Grant Student Projects Senior Design projects are intended to stimulate undergraduate research on current NASA activities and to identify innovative and novel concepts in the areas of

1. *Propulsion,*
2. *Lunar and planetary surface systems,*
3. *Spacecraft, and*
4. *Ground operations.*

When developed via the senior design process, these concepts can be used to complement research thrusts that are important to the sponsoring NASA field centers. Additionally, such practical academic experience will better the prospects for graduating seniors to pursue graduate studies and to seek careers in the Space industry.

The Space Grant Faculty Project assigns summer faculty to NASA field Center to gather senior design project ideas and internship opportunities in support of the ESMD Space Grant Senior Design Program. This component is crucial in establishing a close relationship between the centers and the consortia, as well as allowing for better matches to make effective and substantial contributions to NASA's ESMD work.

NASA
National Space Grant College and Fellowship Program

Stephen A. Whitmore
Course Developer and Instructor
July 1, 2010.

II. Project Overview

Human and robotic missions beyond low earth orbit (LEO) are key components of NASA's currently emerging strategy for space exploration. These missions will inevitably include human-crewed lunar and planetary surface landings. Trips to near-earth asteroids are also in the incipient planning stages. A permanent presence on the surface of an extra-terrestrial body like Mars or the Moon will require many landings by both human-crewed and robotic spacecraft.

Planetary and lunar surface landings are inherently dangerous undertakings, and successful landings are indeed rare events. Since the end of the Apollo era with the completion of Apollo 17 in December 1972, only five successful soft-landings have been achieved on the lunar surface, with the last landing being Luna 24 in 1976. During that same period there have been only six successful Martian surface landings with nearly as many failures. Although surface geology was a secondary consideration in selecting the Apollo landing sites; a primary consideration was crew safety and mission success. Thus all of the Apollo landing sites occurred in a narrow equatorial strip, near the lunar basaltic plains or "Maria." These landing sites were mostly free of significant surface hazards. Martian surface landing sites have been selected for similar benign surface terrain characteristics.

With a long term human extra-terrestrial surface presence, scientific objectives will become increasingly more important, and the landing site terrain will become increasingly more diverse. Correspondingly, as these surface landing sites become more "interesting," they will also become more hazardous. Thus, the development of a research and testing platforms allowing "pin-point" autonomous landing systems to be evaluated, refined, and matured is essential. Only a free flying-platform can develop surface landing technologies to a sufficient technology readiness level (TRL) to be considered for ultra-expensive, extra-terrestrial surface missions. Additionally, as was demonstrated during the Apollo era, the development of a flying human-pilot training vehicle for extra-terrestrial surface landings will become a long-term exploration necessity.

H. Background

Powered landings on the lunar surface presented several difficult situational awareness challenges to the Apollo astronauts. It was believed that significant differences in visual cues – when compared to terrestrial landings -- would be very disorienting to the astronauts. Because of the lack of atmosphere, the surface lighting was very high in contrast, and astronauts had little or no ability to see into areas enveloped in surface shadows. To train astronauts to deal with this lighting effect, the NASA Langley Lunar Landing Training Facility (LLTF) that used severe lighting and night training were constructed.[2] The LLTF modeled the $1/6^{th}$-g environment using a complex series of mechanical pulleys and cables. While providing a good visual simulation of the landing environment, the LTF never successfully produced the required fidelity, and the piloting feel was described as "sluggish and artificial."[3]

Most significantly LLTF was never able to satisfactorily reproduce the unusual physical orientation of the lunar landing vehicle during the approach and landing phase of the mission. Because of the $1/6^{th}$-g lunar environment (compared to a 1-g terrestrial environment), the physical orientation of the lunar module required an extreme pitch angle for a given horizontal acceleration.

Figure 1 demonstrates this reduced-g effect on pitch attitude. Here the equivalent pitch angles required for an equivalent thrust to weight are illustrated. Here W_0 refers to the weight at 1.0 standard earth-g's, T is the thrust required to hold the vehicle level, and θ is the tilt or negative pitch angle of the vehicle. The figure shows the equivalent pitch angles for a helicopter, the lunar excursion module (LEM), and the Apollo-era Lunar Landing Research Vehicle (LLRV).[4] Because a vehicle in $1/6^{th}$ g requires only a fraction of the vertical thrust component required to hold altitude as a terrestrial-based vehicle, the required pitch angle for a given amount of horizontal acceleration is significantly greater. A pitch angle of 5^o on earth is equivalent to 28^o on the moon.

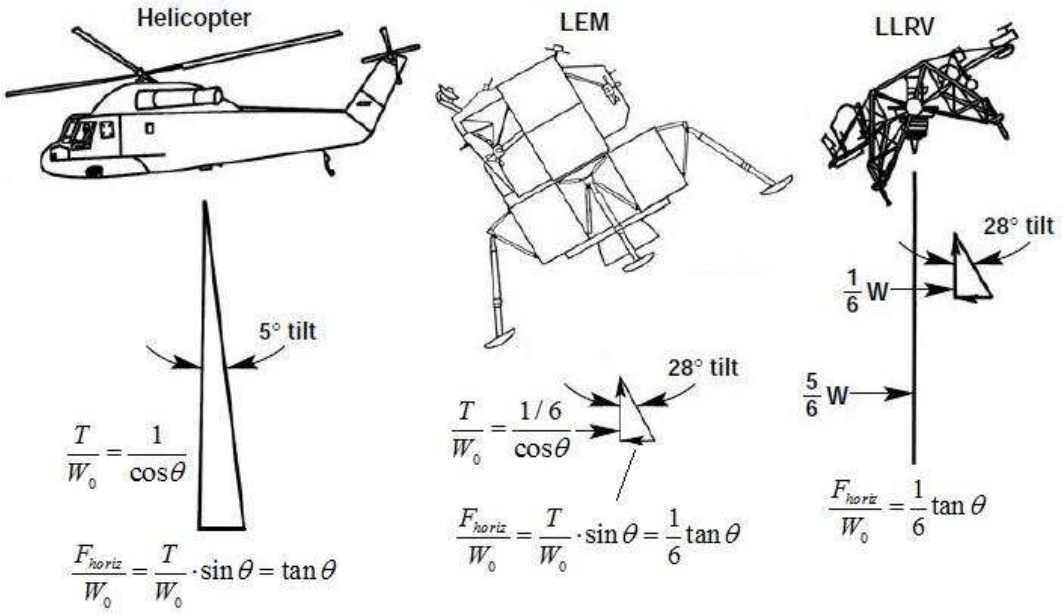

Figure 1. Pitch Angle Required by Terrestrial and Lunar Vehicles for Same Horizontal Acceleration.

A more risky, but higher fidelity free-flying vehicle designed to simulate the 1/6th-g lunar environment was developed at the NASA Flight Research Center (later to become DFRC). This vehicle, the Lunar Landing Research Vehicle (LLRV), used a single General Electric CF700-2V jet engine mounted on a gimbal. The engine was hydraulically driven to point in the vertical direction, and thrust was adjusted to offset the 5/6th of the vehicle weight. Hydrogen peroxide thrusters were used to maneuver an outer platform. Collectively, these apparatus presented an accurate simulation of the lunar landing event to the pilots. Figure 2 shows the original LLRV development platform on the tarmac at FRC. The jet engine, pilot cabin and maneuvering thrusters are clearly visible.

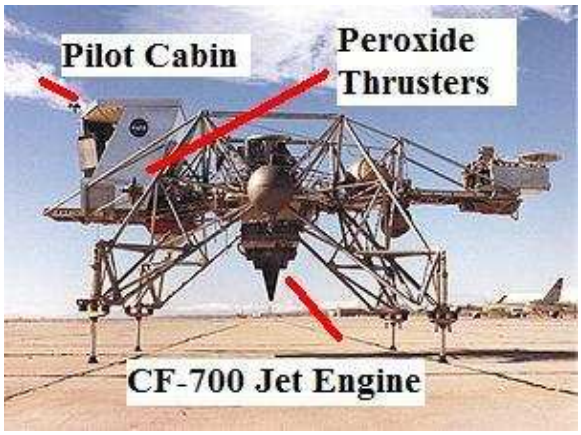

Figure 2. The Lunar Landing Research Vehicle.

Once LLRV became operational, the vehicle was adapted for crew training and 5 Lunar Landing Training Vehicles (LLTVs) were delivered to NASA Johnson Space Center (JSC). The LLTV was a difficult vehicle to fly, and the analog control systems available at the time were insufficient to control the vehicle under all flight conditions. Controllability was especially poor when flying in cross winds. Three of the five original LLT vehicles crashed before the end of the Apollo program. Emergency ejection and parachute systems prevented any significant injury to the pilots. There were also issues associated with hydrogen peroxide leaking from the thrusters' fuel tanks and burning the pilot's skin. Despite the sizeable risks involved in flying the LLTV, seven of the nine astronauts who trained for lunar landings using the LLTV testified that the vehicle was a key enabler for the lunar landing missions.[5]

I. Project Scope and Purpose

This project to be described in this handbook designed and built a free flying research vehicle that reproduces many of the capabilities demonstrated by the 1960s-era LLRV and LLTV. The project was the outcome of a two-semester senior design capstone course at Utah State University. The design course was developed and instructed by the Mechanical and Aerospace Engineering Department (MAE) at Utah State University during academic year 2009-2010. The complexity of the design – building an actual flying vehicle – required a large interdisciplinary team to be assembled. The size of the team – 7

graduate research assistants, 19 undergraduate student design team members and a faculty mentor – required that system requirements and team roles and responsibilities be clearly defined. Formal systems engineering techniques were applied to facilitate this process.

The approach for this project – whenever possible – was to replace 1960s-era analog designs with proven and reliable modern digital computer-aided technologies. This sub-scale (~$1/10^{th}$ scale) vehicle produced by this work simulates the reduced-gravity (i.e., lunar or planetary surface environment) using a vertically-thrusting jet engine to partially offset the vehicle weight. Although this vehicle is remotely piloted, the design is intended as a scalable configuration. The design only uses technologies that can potentially be scaled to a size capable of carrying a human crew.

This project includes elements of all four of the critical technology thrusts identified by ESMD as key for the future of space exploration. These areas include spacecraft systems, propulsion, lunar and planetary surface systems, and ground operations. The vehicle is formally designated as the Lunar or Planetary Surface Landing Research Vehicle (*LPSLRV*), and was nicknamed the "Flying Rhino." The vehicle nickname is derived from the brand name for the gravity offset jet engine, the JF-170 Rhino.

III. Course Overview

The Lunar and Planetary Surface Research Vehicle (LPSLRV) is a new senior-design project at Utah State University (USU). The two-semester sequence, complements both the ESMD Senior Design and ESMD Faculty projects, and was developed as a "packaged" senior design course that can be incorporated into university curricula across the USA and Puerto Rico.

The associated course materials to be described in this handbook detail the systems engineering processes that were developed, how these processes were applied to the student design, and presents examples of results, outcomes, and measures of instructional effectiveness. Detailed systems design details and experimental results, both laboratory-based and flight-test are presented both in formal lecture materials and student-compiled design reports and briefings. Test data are compared to design and analysis computer codes developed by the student are collected in a DVD appended to the final design student report.

J. Course Text

The required text for this design class is *Understanding Space: An Introduction to Astronautics (Third Edition), Jerry. J. Sellers, McGraw-Hill, 2005, ISBN 978-0077230302.* Supplemental materials were posted to the course web site as required. (See section III J.1).

K. Course Description

The design course was developed and instructed by the Mechanical and Aerospace Engineering Department (MAE) at Utah State University during academic year 2009-2010. This course was instructed as a two-semester sequence, with MAE 5930 Technical Elective taught fall semester 2009, MAE 4800 Senior Design spring semester 2010. Table 1 shows how the courses were listed in the Utah State Academic Catalog

The Fall Semester introduces students to design and systems engineering concepts, and provides preliminary design of a prototype configuration. Spring semester involves design closure, leading up to fabrication, integration, and subsystem testing. The academic year is completed a complete-system flight test.

Table 1. USU Course Listings for Design Project

Fall Semester, 2009 *Course Title:* ***Launch Systems Design*** *Course No.:* ***MAE 5930 (3 units)*****, CRN 43050** *Class Times:* 1:30-2:20 MWF *Location:* ENGR 401 *Prerequisites:* MAE Senior with Good Academic Standing, Concurrent Registration in Compresssible Fluids, MAE 5420
Spring Semester, 2010 *Course Title:* ***LPLSRV Design*** *Course No.:* ***MAE 4800 (3 units)*** *Class Times: TBD* *Location:* TBD *Prerequisites:* MAE 5420, MAE 5930

L. Course Structure

One of the most important aspects of a capstone design course is the presentation of introductory materials that provide sufficient project background and technical information. This upfront material allows the students to begin making meaningful design contributions very early in the academic year. This early portion of the class also provides assessment metrics that allow students to be assigned to project aspects best suited to their skills and interests. For the LPSLRV project, the academic year is kicked-off with a graded assignment that mandates reading previous year's final design reports (and other relevant published technical materials) and answering a series of questions regarding material contained in those overview materials.

This initial assignment provides students with a wealth of information about the general project and also provides a template for their own technical writing and organizational efforts. During the first month of the academic year, the students are presented formal lectures that cover a wide swath of materials including aerodynamics, flight simulation,

propulsion, and systems engineering. These lectures are very condensed with derivations deferred to textbooks or complementary academic notes. Homework is assigned to allow the students to comprehend the presented materials. These assignments facilitated the development of preliminary design and simulation tools that were used for the remainder of the project.

During fall semester a maximum of 2 1-hour lectures were delivered each week. Details of the instructional modules will be presented later in this section to this handbook. At least a one-hour period per week was made available for "break off team" meetings. *These team breakout days were designated as "Design Friday."* As necessary, design teams also broke off into small development teams outside of class. During the spring semester lecture periods were reduced to 1 hour per week with the remaining 2 hours dedicated to student lead technical interchange meetings and technical subgroup meetings.

M. Team Summary

The student team consisted of 19 undergraduate students taking the class for credit and 7 graduate research assistants. Graduate teaching assistants were responsible to assisting with instructional material development and project grading. Graduate research assistants were responsible for assisting the undergraduate students in various technical discipline areas. The experience and subject matter expertise provided by graduate teaching and research assistants were essential to accomplishing the project goals and objectives. Students were broken up into industry-style discipline teams, and elected two undergraduate team members to serve as Chief Engineer and Systems Engineer. Table 1 details the team roster and defines individual roles on the project.

Table 2. Team Roster

Course Instructor	Stephen A. Whitmore, PhD, Assistant Professor MAE Department
Graduate Teaching Assistants, MAE Department	Shannon Eilers, Matthew Wilson
Graduate Research Assistants, MAE Department	Ryan Schaefermeyer, Spencer Sessions, Cordell Wright, Zachary Peterson
Graduate Research Assistant, Computer Science Department	Bowen Masco
Chief Engineer (Undergraduate)	Sarah Isert
Systems Engineer (Undergraduate)	Vicki Ragsdale
Undergraduate Team Members (Alphabetical Order)	**Discipline Sub-team Membership**
Blonquist, Jason	Aerodynamics/Mechanics, Structures
Carter, Jason	Recovery/Safety, Structures
Christensen, Andrew	Controls, Instrumentation, Webmaster
Crockett, Derick	Controls, Flight Operations Lead, Propulsions
Dawes, Travis	Propulsions, Structures
Godfrey, Jess[3]	Aerodynamics/Mechanics Lead, Flight Operations, Instrumentation
Grange, Josh[3]	Controls, Power
Hoffer, Nathan[3]	Aerodynamics/Mechanics, Power Lead, Propulsions, Software
Irving, Jordan[3]	Recovery/Safety Lead, Software
Lang, Shawn[3]	Instrumentation , Recovery/Safety, Power
McCulley, Jon[3]	Flight Operations , Instrumentation Lead, Software
Meeks, Anthony[3]	Controls, Mass Allocation/Solid Edge, Purchasing, Structures Lead
Merrill, Rob[3]	Aerodynamics/Mechanics, Flight Operations, Software Lead
Pearce, Greg[3]	Instrumentation , Structures
Prows, Jeff[3]	Instrumentation, Software, Webmaster
Riding, Ken[3]	Document Control, Mass Allocation/Solid Edge, Structures
Warr, Mark[3]	Aerodynamics/Mechanics, Controls Lead

N. Course Deliverables

This project designed, built, and tested a small-scale prototype of a terrestrial based lunar landing simulator. The project is an outcome of a senior design course -- developed as a partial requirement of a NASA Office of Education grant. As such every aspect of the project has been logged, and more than three giga-bytes of information are archived and documented for future use. A significant final outcome is a packaged senior design course that can be incorporated by other universities across the nation. It is anticipated that the vehicle will remain in flight for some time after the completion of this design course, with the long term goal of developing a world class research platform for evaluating planetary landing technologies or mission concepts.

Students used or developed simulation codes required to fulfill team objectives as necessary. Students became sufficiently proficient in technical writing to deliver a professional grade final design report. Design and analysis computer codes developed by the student are collected in a DVD appended to the final design report.

1. Web Sites

All of the materials listed in the following sections are available for down load via internet browser from the class[6] and student-prepared (Ref. 7) web sites. These two associated web sites will remain active and supported for at least 24 months following the completion of the project.

2. Formal Presentations and Design Reviews

There were four major design reviews for this project. These reviews, listed in Table 3, were presented to departmental faculty as well as outside reviewers from NASA and the aerospace industry. Several members on the Utah American Institute of Aeronautics and Astronautics (AIAA) section attended the preliminary and critical design reviews. Peer evaluations were collected after each review. These reviews were webcast and recorded for future reference. Electronic copies of the presentations can be downloaded from the LPSLRV project documents web site.[7] These briefings are also uploaded to the NASA PBMA server for direct download.

Table 3. Summary of Formal Design Reviews

Review	Description	Date	Target Audience
LLRV/LLTV Design Features and Systems Review	Review of the Apollo-Era Lunar Landing Research and Astronaut Training Facilities	September 21, 2009	Program Internal technical Interchange Meeting, Formal presentations to the class.
Conceptual Design Review	Student Presentation to USU Dean of Engineering, Department Heads	October 13, 2009	USU Internal, College of Engineering, Student Design Team
Preliminary Design Review	Peer review by USU Faculty, NASA Sponsors, Technical Monitors, Industry Professionals	December 8, 2009	NASA Sponsors, Industry Reviewers
Critical Design Review	Same as above	March 25, 2010	Same as above

3. Trade Studies and Design Reports

Two formal trade studies were performed. These trade studies selected the gravity offset (jet engine) and maneuvering (quadrotor) drive components. Two student-develop formal design reports were also composed. These reports include a formal system-engineering document, and a two volume final design report. Portable Document format (PDF) copies of these trade studies and design reviews may be found on the LPSLRV student website. (Ref. 7) These reports are also uploaded to the NASA PBMA server for direct download. Table 4 lists these design reports titles and their release dates.

Table 4. Trade Studies and Design Reports

Report Title	Release Date
Remote Control Jet Engine Trade Study	October 21, 2009
Maneuvering Platform, Rotor Selection Trade Study	December 1, 2009
Systems Engineering Paper: Design of a Reduced Gravity Lunar Landing Research Vehicle	April 23, 2019
Reduced Gravity Landing Research Vehicle, Volume I: Concept Development to Vehicle Integration and Testing	May 6, 2010
Reduced Gravity Landing Research Vehicle, Volume II: Flight Test Report	May 24, 2010

4. Lecture Notes and Supporting Class Materials

Lecture Notes are available in Microsoft™ Power-point and portable document format (pdf). These notes are organized into 12 subject matter modules, with each module possessing sufficient detail to allow the design team to perform the necessary design tasks. As mentioned earlier, formal lectures were presented two hours per week during the fall semester. During the winter semester the formal lecture times were reduced to one hour per week. As required the materials can be presented in different order to meet the needs of the design class.

The course module titles and the associated supplemental materials are listed below. The modules and associated supplemental material are linked via the course web site. These notes are also uploaded to the NASA PBMA server for direct download. The document format is displayed in parenthesis after the title.

Section 1: Introduction

- Course Overview (ppt)
- Supplemental Materials to Section 1
  1. LLRV Monograph (pdf)
  2. NASA TN D-3838, Operational Features of the Langley Lunar Landing Research Facility (pdf)
  3. NASA TMX 57213, Initial Results of Studies of Handling Qualities of a Simulated Lunar Landing (pdf)
  4. Minutes of LLRV FRR Board, Jan. 12, 1970 (Armstrong/Conrad comments) (pdf)
  5. AIAA Paper: 68-254, Apollo Flightcrew Training /LLRV/LLTV(pdf)
  6. "Go For Landing" Conference, March 2008, Transcripts of LLRV Presentation (pdf)
  7. Dave Scott Comments on LLTV, JSC LLRV Technical Interchange Meeting, Dec. 08, (rtf)

Section 2: Space, Lunar, and Martian Environments

- The Space Environment (pptx)
- Supplemental Materials to Section 9
  1. JSC-1 Lunar Soil Simulant Data Sheet (pdf)
  2. JSC-1 Mars Soil Simulant Data Sheet (pdf)

Section 3: Systems Engineering

- Systems Engineering I: "What is Systems Engineering?" (ppt)
- Systems Engineering II: Systems Engineering Tools (ppt)
- Supplemental Materials to Section 3
  1. Response Protocol for an Assigned RID
  2. NASA Systems Engineering Handbook, SP-2007-6105 (pdf)
  3. Systems Engineering Fundamentals, DoD Systems Management College (pdf)
  4. Sample NASA Request for Action (RFA) form (docx)
  5. Sample NASA Review Item Disposition (RID) form (docx)
  6. USU Chimaera 2008-2009 Senior Design Report, AIAA Paper 2009-5193 (pdf)
  7. NASA SP-287, What Made Apollo a Success? (pdf)
  8. NASA TM X-58040, Apollo Lunar Descent and Ascent Trajectories (pdf)
  9. NASA TN D-6846, Apollo Experience Report - Mission Planning for Lunar Module Descent and Ascent (part 1, part 2) (pdf)

Section 4: Introduction to Rocket Science and Spacecraft Systems

- Spacecraft Subsystems Overview (pptx)
- Rocket Science 101: Basic Concepts and Definitions (pptx)
- Supplemental Materials to Section 4
    1. Altair Lander Overview (ppt)
    2. Altair Avionics Systems Architecture Study (ppt)
    3. LPSRV Top Level Concept (Sketchup 5)
    4. Helicopters for Lunar Descent/Landing Training (ppt)
    5. Template for Class Report Format (doc)

Section 5: Propulsion

- Propulsion Systems I: Rocket Systems Overview (pptx)
- Propulsion Systems II: Air Breathing Systems Overview (pptx)
- Propulsion Systems III: Propeller Theory (pptx)
- Algorithm Summary for Blade-Element/Momentum Propeller Theory (pdf)
- Propulsion Systems IV: Rotorcraft Performance and Flight Mechanics (pptx)
- Supplemental Materials to Section 5
    1. JetCentral Web page
    2. JF-170 Rhino User's Manual
    3. Small Turbine Jet Engines, "Do's and Don'ts" (pdf).. by John Redman
    4. US 1976 Standard Atmosphere Table, Metric Units: (xls)
    5. Fortran Code (txt)
    6. NACA RP 30, “Experimental Research on Air Propellers, II"
    7. NACA RP 447, “Static Thrust of Airplane Propellers”

Section 6: Avionics

- Spacecraft Avionics I: DC Motor Overview (pptx)
- Spacecraft Avionics II: Telemetry and Communications Systems (pptx)
- Supplemental Materials to Section 6
    1. USU UAV Flight Computer "WIKI" (html)
    2. RC-370 CH Motor Specs (pdf)
    3. Shimpo DT-209X Tachometer (html)
    4. NI 6024E PCMCIA DAQ Card Specs (html)
    5. ENTRAN PS-30 Power Supply Data Sheet

Section 7: Structures and Mechanics

- Recovery Systems: Parachutes and Airbags (pptx)
- Structures, Structural Dynamics, and Resonance (pptx)
- Mechanisms (pptx)
- Supplemental Materials to Section 7
    1. Parachutes for Planetary Entry Systems (pdf)
    2. Design and Testing of the HOPE-X HSFD-II Landing System (pdf)
    3. Design and Testing of the K-1 Reusable Launch Vehicle Landing System Airbags (pdf)
    4. Computer Simulation of an Airbag-restrained Passenger in Impact Simulator (pdf)
    5. Landing Strut Impact Force Simulation Model (zip)

Section 8: Testing and Measurements

- "Rhino" JF-170 Thrust Model, Derived from Test Data (pptx)
- Introduction to Labview (pptx)
- Classification of Measurement Errors, Calibration, Trend Lines, and Data Presentation (pptx)
- Probabilistic Assessment of Experimental Uncertainty (pptx)
- Supplemental Materials to Section 8
    1. Appendix 8, Strain Gauge Measurement Example (from MAE 3340) (pptx)
    2. "Vishay Box" Voltage Read VI (VI)
    3. "Vishay Box" Analog Output Calibration VI (VI)

Section 9: Flight Dynamics and Controls

- Flight Dynamics and Controls I: Motions in 6-Degrees of Freedom (pptx)
- Flight Dynamics and Controls II: Control Actuators, Control System Examples (pptx)

- Flight Dynamics and Controls III: Introduction to Feedback Control Systems (pptx)
- Flight Dynamics and Controls IV: Digital Feedback Control (pptx)
- Supplemental Materials to Section 9
    1. Appendix 8: Introduction to Geodesy (pptx)
    2. Comparison of Lunar Landing Trajecotry Strategies Using Numerical Simulations (pdf)
    3. NASA TN D-3903, Flight-Test Evaluation of an ON-OFF Rate Command Attitude Control System of a Manned Lunar-Landing Research Vehicle (pdf)
    4. LEAPFrog Paper: AIAA 2007-2764 (pdf)
    5. JSR Paper: Manual Attitude Control of the Lunar Module (pdf)
    6. STARMAC Quad Rotor Control Paper: AIAA 2007-6461 (pdf)
    7. Australian, Quadrotor Robot Paper (pdf)
    8. "VASALARaptor" QuadRotor Control, Final Report, U. Colorado AAE (pdf)

Section 10 Introduction to Orbital Mechanics

- Orbital Mechanics I: Kepler's Laws (pptx)
- Orbital Mechanics II: Vis-Viva Equation, Orbital Maneuvering, Hohmann Transfer, 3-Dimensional Orbits (pptx)
- Orbital Mechanics III: Planar, Orbital Equations of Motion (pptx)

Section 11: History, Politics, and the Future of Spaceflight

- Rockets, Past, Present, and Future (pptx)
- USA Space History, Policy, and Organizations (pptx)
- Supplemental Materials to Section 11
    1. The Road to Space: The First 100 Years
    2. Why Human Mars Exploration is So Surprisingly Hard?

Section 12: Technical Writing

- NASA Style Guide (pdf)
- Scientific Writing, An Introduction (ppt)
- Formatting Scientific Documents (ppt)
- Avoiding Common Errors of Grammar (ppt)
- The Craft of Editing (ppt)
- Structure: the Strategy of Style (ppt)
- Language: The Way We Use Words (ppt)
- Illustration: The Meshing of Words with Images (ppt)

O. Course Grading

As mentioned earlier, a strong sense of responsibility and ownership is critical to both motivation and the overall project experience. Getting students to “buy in” to the team goals is essential for overall success of the project. As such “attitude, teamwork,” and enthusiasm,” were essential components for getting an excellent grade in this class.

The class grades consisted of scores for overall class efforts and achievements, and scores for individual efforts and achievements. Weekly homework and reading assignments were given and up to 25% of student grades came from individual homework assignments, programming assignments, test and measurement assignments, and “pop” quizzes. Approximately 35% of student’s individual “weighted class grades” came from peer evaluations of total performance. The peer rating were essential to insure that a particular student did not “slack” and allow other students to carry the load for them. The remaining 40% of the overall score results from an average class grade combining the design reports and presentations.

IV. Systems Engineering

As mentioned earlier, the size of the design team, coupled with the multidisciplinary nature of the project, required the use of formal systems engineering and management concepts throughout the class. Students were broken up into industry-style discipline teams. Figure 3 shows this team breakdown. Students were required to be members of at least two technical discipline teams.

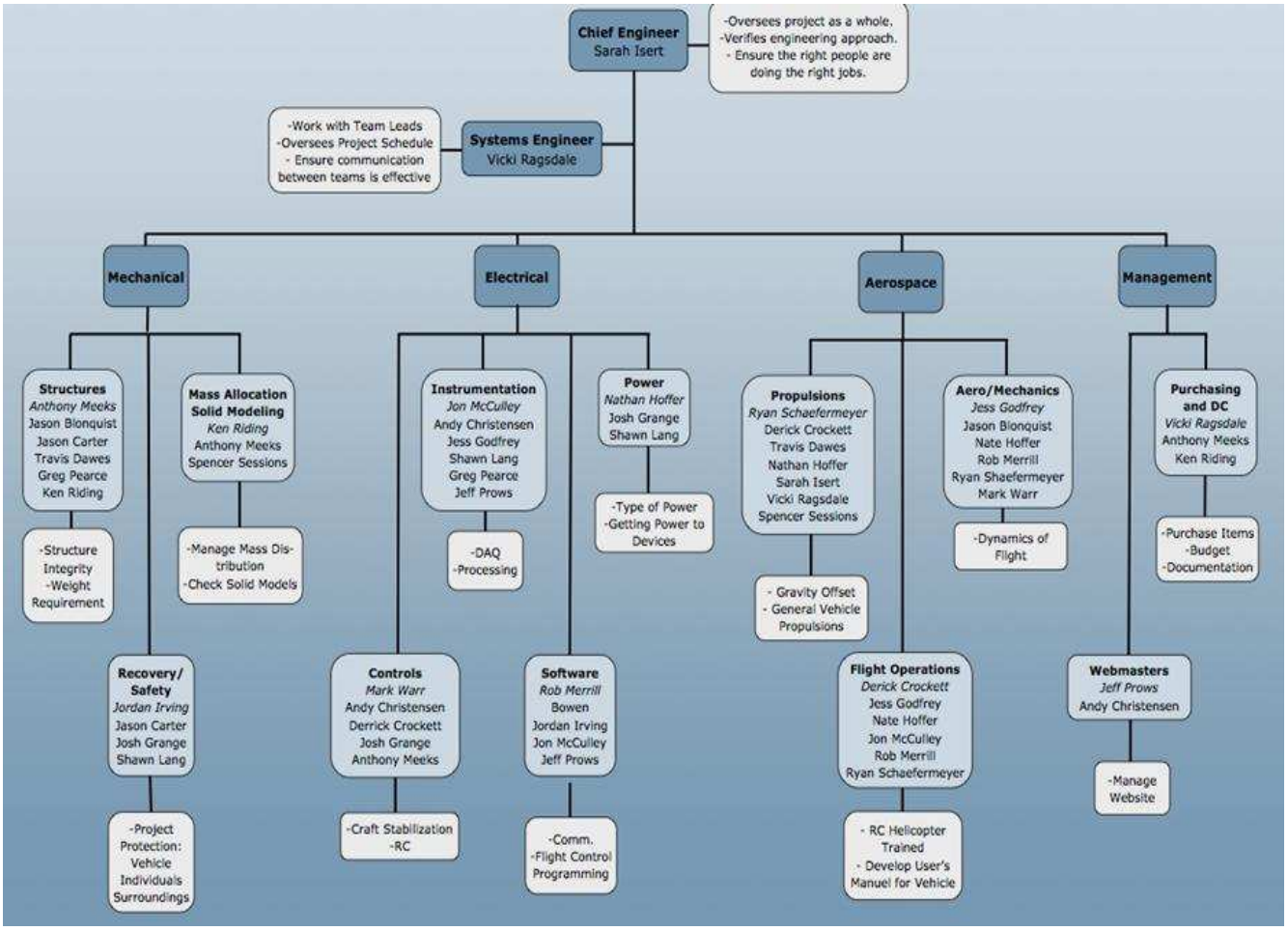

Figure 3. Team Disciplinary Breakout.

P. Systems Engineering Processes

As mentioned in the introductory section, the size of the team and the highly interdisciplinary nature of the design being attempted required that formal systems engineering techniques be applied to the design process. This section will highlight some of the design systems engineering processes that were used during the project.

5. Review Item Disposition

A Review Item Disposition (RID) procedure was developed to ensure fluid communication between sub-teams as well as provide a means of formal documentation for actions performed to complete the project. This process is modeled on the formal processes widely used within NASA, the Department of Defense (DoD), and the aerospace industry. During this process anyone on the team can initiate a Request for Action (RFA) or Request for Information (RFI) and assign it to a specific person or sub-team with a desired date of completion. An RFA assigns a specific task to be performed and documented, while an RFI asks for information about a system that is critical for the development of the project. At each team meeting, RIDs that are "due" are presented in a two slide PowerPoint presentation. This formal presentation allows the entire team to understand the decision being made, and documents progress or "neglect." The formal presentation makes it hard for students to "hide" in the process. If the action or

information was sufficient, the RID is formally closed by the Systems Engineer. RIDs can be extended if more time is necessary for satisfactory completion. Figure 4 depicts a flow chart of the RID process.

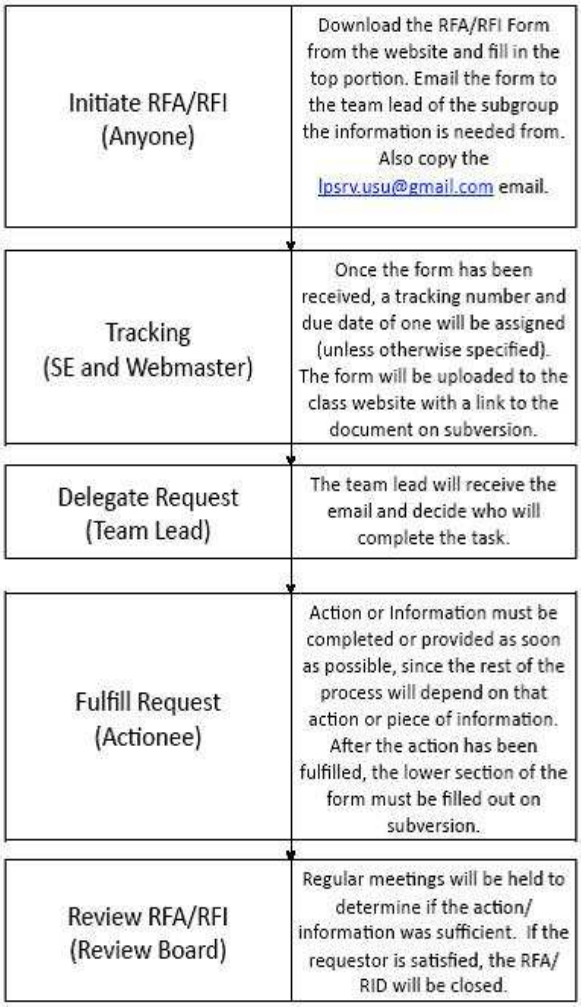

Figure 4. Review Item Dispensation (RID) Process.

6. Information Tracking

All RIDs are tracked on the student-built website. This website also presents formal documents such as trade studies, presentations, and test reports, that were created In addition to keeping formal documents on the website, an online "wiki" was developed for easy uploads of information. The "wiki" provided a quick reference for other team members. This wiki archives general knowledge gained this year for future teams.

7. Document Control

A document control system, using primarily Google Docs™, was created to track the variety of documents created during this project. As shown in Table 5 each sub-team was assigned a number, which acted as the first two numbers of the document number. The next three numbers were chosen chronologically. For example, the reference number 01-001 represents the Management team. The -001 indicates the first document from this group.

Table 5. Document Control Numbering Scheme

Sub-Team	Associated Number
Top Level Management	01
Aerodynamics	02
Propulsions	03
Structures	04
Safety	05

Q. Requirements Analysis

This section develops programmatic and system-level requirements. Both top-level and derived requirements are presented. This requirements analysis was used initially to come up with a top-level *concept of operations* and a workable *design reference mission.*

8. Programmatic Level Requirements

Top-Level design requirements, itemized in Table 6, were defined by the NASA technical point of contact based on the results of a NASA-internal trade study performed in 2008.[8] There are five NASA-defined requirements:

1) The design must be free flying.

2) The design must account for a reduced gravity environment.

3) The terminal stage of descent may be flown either autonomously or remotely piloted.

4) The vehicle shall be a platform for sensor evaluation.

5) The vehicle shall be designed and constructed within the constraints of a one-academic year senior design course

9. System Level Requirements

The decisions to go with a rotor-based maneuvering system for the outer platform and a jet-engine for the inner gravity-offset platform drove many of the subsequent sub-system design requirements. The sub-system particular requirements, their designation numbers, the source of the requirement, and the verification methods are listed in Table 7.

Table 6. Initial and Derived Program Level Requirements

Requirement	Number	Source	Proof of Achievement
Vehicle shall be free-flying	0.PRJ.1	NASA DFRC	Entire vehicle shall lift off the ground on its own power
Vehicle shall simulate lunar landing on Earth	0.PRJ.2	NASA DFRC	Video
Vehicle must be remotely controlled by trained pilot	0.PRJ.3	NASA DFRC	Flight test, pilot input
Vehicle shall be a platform for sensor evaluation	0.PRJ.4	NASA JSC	Data from onboard sensors
Vehicle design shall be conducted within constraints of one academic-senior design course	0.PRJ.5	NASA ESMD Office of Education (Customer)	Final functional test completed by May 8, 2010 and project within budget
Vehicle shall be reusable and capable of multiple flights	0.PRJ.6	Derived from 0.PRJ.2	Successful completion of second flight test
Mission shall be completed in 5 minutes or less	0.PRJ.7	Historical; 0.PRJ.2	Mission shall be timed
Vehicle design shall be compatible with environmental and safety constraints of operating within a university environment	0.PRJ.8	USU Risk Management Office	Risk Management sign off on flight testing

Table 7. System Level Requirements

Requirement	Number	Source	Proof of Achievement
GRAVITY OFFSET			
Gravity offset system will provide enough thrust at 80% RPM to offset necessary amount of vehicle weight	0.SYS.1	0.PRJ.2	Thrust at 80% throttle is greater than or equal to 5/6 of the vehicle weight. Determined by static test
Thrust vectoring system shall keep gravity offset system opposing local gravity vector at all times in flight	0.SYS.2	0.PRJ.2	Measure the deflection angle using onboard sensors
MANEUVERING			
Maneuvering system shall provide enough thrust to offset necessary vehicle weight at 80% RPM	0.SYS.3	0.PRJ.2	Thrust at 80% is greater than or equal to 1/6 vehicle weight. Determined by static test
Maneuvering system shall provide enough differential thrust to allow correct maneuvering angles to be achieved	0.SYS.4	0.PRJ.2	Measure available differential thrust on test stand. Analytically verify that given thrust will allow angles to be achieved
STRUCTURE			
The vehicle structure shall be designed so the vehicle can fall from a height of 0.3 m without damage	0.SYS.5	0.PRJ.6	Analytic calculations/ testing

R. Hazard Assessment and Risk Mitigation

Through comprehensive checklists and emergency procedures, the risk of human injury and vehicle failure is greatly reduced. For actual test flight, safety positions have been created so that, in the event of an emergency, there should be order in handling the situation. Months before jet engine and prototype testing began; safety rules and guidelines were put in place to ensure the well-being of everyone involved. Proper clothing was worn, including safety goggles, and earplugs, gloves and hardhats were necessary. A first aid kit and fire extinguisher were always on hand in the event of injury or fire.

The Risk Management Office (RMO) at Utah State University was involved in much of the decision making process for this project, and drove several of the initial decisions that affected the

overall system design. To satisfy RMO mandated hazard reporting requirements, a formal system of risk assessment was developed for this project. A hazard matrix was developed to determine and classify the hazard level of an anomaly. The hazard levels ranged from low to extreme based on likelihood of occurrence and the magnitude of damage that would ensue if a hazard was realized.

Figure 3 presents the hazard assessment matrix used for this project. To navigate this matrix, select a risk and determine how likely it is for the event to happen, and then assess how much it will affect the project. For example, the possibility of a person getting a paper cut during the duration of the project was fairly high but the *Magnitude of Failure* is negligible. Therefore, a paper cut is listed as a level-6 hazard. Level 6 is considered to be an acceptably low level of risk and can be "carried" without formal mitigation processes. On the other hand, consider the jet engine failing during flight. The *Likelihood of Failure* would be "unlikely;" however, the Magnitude of Failure would be "catastrophic." This hazard corresponds to a level 16, or extreme, hazard. Extreme hazards (level 13 and above) are unacceptable and require additional mitigation plan.

This assessment matrix was applied to every identified risk to determine if the level of risk is acceptable. If the risk was deemed unacceptable, then the design was modified or processes were developed to mitigate the hazard. Table 8 lists some example hazards identified by the project. The table lists the numerical hazard level, potential causes and consequences, and describes what mitigation process, if any, are required.

Magnitude of Failure

Likelihood of Failure	Negligible	Marginal	Critical	Catastrophic
Certain	11	15	19	20
Likely	6	10	14	18
Possible	5	9	13	17
Unlikely	2	4	8	16
Rare	1	3	7	12

Hazard level	Color
Low	
Moderate	
High	
Extreme	

Figure 5. Example Hazard Assessment Matrix.

Table 8. Example Hazard Tracking List

Hazard Level	Hazard	Causes	Preventative Measures
16	Engine Failure, causing an inability to keep vehicle in air	Debris Weather Temperature	Screen on jet intake, Check flying conditions, Pre-flight checklist Pre-flight and in-flight systems check
9	Human Injury	Burns from Jet Engine Exhaust Blowing debris Low-Voltage Electrical shock	Wear protective equipment, Designate "Keep out" zones, No power during maintenance, Follow manufacturer's recommendations, Follow checklists
8	Electronics Failure, causing a loss of power to rotors	Communication loss Communication interference Electrical shorting	Pre-flight and in-flight systems check
8	Vibration Effects, causing the vehicle to become unstable or components to become loose	Rotors rotating near Resonance	Pre/Post assembly testing
4	Fuel Leakage, forcing the time of the mission to be reduced	Bad seal on Fuel Tank, Improper filling of Fuel Tank	Quality check, Pre-flight checklist

S. Concept of Operations

A key enabler a successful design is to develop an early Concept of Operations (CONOPS) so that each of the subsystem design teams can scope the level of efforts required by their designs. For this design the initial CONOPS proposed a vehicle composed of two platforms. The design features a two-axis gimbal system that allows the inner gravity-offset gravity offset system on the inner platform to move independently in two degrees of freedom from the outer maneuvering platform. Stability and independence of each platform is provided by two independently control systems. The final propulsion systems selected for the inner and outer platforms are the result of trade-study assessments.

In order to meet project requirement 0.PRJ.8 (environmental safety), the decision was made very early in the program to eliminate the hydrogen peroxide maneuvering thrusters employed in the LLRV/LLTV design. Using a corrosive and toxic mono-propellant would require extraordinary safety and handling procedures that are incompatible with an "open" university design project. Similarly, developing a state-of-the art "green-propellant" bi-propellant thruster system is far beyond the scope of what can be accomplished in a one-year senior design project. Cold-gas thrusters were quickly eliminated because there was insufficient total impulse capability to meet project requirement 0.PRJ.7 (5 minutes flight duration). Thus, the lift thrusters were replaced by a propeller-powered quadrotor system. Selecting quadrotor system was a key programmatic design decision that drove many of the down-stream design decisions. Figure 6 compares the LPSLRV design CONOPS to the LLRV.

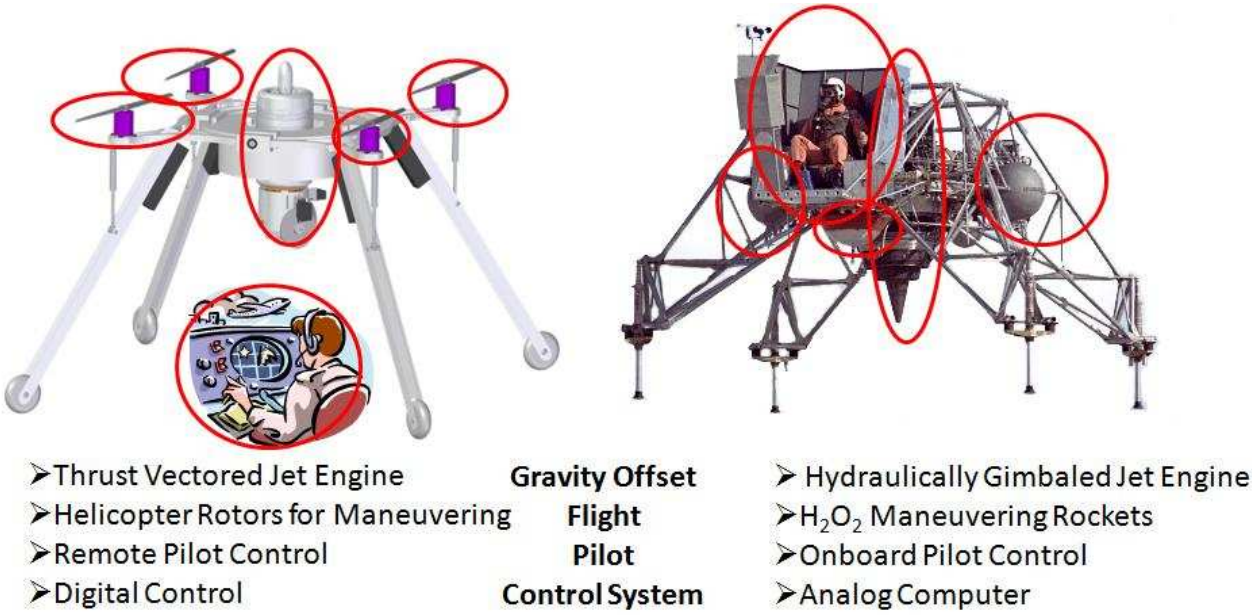

Figure 6. Comparison of LPSLRV and LLRV Concepts of Operations.

T. Design Reference Mission

One of the key enemies of a successful program is "mission creep." Mission creep more often than not leads to a program stalling or collapsing under its own ponderous weight. Because of limited resources and experience, student design projects are especially susceptible to mission creep. A "tried and true" way to keep a program on track is adherence to a Design Reference Mission (DRM). A well-defined DRM accomplishes top-level program requirements but limits scope of design and restricts unnecessary requirement growth. The design reference mission for this vehicle attempts to reproduce as many elements of a lunar landing mission as is feasible within the schedule and budget constraints of a single year undergraduate student design project.

Figure 5 shows the three phases of the Apollo landing profile.[9] Pictured are the in-orbit Keplerian maneuvers (5a), the powered descent phase (5b), and the final approach and descent phase of the landing (5c). Two key waypoints are shown on the approach trajectory; *high gate* – where the vehicle transitions from the powered descent to approach, and *low gate*[*] – where the vehicle transitions from approach to the vertical descent.

For this design project the DRM attempts to simulate the approach and landing phases of the mission (as did the LLTV and LLTV). To achieve a simulated lunar landing approach, the vehicle climbs, maneuvers horizontally to get onto the proper approach trajectory, then begins the powered descent before hovering for a vertical landing. An initial systems check is performed when the vehicle is at a 1 meter hover. Figure 6 depicts this design reference mission. Velocity and altitude markers were scaled from actual mission profile to keep the vehicle within the available testing range.

[*] The terms *high gate* and *low gate* were inherited from the Apollo program and are derived from naval aviation terminology for aircraft carrier landings.

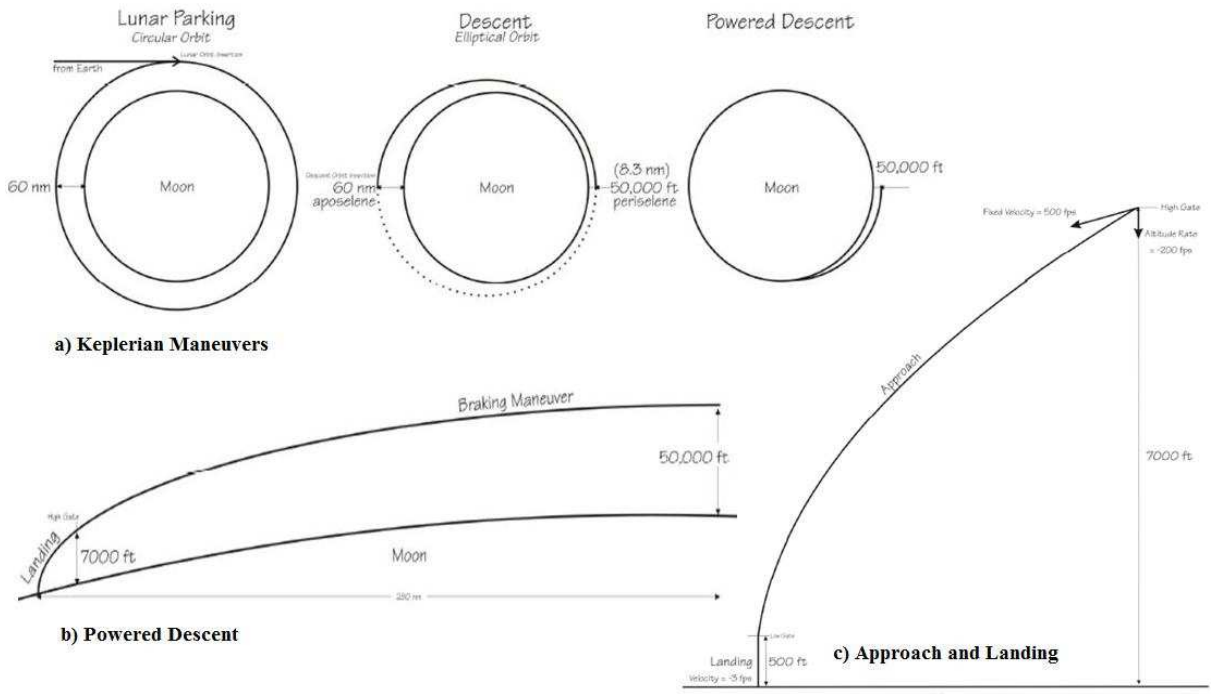

Figure 7. Phases of the Apollo Lunar Landing Profile.

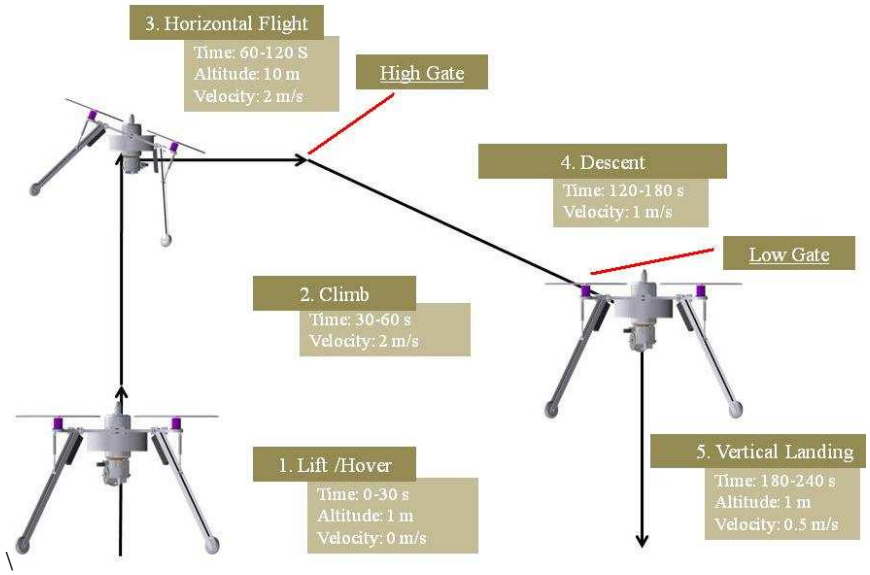

Figure 8. Design Reference Mission.

U. Vehicle Development

Figure 7 shows the decision sequence that was used to close on the overall vehicle design. This approach is similar to the classical design process for spacecraft and starts with the power-plant selection.[10] Since the gravity offset system was a key factor in fulfilling the primary mission requirement, selection of the gravity offset system was the starting point for vehicle design. Once the available thrust is known, a maximum allowable vehicle mass can be calculated as $6/5^{th}$ of the lifting capacity of the jet engine. This total vehicle mass then determines the required thrust needed from the rotors. The lifting capacity of the rotors drives the power requirements for the battery systems, etc. Using subsystem simulations based on

component performance testing, the process is iterated until an acceptable design closure is reached.

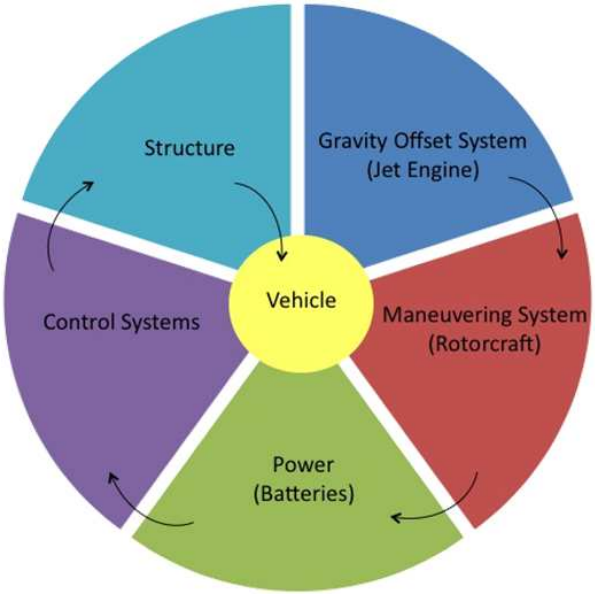

Figure 9. Vehicle Design Process.

10. Initial Vehicle Trade Assessments

The primary initial trade assessments selected the appropriate power plant technologies for the inner and outer platforms. This subsection describes the top-level trade studies that were used to select the most appropriate lift-technologies. Detailed procedures used to select the final power-plant systems design will be presented later in the "Vehicle Development" section.

One of the major components of the LPSLRV is the gravity offset system that enables the vehicle to respond in the Earth's gravity field as it would on the Moon. Several options were considered for this system, including rocket motors, electric ducted fans, rotors, and a small jet engine. A formal trade study was conducted to select the best choice for the gravity offset system power-plant. This trade study was a formal deliverable for the design class. Figure 10 depicts the lift options that were considered.

Rocket motors were determined to be unsuitable for the same environmental and safety reasons presented earlier. Additionally, ability to precisely control and modulate a rocket system for gravity offset is very limited. Finally, the amount of propellant required on-board would cause a prohibitive vehicle weight.

Figure 10. (L to R) Rocket Engines, Ducted Fans, RC Jet Engine, Helicopter

The electric ducted fans of the type used on remote control vehicles also proved to have prohibitive weight restrictions. Ducted fans are very power intensive, and for this design would have required the entire structure to be built out of batteries to provide enough power for the 5-minute mission. Gas-powered fans in the size compatible with this vehicle size are not readily available.

Jet engines, the final choice for this system and the type of gravity offset system used on the LLRV, are readily available with a wide variety of vendors and size options. Fuel and power requirements were reasonable, and preliminary analysis showed that interactions with the rotors would be acceptable. In fact the propeller-wash from the maneuvering platform likely has the effect of improving the jet performance. Therefore, a jet engine was chosen for the gravity offset system. Once jet engine technology was selected, a secondary trade study was performed to select the jet engine size, features, and lift capacity.

11. Jet Engine Selection Summary

With the type of engine used to provide the gravity offset determined, the team began an analysis to select a suitable micro-turbine. Figure 11 depicts this process. The trade study began with a consideration of the scope of the study. Limits were placed on parameters such as weight, thrust and fuel consumption based on preliminary projections of total vehicle weight, flight time, and budget. Then general research began, considering all possible candidates, followed by the preliminary analysis of groups of engines. Top engines were selected, researched, analyzed, and compared to each other. Of these four were chosen. These engines were researched and put in a quad chart and a matrix rating system. From these charts the vehicle engine was chosen.

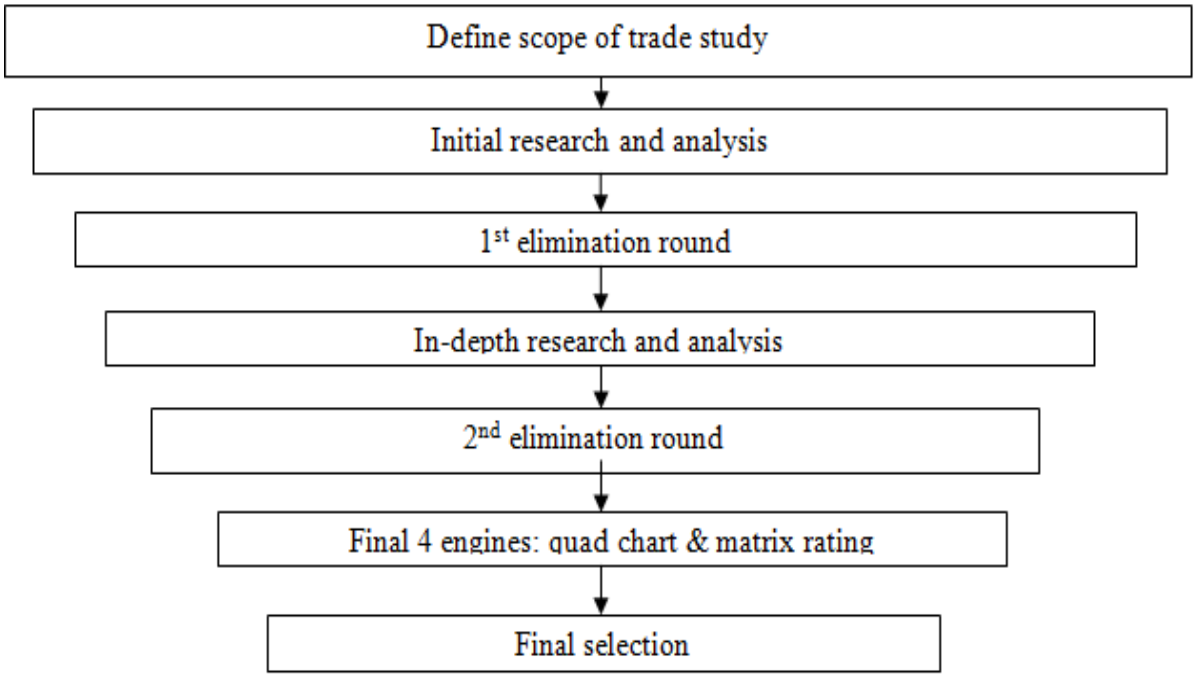

Figure 11. Jet Engine Selection Summary

12. System Interfaces

Figure 12 shows a functional block diagram of the overall vehicle design. The primary components are listed with arrows showing the flow of information and overall functional interdependence.

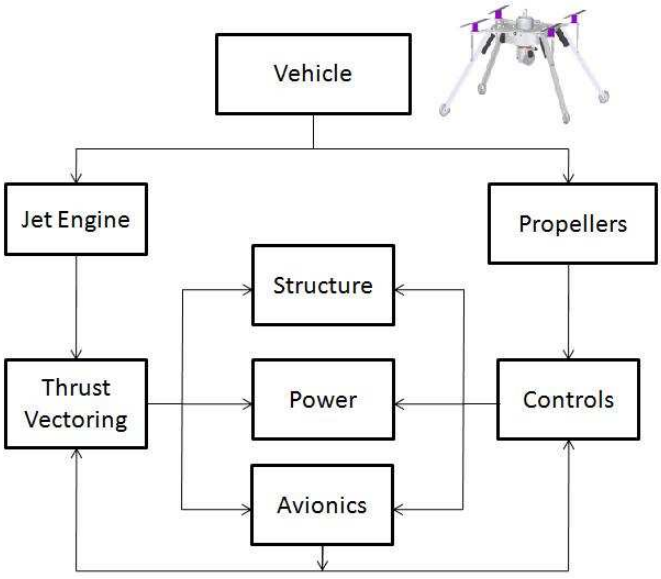

Figure 12. Vehicle Functional Diagram.

Table 9 shows a detailed interface chart used to track the impact of changes on one sub-system to other sub-systems. Each sub-system is listed in a "yellow box." If there is an interface between two subsystems, an M (for mechanical) or E (electrical) is written in the corresponding box. A mechanical interface is defined as a hardware connection between the two, whereas an electrical interface is defined as a software or electrical connection between the two. For example, the outer platform has mechanical interfaces with the inner platform: these are, the quad rotor system, the required instrumentation and avionics, and the batteries providing power. Similarly, the power system has an electrical interface with the outer platform, the jet engine, the flight computer and avionics. Details of these sub systems will be presented later in the "Final Design Description" section.

Table 9. Interfaces with Vehicle Sub-Systems

Outer Platform	M			M, E	M, E	M, E		E
	Inner Platform	M	M, E		E	M		
		Jet Engine	E		E	E	E	E
			Gumstix		E	E		
				Quad Powered board				
					Avionics	E	E	
						Power		
							Software, Ground Computer	M
								Pilot

V. Final Vehicle Design

This section presents only the final design for the LPSLRV. The design evolution and details regarding the verification testing used to characterize the component performances.[11] Details of the experimental apparatus used for engine characterization including the thrust, fuel mass flow curves, thrust vectoring vane moments, and other critical engine performance parameters may be found in Appendix F of that report. A brief summary of ground testing and systems verification is also included in the *Appendix A* of this report.

Figure 13 presents the solid 3-D model showing the final design configuration for the LPSLRV. The structural components were designed with the aid of structural optimization programs provided free of charge by Altair Engineering.[12] The landing gear are hinged at the root and angled at 45° to avoid the maximum downwash velocity area produced by the rotors. Small spring-loaded shock-absorbers are used to reduce landing loads.

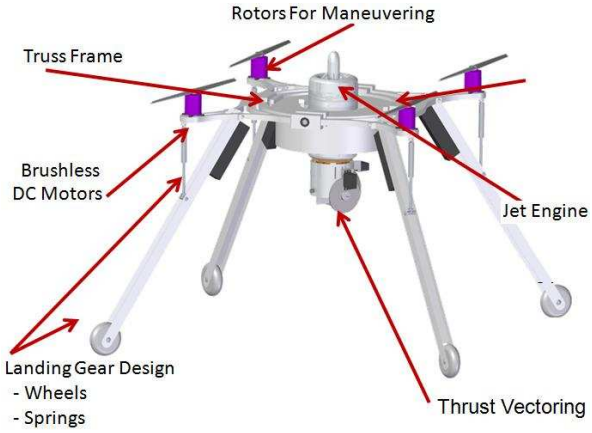

Figure 13. Final Design Configuration.

The vehicle features two gimbals designed to move independently about the pitch and roll axis. Figure 14 depicts the platform gimbal design. The gravity offset system is attached to the inner of the two gimbals and the maneuvering system is attached to the outer gimbal. The function of the gimbal is to decouple inner platform rotational dynamics from the outer platform. The outer platform holds all of the maneuvering rotors and associated drive-train components; while the inner-gimbal ring holds the jet engine and associated equipment. The fuel tank for the jet engine is integrated into the structure of the inner gimbal ring. The inner platform pitch and roll angles are controlled by a thrust vectoring system featuring exhaust turning vanes.

Figure 14. Inner and Outer Platform Gimbals.

V. Inner Platform: Gravity Offset System

The function of the gravity-offset system is to lift *5/6th* of the vehicle weight without contributing to horizontal linear acceleration. The gravity offset system features a Jet-Central® JF-170 Rhino[13] centrifugal turbine engine. The engine features a single shaft turbojet with an annular combustor. A single stage axial flow turbine drives a single stage centrifugal compressor. The shaft is supported by 2 fuel/oil lubricated, annular contact bearings. The turbine speed is controlled by the amount of fuel received from the fuel pump, which is controlled by a full-authority digital engine control system (FADEC). The turbine runs on both jet-A fuel and K-1 grade kerosene.

The FADEC is a total system for the control of the turbine. The main FADEC function is to control and regulate the fuel pump, providing the necessary fuel flow for controlled operation. Engine control is provided by two primary feedback sensors, a rotor RPM sensor, and an exhaust gas temperature (EGT) thermocouple. Additional diagnostic measurements include engine run time, and pump supply battery voltage.

All onboard sensor data can be monitored via a standard RS-232 C serial output. The throttle input to the FADEC is controlled by a pulse-width modulation (PWM) signal that complies with the industry standard servo control specifications. The serial connection is through an RJ-45 connector on the FADEC. The stock engine comes with a hand-held unit that can be used to manually program the engine. The LPLSRV team “reverse engineered” this design to allow the engine to be directly computed controlled in real time using a wireless link. The telemetry like will be described in more detail later in this section.

With the thrust vectoring system installed, the engine produces approximately 30 lbf of thrust at full throttle (120,000 RPM). Figure 15 compares the original manufacturer’s thrust/PRM curve profile

against the measured thrust RPM curve with the vectoring system installed. Details regarding the thrust measurements are presented in Appendix A or this report.

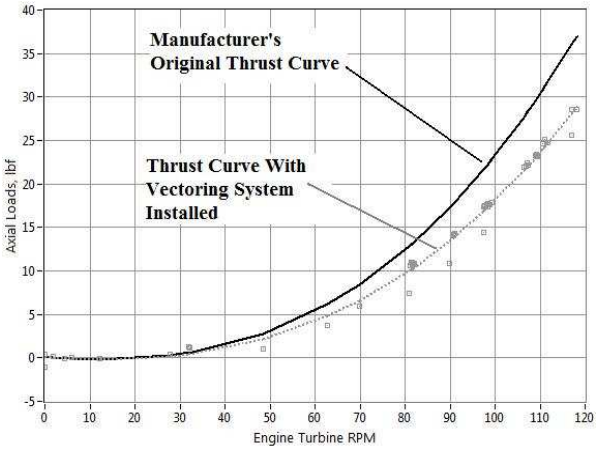

Figure 15. JF-170 Thrust/RPM Curve.

The thrust vectoring installation reduces the available thrust by approximately 17-18%. The RPM (x-axis) is plotted in units of 1000's of RPM. The thrust vectoring system is described in detail in the following section. The fuel consumption rate of the JF-170 Rhino is very much dependent on the operating RPM of the engine. Figure 16 shows the measured fuel mass flow consumption as a function of the engine throttle setting.

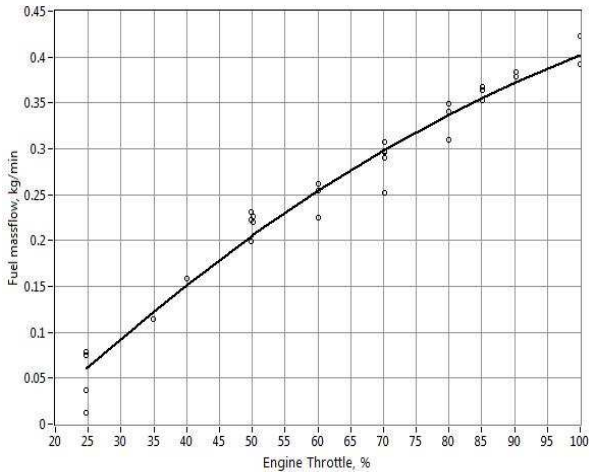

Figure 16. Fuel Mass Flow Consumptions as Function of Throttle Setting.

The vehicle design assumes a nominal flight thrusting level of 85% throttle for the gravity offset system.[†] Operating at an 85% throttle setting (115,000 RPM) produces approximately 26 lbf thrust and requires a fuel mass flow of 0.36 kg/min. Thus at a sustained 85% throttle, one kg of fuel can produce approximately 3- minutes of flight time.

13. Overview of the Thrust Vectoring System

Various well-developed thrust vector control (TVC) methods are available for use on a jet engine, some of which include: rotating the entire engine relative to the vehicle, a rotating nozzle that directs the exhaust in a different direction, insertion of moveable vanes into the exhaust flow.

Mechanically driving the inner ring against the outer ring to position the jet engine will result in two forces: the force exerted on the inner ring by the hydraulic system and a reactionary force exerted on the outer ring. The reactionary force would either have to be overcome by a large moment of inertia (compared to the inner ring's moment of inertia) or by the crafts maneuvering system. The very existence of the reactionary force means that the inner ring and the outer ring are not fully uncoupled in pitch and roll.

The thrust vectoring system for the LPSLRV employs exhaust plume turning vanes to direct the thrust away from the axial centerline of the vehicle. Moveable exhaust vanes, despite their propensity to reduce the total thrust level, were preferred for the LPSLRV inner platform. This method has the distinct advantage of being one of the lightest available vectoring methods, and features large force generation effectiveness. When compared to hydraulic gimbal systems installed on the original LLRV and LLTV configurations, exhaust thrust vectoring is mechanically simpler and requires only a fraction of the weight. Because the exhaust temperatures from the jet engine, approximately *650 C* at full throttle, are substantially lower than rocket plume exhaust temperatures, this design requires no active cooling or special high-temperature materials.

14. Turning Vane Design

Several vane configurations including cylindrical and elliptical leading edges, blunt and tapered trailing edges, and NACA-4 digit airfoil[14] sections were examined before finally deciding on the final vane contour. An interactive 2-dimensional, compressible-flow, computational fluids dynamics program, XFOIL 6.9[15], was used to calculate lift, drag forces, and pitching moment about the 1/4th chord on the airfoil. The code was run in inviscid-flow mode, with the airfoil viscous drag calculated using simple compressibility-adjusted, high-temperature, flat-plate skin-friction models.[16] Quarter-chord pitching

[†] The 85% throttle setting corresponds to operating at "Mil-power" in a military-style high performance fighter aircraft.

moments were translated to account for the vane offset from the hinge point of the inner gimbal ring.

Effects of total lift, flow separation at high angles-of-attack, and induced drag were considered. The simple blunted leading edge configurations offered the greatest ease of manufacturing, but tended to separate on the leeward side at moderate angles of attack. This flow separation results in a significant increase in the overall profile drag of the section. In the end, the NACA 0012 airfoil section offered the best overall performance. Figure 17 presents an XFOIL-derived surface pressure distribution for a NACA 0012 airfoil at 1.5^{o} angle-of-attack. .

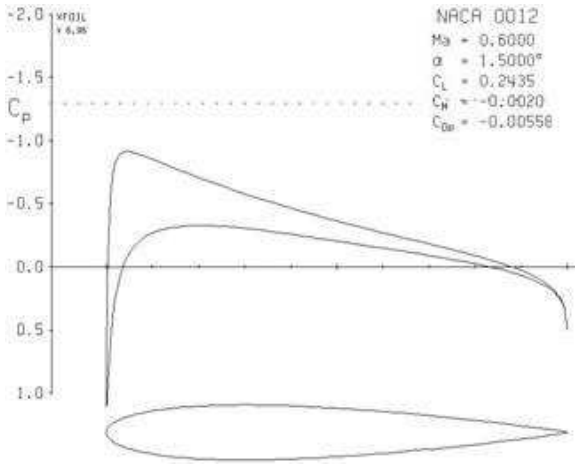

Figure 17. NACA 0012 Pressure Distribution at Mach = 0.6, and 1.5° Angle-of-Attack

The JF-170 Rhino has an unusual exit plane velocity distribution profile. This profile has a large momentum "hole" near the axial centerline – a likely result of the centrifugal turbine mounting and exit cone fairing. Figure 18 plots the exit plane Mach number distribution as a function of the radial distance from the axial centerline for 25%, 50%, 75%, 80% and 100% throttle settings. (Ref. 11) Clearly, the span of the high-velocity flow is approximately 30 mm wide on either side of the "momentum hole," which is approximately 12 mm wide.

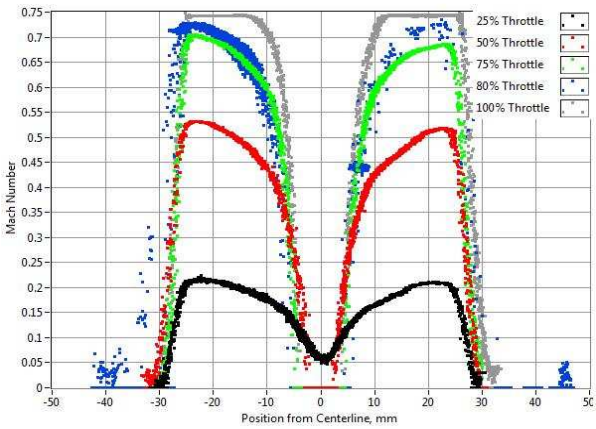

Figure 18. JF-170 Rhino Exit Plane Mach-Number Distribution for Various Throttle Settings.

To best take advantage of this flow distribution and to aid in manufacturability, the pitch and roll axis turning vanes were each divided into two sections each, with each section spanning approximately 33 mm with a 12 cm gap between sections. Due to the momentum hole in the center of the nozzle, the "gap" between airfoil sections eliminates pitch and roll vane interference while having a minimal effect on the overall performance. The vanes are slightly oversized to extend beyond the edge of the exit jet-plume. This extension helps to weaken the tip-vortex of wing and minimizes induced drag effects.

Figure 19 shows show the calculated gimbal-point pitching moment for a 66 *cm*[‡] *x 43 cm* airfoil section. The moment is plotted as a function of angle of attack for Mach numbers varying from 0.40 to 0.65. A positive angle of attack on the vane results in a negative pitching moment about the gimbal point.

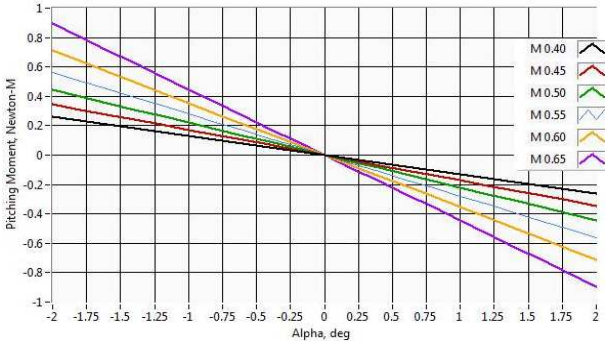

Figure 19. Gimbal Point Pitching Moment for 20 cm x 10 cm NACA 0012 Airfoil Section.

The data of Figure 19 were reorganized with the commanded moments and engine throttle settings

[‡] This dimension results from two vane segments each with a 33 mm span.

expressed as independent variables, and the corresponding servo vane-deflections (equivalent to the local vane geometric angle of attack) expressed as the dependent variable. These data, presented in Figure 20, will be used in the next section to complete the control system algorithm.

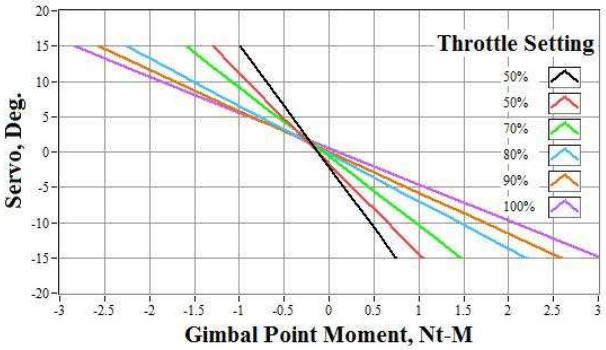

Figure 20. Servo Deflection Angle for Commanded Gimbal-Point Moment and Engine Throttle Setting.

15. Thrust Vectoring Mechanical Interface

The mechanism chosen for this design couples a set of NACA 00012 airfoils along the pitch and roll axes, and drives them using a geared servo mechanism. Figure 21 shows the NACA 0012 turning vane design. The center gap, vane span, and chord are marked on the image. Each vane segment was Machined from a single block of stainless steel, and the mounting rod was press fit and welded at the 1/4th chord of the vane.

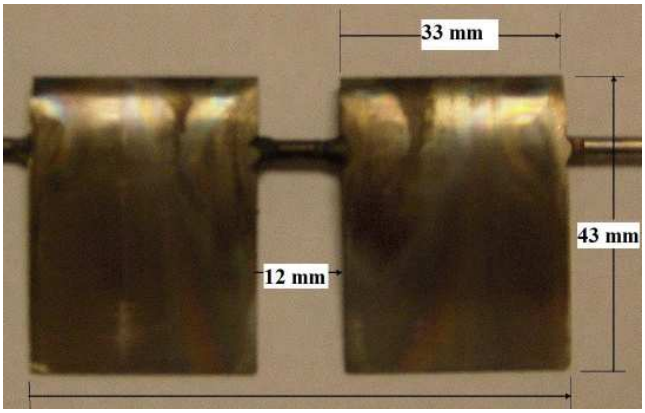

Figure 21. NACA 0012 Turning Vane Layout.

Hobby-class radio control (RC) servos were chosen to drive the system because of their proven track record, cost, and availability in a wide range of applicable sizes. For the LPSLRV design, two *HITEC HS-5245MG* digital programmable servos, featuring a pulse width modulated (PWM) drive signal, were selected to operate the vane mechanisms. The pulse width period is typically 20 milliseconds, with the duty cycle-determining the servo deflection. The range of the PWM signal can be adjusted from 100% to less than 10% to increase the available drive fidelity. Tests showed that with the servos re-ranged to have full throw deflection of $\pm 10^{o}$, the servos resolve angles down to at least 1/4°. This resolution is more than sufficient for the needs of the project.

Figure 22 shows a detail of the thrust vectoring components l. As long as the vane deflection remains less than 10^{o}, the gap in the center of each turning vane prevents interference between the pitch and roll axes. For the LPSLRV design the servos were programmed to have extents of travel between ±9°. This deflection margin was chosen to allow for servo-hysteresis and material distortion due to aerodynamic loads and plume heating.

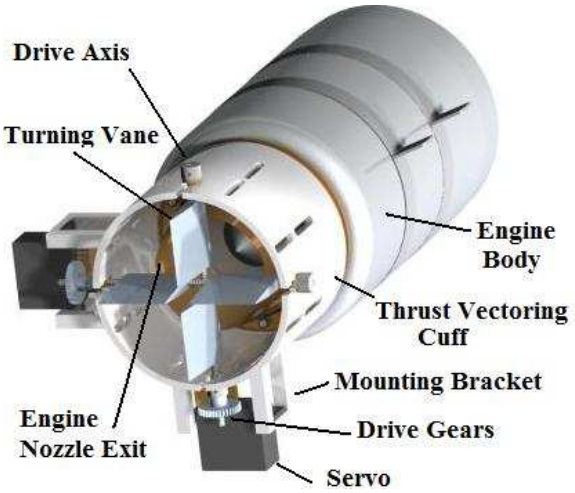

Figure 22. Solid Model of Thrust Vectoring Components.

16. Thrust Vectoring Control System

The pitch and roll axes of the thrust vectoring system are controlled independently using a proportional, integral, derivative (PID) control law. In this system the pitch angle *(θ)*, roll angle *(ϕ)*, pitch rate *(q)* and roll rate *(p)* sensed a miniature Inertial Measurement Unit (IMU)[17] are used as feedback parameters for the controllers. Details of the control algorithm will be presented later in this section.

The IMU, pictured in Figure 23, manufactured by MicroStrain Inc^{TM}, features a high-performance miniature attitude heading reference system that includes embedded tri-axial accelerometers, rate-gyros, magnetometers, and a temperature sensor. The sensor data are blended in an internal micro-processor running a sensor fusion algorithm to provide inertial navigation quality output parameters. User-selectable output parameters include Euler angles, rotation matrix components, Δvelocity vector

components, acceleration vector components, 3-axis angular rates, and 3-axis magnetic field components.

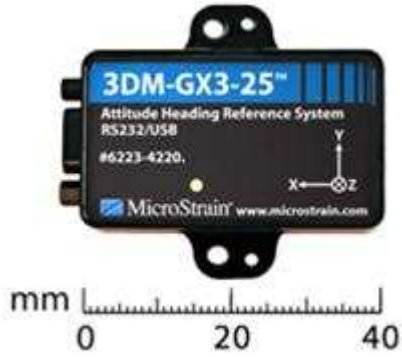

Figure 23. Miniature IMU Used for Thrust Vectoring Control System.

The PID control law generates a moment command to keep the gimbal pitch and roll angles very near pre-determined reference control angles – zero in the ideal case. A typical restorative thrust vectoring vane deflection is depicted in Figure 24.

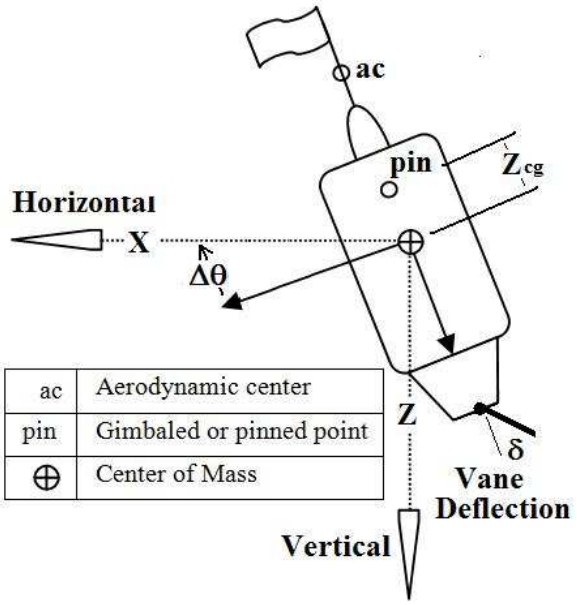

Figure 24. Vane Deflection for Pitch Angle Trim.

17. Proportional, Integral, Derivative Control Law

Equation (1) shows the PID control law for the pitch axis. The control law for the roll axis has an identical implementation.

$$K_p \cdot \tilde{\theta} + K_d \cdot \frac{d}{dt}\tilde{\theta} + K_I \cdot \int_t \tilde{\theta} \cdot dt = \frac{M_y}{I_{yy}} \qquad (1)$$

In Eq. (1), $\tilde{\theta} = \theta_{ref} - \theta$ is the error signal, i.e. the difference between the reference pitch angle -- typically zero -- and the IMU-sensed pitch angle. The parameter M_y is the commanded pitching moment to be generated by the pitch axis-turning vane. The parameter I_{yy} is the moment of inertia about the gimbal pitch axis. The gains $\{K_p, K_d, K_I\}$, are initially selected using a variety of synthesis techniques, and then "tuned" in an ad-hoc manner to give acceptable controller performance.

Various methods can be used to discretize Eq. 1 for implementation on digital computer, with the most common method being the bi-linear transform.[18] When the bi-linear transform is used to discretize the controller the resulting difference equation is

$$\begin{aligned} &\left(M_y\right)_{k+1} = \\ &\left(M_y\right)_{k-1} + K_p \cdot I_{yy} \cdot \left[\left(\tilde{\theta}\right)_{k+1} - \left(\tilde{\theta}\right)_{k-1}\right] + \\ &\frac{2}{\Delta t} \cdot K_d \cdot I_{yy} \cdot \left[\left(\tilde{\theta}\right)_{k+1} - 2 \cdot \left(\tilde{\theta}\right)_k + \left(\tilde{\theta}\right)_{k-1}\right] + \\ &\frac{\Delta t}{2} \cdot K_I \cdot I_{yy} \cdot \left[\left(\tilde{\theta}\right)_{k+1} + 2 \cdot \left(\tilde{\theta}\right)_k + \left(\tilde{\theta}\right)_{k-1}\right] \end{aligned} \qquad (2)$$

In Eq. (2) the time indices *{k+1, k, and k-1}* correspond to the current, previous, and previous minus one sampled data points, and Δt is the discrete time interval between data points. The numerically differentiated pitch angle data can lead to a noisy control signal, and Eq. (2) can be re-written to directly use the pitch rate output by the IMU. This reformulated control is

$$\begin{aligned} &\left(M_y\right)_{k+1} = \\ &\left(M_y\right)_k + K_p \cdot I_{yy} \cdot \left[\left(\tilde{\theta}\right)_{k+1} - \left(\tilde{\theta}\right)_k\right] + \\ &-K_d \cdot I_{yy} \cdot \left[q_{k+1} - q_k\right] + \\ &\frac{\Delta t}{2} \cdot K_I \cdot I_{yy} \cdot \left[\left(\tilde{\theta}\right)_{k+1} + \left(\tilde{\theta}\right)_{k-1}\right] \end{aligned} \qquad (3)$$

18. Filtered, Proportional Hover Control Law

The PID controllers were extremely sensitive to disturbances and gain selection, and small changes in the gains tends to excite pitch and roll axis gyroscopic coupling (caused by the rotating jet turbine). This coupling can result in an unstable platform controller. To expedite early flight testing in a near hover operational mode, a less complex control law was implemented for hover testing of the vehicle. This algorithm, while very sluggish with

regard to the allowable maneuvering performance, is highly robust and significant parameter variations can be performed without exciting the gyroscopic coupling.

This control algorithm uses only a proportional error feedback, and filters the commanded moment to insure a frequency significantly lower than the natural rotational frequency of the inner platform. The coupled filter tends to damp out noisy oscillations in the IMU attitude measurements. Also the low frequency, filtered commands do not tend to excite inter-axis gyroscopic coupling. Because the early tests were intended only to demonstrate the ability of the vehicle to achieve a stable hover condition, the sluggishness of the control command was not an issue.

The form of the hover control law assumes a second order filter of the form

$$\frac{d^2}{dt^2}M_y + 2\cdot\varsigma\cdot\omega_n\cdot\frac{d}{dt}M_y + \omega_n{}^2\cdot M_y = \omega_n{}^2\cdot I_{yy}\cdot K_p\cdot\tilde{\theta}. \quad (4)$$

In Eq. (4) ω_n is the natural radian frequency of the filter, and ζ is the damping ratio. When Eq. 4 is converted to the frequency domain and discretized, the resulting difference equation is

$$\left(M_y\right)_{k+1} = \frac{a^2}{b}\cdot\left(E_{k+1} + 2\cdot E_k + E_{k-1}\right) - \left(\frac{c}{b}\cdot\left(M_y\right)_k + \frac{d}{b}\cdot\left(M_y\right)_{k-1}\right). \quad (5)$$

In Eq. (5) the coefficients *a, b, c,* and *d* are

$$\begin{bmatrix} a = \omega_n\cdot\left(\frac{\Delta t}{2}\right) \\ b = 1 + 2\cdot\varsigma\cdot a + a^2 \\ c = 2\cdot\left(a^2 - 1\right) \\ d = 1 - 2\cdot\varsigma\cdot a + a^2 \end{bmatrix}. \quad (6)$$

19. End-to-End Gravity Offset and Thrust Vectoring Control System

Once the moment command is calculated by the control law, then a table-lookup of the data presented in Figure 20 are used to generate the pulse-width command for the servo. Figure 25 presents the end-to-to-end control law for a single control-axis. The onboard avionics necessary to perform the control calculations will be described in the next section.

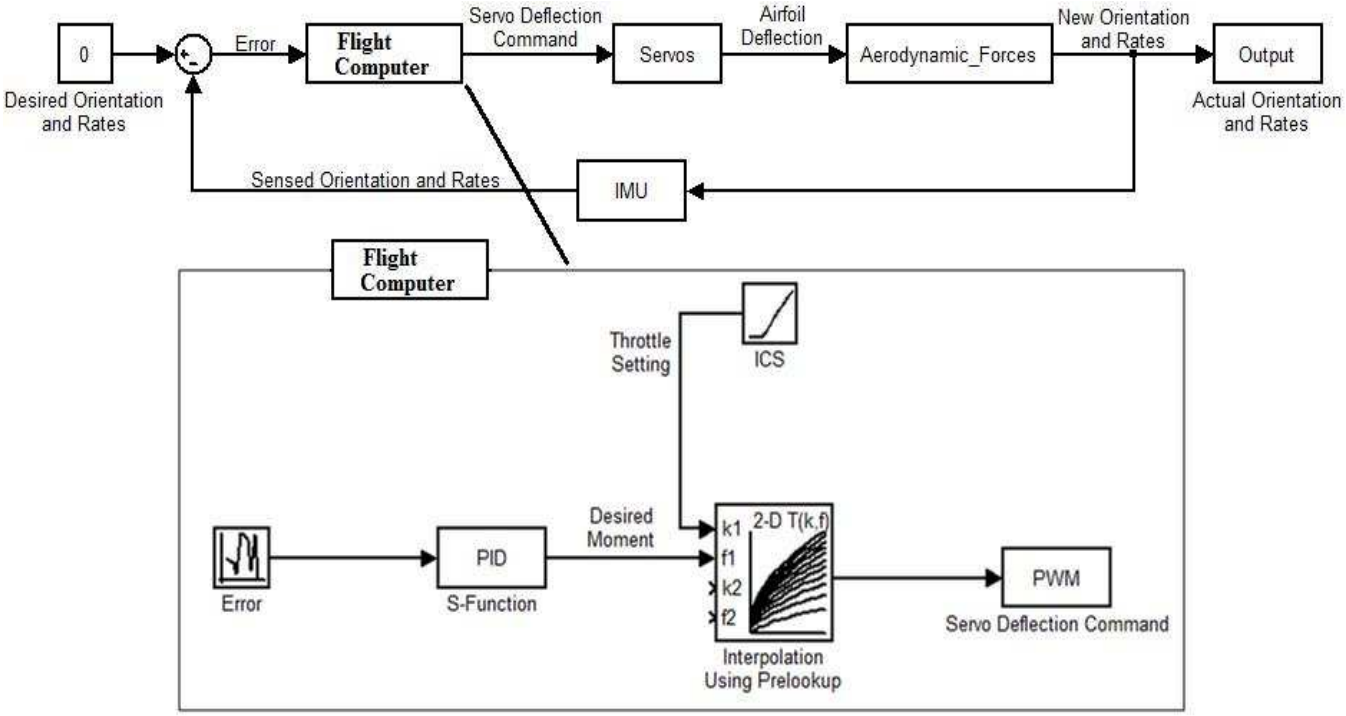

Figure 25. Closed-Loop Thrust Vectoring Control System for a Single Gimbal Axis.

20. Thrust Vectoring Avionics

Onboard thrust vectoring control law calculations and data flow management were controlled using a GumStix® micro-computer.[19] The GumStix is a 17 mm x 58 mm, 600 Mhz single-board computer that features the open-source Overo development platform. The name of the computer is derived from its small size. Figure 26 shows the Gumstix flight computer compared to the size of a package of chewing gum.

Figure 26. GumStix® Flight Computer

The Gumstix communicates externally through Blue Tooth or an 802.11 G wireless link. The computer also comes standard with 6 Pulse Width Modulation (PWM) I/O ports. The LPSLRV design leveraged both the built in wireless capability for down-link to the ground, and the native PWM ports to control both the engine throttle and vane servo commands. The Gumstix replaces the ground control unit typically used to control the JF-170 Rhino engine.

A ground-based laptop computer was used to communicate with the onboard GumStix flight computer via the wireless link. This laptop runs an interface program, written in the National Instruments Labview 2009® programming language[20] that allows direct control of all engine functions including built-in test diagnostics, startup, and throttle settings. The program also allows the controller gains and reference angles to be modified in real time and uplinked to the flight computer. Finally this program receives and logs pertinent flight data including the engine FADEC parameters, IMU outputs, and controller moment and vane deflection commands.

Figure 27 shows the power distribution to the thrust-vectoring avionics components on the inner gimbal platform. A 7.4 volt (two cell) Lithium-Polymer (Li-Po) battery supplies a 5-volt output Battery Elimination Circuit (BEC). This BEC regulates the output voltage and distributes power to the Gumstix, two servos, and a Universal Serial Bus (USB) hub modulates serial communications with both the IMU and the engine FADEC. The externally powered USB hub is required because the Gumstix cannot supply the current needed to power the IMU. The FADEC is powered by a separate 7.4 volt Lithium-Ion (Li-Ion) battery. The FADEC throttle control also receives power from the PWD signal generated by the GumStix.

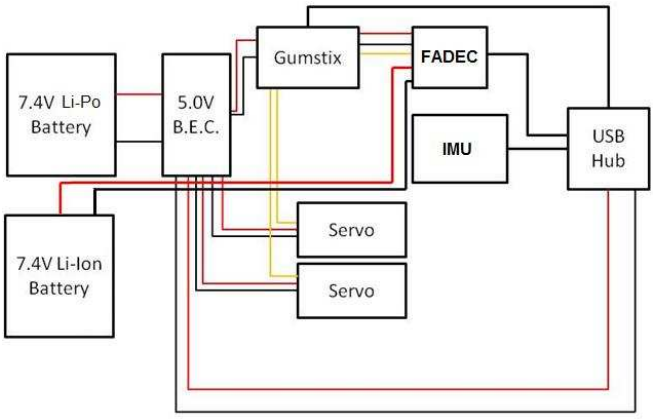

Figure 27. Inner Gimbal Platform Power Distribution Diagram.

W. Outer Platform: Vehicle Maneuvering System

As described earlier in the *Project Overview* section, the outer platform controls the horizontal and vertical accelerations of the vehicle, and offsets 16th of the total weight during hovering flight. A propeller driven quadrotor lift system was selected to maneuver the vehicle. The complete trade study that selected this approach is presented in Appendix G of Reference 11.

The original LLRV/LLTV design employed hydrogen-peroxide (H_2O_2) mono-propellant thrusters to maneuver and control the vehicle. The maneuvering thrusters were grouped in clusters of 4 90-lbf thrust rockets, and were positioned at the "corners" of the vehicle. After the jet engine had throttled-up enough to simulate lunar gravity, the LLRV's vertical movements were controlled by two 500 lbf thrust rockets mounted in the center, next to the engine. The flow of pressurized H_2O_2 was systematically turned on or off allowing very crisp attitude control, similar to was eventually experienced by the Apollo astronauts when landing the Lunar Excursion Module (LEM) on the moon.

Figure 28 shows the locations of the maneuvering thruster banks on the LLRV.

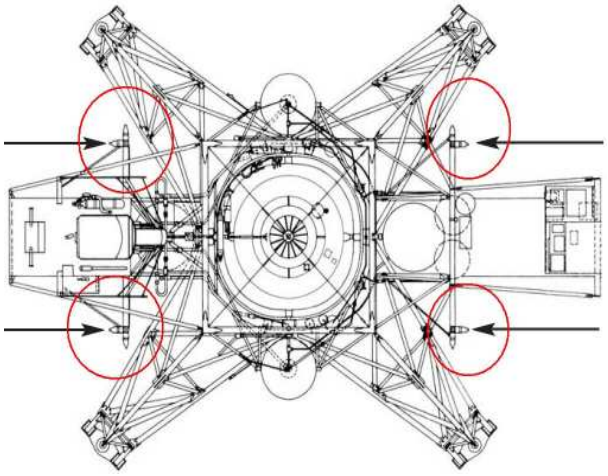

Figure 28. Maneuvering Thrusters Banks on LLRV.

A maneuvering platform design similar to the LLRV was initially considered. However, personnel safety and environments hazards associated with mono-propellants thrusters made this design infeasible for a free flying vehicle not operating on a restricted government test range. Cold gas thrusters were also considered, and deemed to be feasible. The mass of cold-gas propellant and associated storage hardware required for supporting 1/6th of the weight of the vehicle during flight was more than the remaining vehicle weight.

An option where the jet engine supports nearly all of the vehicle weight and cold gas thrusters were used only for maneuvering were also considered. This option, while technical feasible, could not accurately reproduce the "feel" of landing in a reduced gravity environment. This design will not satisfy one of the basic requirements for the vehicle and basically defeats the purpose of the experiment.

When the one-academic year time table and the allowable hazard levels were thoroughly considered, the most suitable option for the LPSLRV's attitude control and maneuvering lift, was a quadrotor propelled vehicle outer platform. Although quadrotor designs are known to be notoriously difficult to control,[21,22] the recent proliferation of sophisticated microcontrollers has allowed the development of several suitable commercial digital "fly-by-wire" controllers. It was concluded that employing one of these commercial design would allow for a feasible design whose closed-loop dynamics could be tuned to fly in a manner approximating a reduced gravity landing vehicle.[23]

21. Rotor Layout on the Quadrotor System

The quadrotor system design for the LPSLRV attempts to match the general layout of the LLRV thrusters, and provides the means to maneuver the craft up, down, forward, back, left and right with the use of four propellers. A quadrotor is an aircraft propelled by four independently operating rotors. Unlike helicopters, quadrotors can use fixed-pitch blades -- blades whose angle of attack does not vary as the blades rotate – to achieve precise flight maneuvering. Control of vehicle motion is achieved by modulating the rotational speed of each rotor to vary thrust and torque produced by each rotor.

Figure 29 depicts the rotor layout on the outer platform support-structure. The circular arrows superimposed on each rotor show the direction of rotation. In this design the front and aft propellers (1-4) rotate in opposite directions from the port and starboard (2-3) propellers. This counter-rotating scheme allows for precise control and trim of the vehicle yawing rate. A left-to-right (2-3) differential throttle produces a rolling moment about the center of the platform and front-to-aft (1-4) differential throttle produces a pitching moment. Collective throttle (1,2,3, and 4) is used for vehicle to climb and descent.

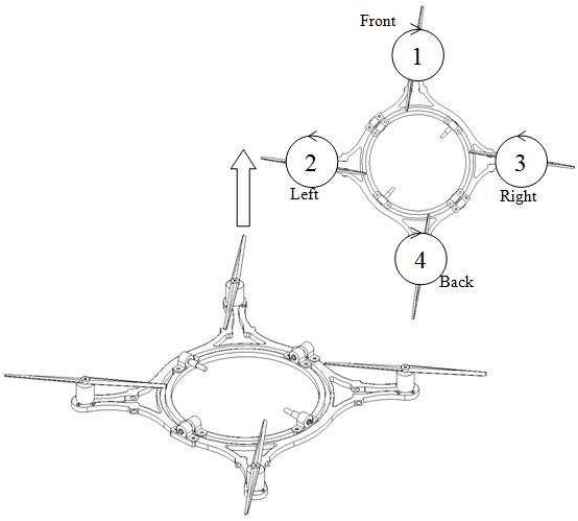

Figure 29. Quadrotor Propeller Layout.

Table 10 shows the simple throttle control logic used to generate a desired flight motion. The "up arrow" indicates an increase in the throttle level, while the "down arrow" indicates a decrease in throttle level.

Table 10. Throttle Mixing Command Logic

	Rotor Identification of Increase(↑) or Decrease(↓) Torque			
Desired Motion	1	2	3	4
Pitch (Forward)	↓	-	-	↑
Pitch (Backward)	↑	-	-	↓
Yaw (Clockwise)	↑	↓	↓	↑
Yaw (Counter)	↓	↑	↑	↓
Roll (Right)	-	↑	↓	-
Roll (Left)	-	↓	↑	-
Up	↑	↑	↑	↑
Down	↓	↓	↓	↓

22. Rotor Selection

A project-developed blade element/momentum theory computer code was used to determine the required size, pitch, and operating RPM for the rotors. The blade-element code was created to provide a starting point on rotor, motor selection, and allowed a baseline assessment of the power requirements of the system. The blade element technique is described in detail in Appendix B of this report. Analytical predictions were also supported by test stand characterization. Experimental apparatus and test procedures may be found in Appendices G and I of Ref 11.

Following an extensive trade study, (Ref. 11, Appendix G) the LPSLRV team selected *13 in.* diameter, *6.5 in.* pitch propellers manufactured by Advanced Precision Composites Corporation.[24] Figures 30a and 30b compare the predicted and measured thrust and direct-drive braking power for these propellers. At full throttle, (~6400 RPM) the tip velocity of these propellers is approximately *100 m/sec*, so transonic tip-drag losses are not an issue.

23. Rotor Drive Mechanism

The relatively high thrust provided by the APC rotors at low RPM allowed a direct drive system to be employed in the LPSLRV design. A small brushless RC motor manufactured by Hacker Inc,[25] A30-10XL, was selected for the drive train. Brushless motors, because they have no commutation ring, are "spark free" and produce minimal electromagnetic interference when compared to conventional brushed motors.

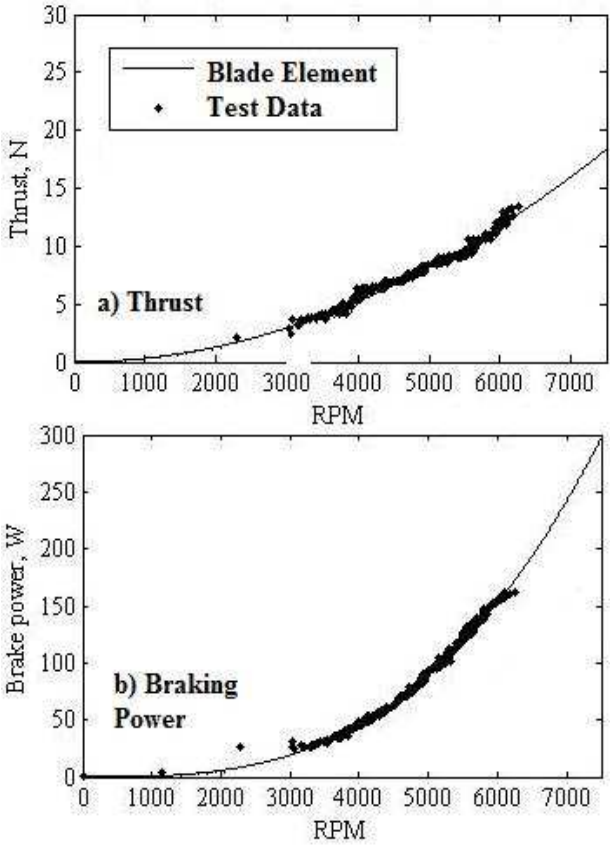

Figure 30. APC 13 x 16.5 in. Rotor Performance.

When one considers the volatile jet fuel mounted on the center platform, and the WiFi communications link to the jet engine control and telemetry systems, these *spark-free* motor properties are highly desirable. The matched electronic speed controller (ESC) recommended by the manufacturer is the Hacker X55-SB-Pro. The ESC receives a PWM command from the radio receiver/transmitter, and translates this command into an appropriate drive voltage level for the motor. Table 11 lists key motor properties. Figure 31 shows the motors and rotors as mounted on the outer maneuvering platform.

Table 11. Hacker A30-10XL Motor Properties.

Power (Torque) at 10 Newton Thrust Level (13 x 16.5 in rotor) 137 W (0.194 N-m)	RPM at 10 Newton Thrust Level (13 x 16.5 in rotor) 6750
Motor Peak Power	650 W
Motor KV	900 RPM/Volt
Stall Torque	0.621 N-m

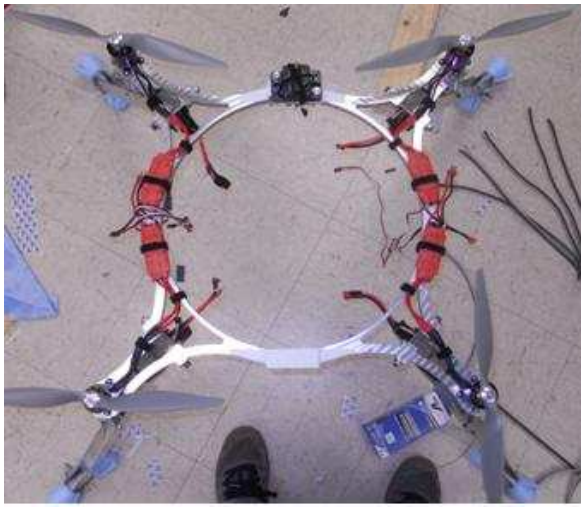

Figure 31. Quadrotor Maneuvering Platform.

24. Outer Platform Control System

Initially, it was thought that the quadrotor system could be flown open-loop using a conventional RC receiver/transmitter designed for model aircraft. Following the procedure developed by Ref. 23, the throttle, rudder, aileron, and flap controls were internally re-mapped to control the 4 motor throttle levels. This mapping allowed, at least in theory, the quadrotor to be flown as if it were a conventional RC aircraft. Figure 32 and Table 12 show this transmitter re-mapping scheme.

This open-loop control mixing scheme resulted in a quadrotor configuration that was essentially unflyable. The transmitter control signal latencies were so large that the rotational rate onsets could not be negated by pilot input alone. Closed-loop platform control, hosted locally on the vehicle, was required to maintain outer platform stability.

Fortunately, a commercially-available control and logic board specifically designed for quadrotor systems was available to perform the stabilization and control function. This device, the QuadPowered Control™, is manufactured by Quadpowered Precision Control Systems Company,[26] The QuadPowered system limits vehicle rotation rates using a PID feedback-control system. Feedback sensors include a two-axis rate-gyro for the pitch and roll axes, and a single axis rate gyro for the yaw axis.

Three independent control loops are executed by a microprocessor installed on the board. The microprocessor receives throttle, pitch, roll, and yaw signals from a standard RC transmitter, mixes the commands appropriately, and sends out a PWM signal to each of the 4 rotor ESCs. Figure 33 pictures the baseboard, and presents a functional block diagram of the QuadPowered board control logic.

Table 12. Transmitter Re-mapping of Throttle Commands

	Transmitter Re-mapping of Increase(↑) or Decrease(↓) Signal to the Motors			
Desired Motion	Throttle	Aileron	Elevator	Rudder
Pitch (Forward)	↓	-	-	↑
Pitch (Backward)	↑	-	-	↓
Yaw (Clockwise)	↑	↓	↓	↑
Yaw (Counter)	↓	↑	↑	↓
Roll (Right)	-	↑	↓	-
Roll (Left)	-	↓	↑	-
Up	↑	↑	↑	↑
Down	↓	↓	↓	↓

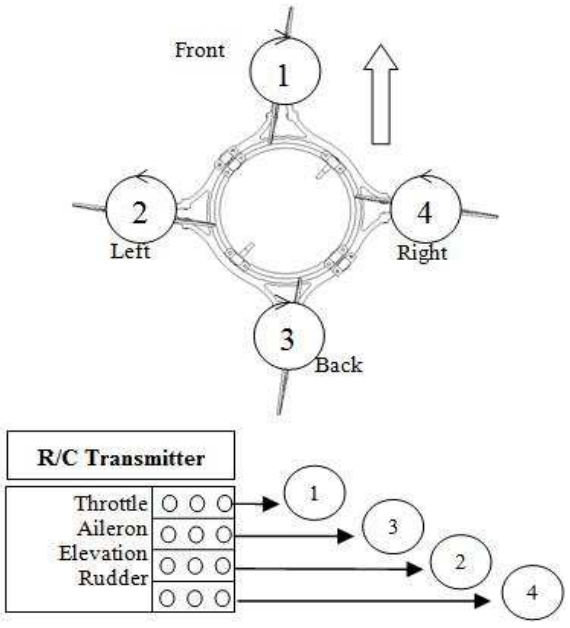

Figure 32. Throttle Mixing Scheme.

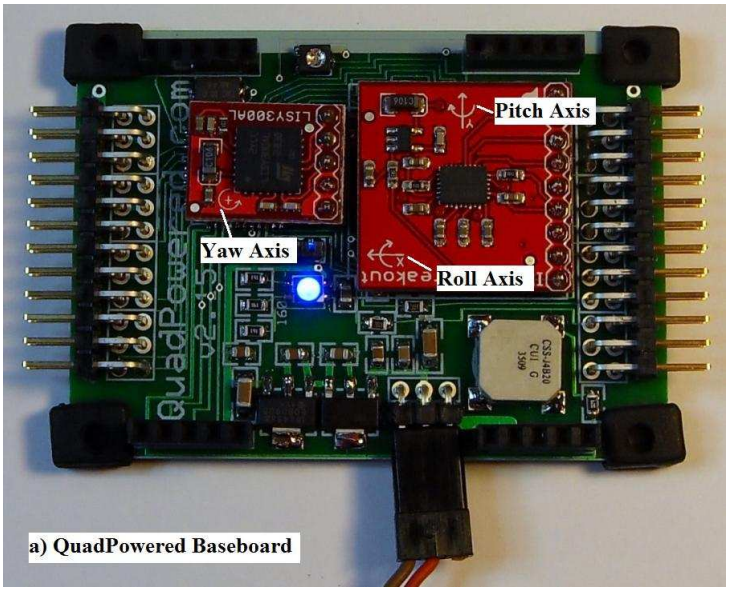

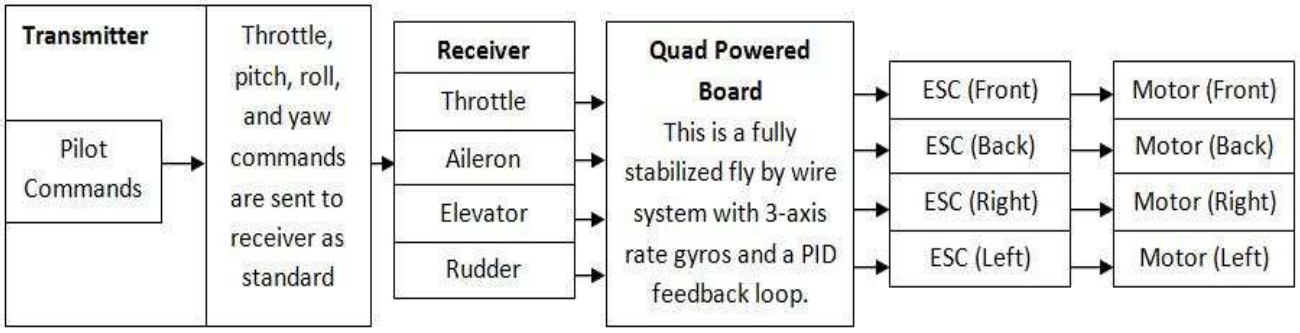

b) Functional Block Diagram

Figure 33. QuadPowered Control Systems Board.

25. Outer Platform Power Distribution System

All components for the maneuvering system were arranged on the outer platform ring. Figure 34 presents a block diagram of the outer platform power distribution system. The outer platform is powered by 4 x 3-cell lithium-polymer (Li-Po) batteries operating at a nominal 11.4 volts. The positive and negative terminals for each batter were connected to a separate power hub creating a parallel circuit. This arrangement provides uniform voltage to the Electronic Speed Controllers (ESC) for each motor. This design eliminates the possibility of one motor receiving a higher voltage, thus producing more thrust, than the other three motor.

The QuadPowered board receives power from two sources, the power hub, and power from one ESC that has an integrated 5 volt BEC in series with the ESC drive signal. The RC transmitter/receiver is powered by the QuadPowered board through a three pin connector. A safety switch – a marine grade circuit breaker rated to 150 amps -- was added to the power circuit to allow the QuadPowered board and all 4 ESCs can power-up simultaneously. This simultaneous power-up is necessary for proper hardware and software initialization. Figure 35 shows the switch as integrated onto the outer platform (inset image).

Because the outer platform maneuvering motors draw substantial current -- a maximum of 40 Amps total -- proper wire gauge selection was critical. Too high of wiring gauge could result in harness damage under maximum load; too low of wiring gauge adds considerable wiring volume and weight to the already crowded outer platform. Fortunately, as the motors are operating there is a constant flow of air across airframe resulting from rotor downwash. The convection from this rotor downwash has the effect of dissipating substantial heat from the lead wires to the motors and allowed 12 AWG wire (rated only for 30 Amps) to be used in lieu of 10 AWG wire. This substitution reduced the total wiring weight

substantially – nearly 0.5 kg. Extensive ground and flight testing verified that the 12 AWG wires could withstand the current draw required for fight maneuvering.

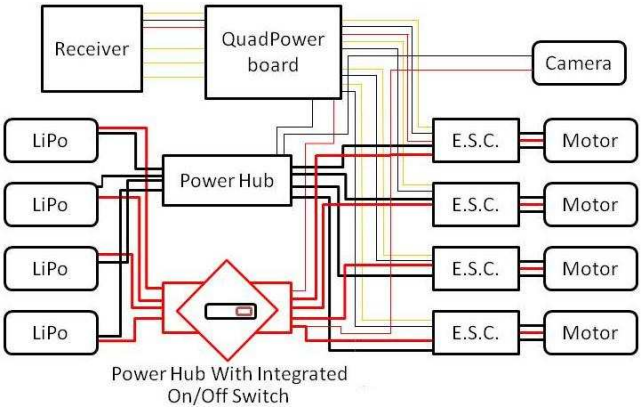

Figure 34. Outer Platform Power System Wiring Diagram.

Figure 35. Outer Platform Power-Up Switch/Circuit Breaker.

X. Vehicle Structure

The structure went through many design iterations to reach its final configuration. This section presents the final structural design. A detailed description of the design evolution is presented in Ref. 11, section 6.0. All components were designed to structurally survive a one-meter vertical drop with a load margin of safety of 2.25. The entire structure, except for the landing gear and fuel tank platform was constructed from ½ inch 6061 T-6 aluminum. Figure 13 shows the final structural design.

There are three primary structural features, 1) landing gear, 2) the outer platform, and 3) the inner platform. As described earlier, the inner and outer platforms are connected by pitch and roll gimbals that transmit translational forces but no moments. The gimbals complete the requirement of decoupling the gravity offset from the outer platform. The landing system has spring-loaded legs to allow for soft landings when the vehicle doesn't necessarily make a smooth landing. All the auxiliary items for the gravity offset are located on the inner gimbal to properly simulate flying in a 1/6 gravity environment. Similarly, all the auxiliary items for the maneuvering controls are located entirely on the outer platform.

26. Landing Gear Design

Figure 36 shows the landing gear strut design. An aluminum I-bean shape was selected for the struts in preference to a more conventional tubular design to accommodate mounting of the 11.4 Volt batteries Li-Po batteries used to drive the maneuvering motors. A stock size was selected so that the batteries would fit snugly into the I-beam slots of the strut. This design feature has the beneficial effect of lowering to overall center of gravity of the vehicle -- thus increasing the hover stability – and reducing the physical volume of components mounted to the outer platform clover leaf structure.

Wheels attached to the bottom of the legs allowed travel outward during landing. This feature gives the vehicle a larger and more stable landing footprint. The spring-loaded shock absorbers are commercially available, and were originally designed for small RC-toy cars and trucks.

Figure 36. Landing Gear Strut Design.

27. Outer Platform Structural Design

To minimize the effects structural interference and disruption of the rotor down wash (and reduction of the produced lift), the outer platform was designed to have a clover leaf shape with the rotors located at the ends of the leaves. Figure 37 shows this design.

Figure 37. Outer Platform for Clover Leaf Design.

The design and optimization of the outer platform was completed using Altair Engineering's HyperWorks® suite.[27] The HyperWorks® suite provides a finite element analysis method (FEM) environment capable of analyzing structural configurations numerically or using reduced-order explicit methods. Altair engineering provided the HyperWorks® suite of programs free of charge to the LPSLRV design team.

With all of the gravity offset auxiliary items placed on the inner gimbal, the need for surface area on the outer platform was greatly reduced, and this factored was considered in the structural optimization process. An initial "blocky" version of the clover-leaf design was presented to HyperWorks® and analyzed. Specific design constraints included setting the maximum deflections, setting a maximum allowable stress, and specifying minimum member sizes to prevent a spider web of structural components. Once the constraints were specified, the HyperWorks® FEM program optimized the clover leaf contour line to minimizing the amount of material required.

28. Inner Platform Structural Design

As mentioned previously, in the introduction to this section, the inner platform is partially decoupled from the outer platform by pitch and roll gimbals. All of the gravity-offset and thrust vectoring components are located on the inner gimbal. The fuel tank and engine mount was directly integrated onto the inner gimbal. The tank was constructed with interior baffles to reduce fuel sloshing during maneuvering flight. The tank was designed in an annular fashion with the jet engine inserted on the interior of the annulus, and the pitch axis bearings press fit into the top of the tank structure. The fuel tank was walls and baffles were constructed from ¼ inch 6061 T6 aluminum plate. The top surface of the tank serves as the inner platform and was built from ½ 6061 T6 aluminum plate. At full capacity the tank holds approximately 1.66 kg of fuel. Figure 38 shows the fuel tank structural design.

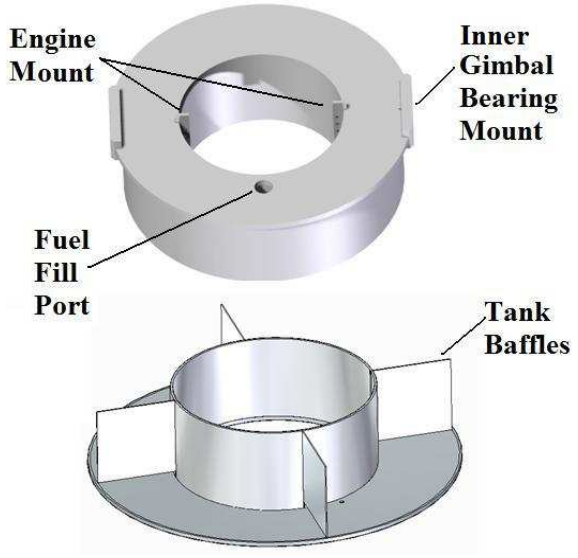

Figure 38. Fuel Tank Design.

Y. Vehicle Mass Budget

The vehicle design was initiated by allocating percentages of the total vehicle mass to the various design teams. The total allowable vehicle mass was estimated at $6/5^{th}$ of the JF-170 Rhino thrust at 80% throttle, based on the manufacturer's thrust curve. The engineering estimates for initial mass fractions were derived from the original LLRV vehicle layout.

Table **13** presents the original mass budget allocations.

As the design progressed, the distributions of mass were updated to accommodate each of the design group needs. Table 14 shows the mass distribution of the final design. Some of the mass allocation categories changed as the vehicle design matured. For example, the recovery system was analyzed and determined to be too mass costly and expensive. This feature was deleted from the overall design.

Amazingly the mass percentages changed only slightly and the final fully-fueled vehicle mass, 32.87 lbm, is under the original vehicle mass estimate. The thrust reduction from the original thrust curve -- caused by the thrust vectoring system – requires the engine to be operated between 85% to 90% throttle to achieve a true $5/6^{th}$ *g* initial weight offset. This throttle level is moderately higher than the originally desired 80% throttle level; but is well within the operating range of the JF-170,

Table 13. Initial Mass Allocation for Vehicle

Subsystem	Percent of Total Mass	Mass (kg)	Mass (lbf)
Structures	21	2.5	5.51
Safety	8	1	2.21
Controls	8	1	2.21
Instrumentations	8	1	2.21
Power	21	2.5	5.51
Aerodynamics	18	2	4.41
Buffer	16	1.87	4.12
Total (Less Motor and Fuel)	100	11.87	26.17
Maximum Total Allowable		15.53	34.24

Table 14. Final Mass Distribution for Vehicle

Subsystem	Percent	Mass (kg)	Mass (lbf)
Structure	40.58	6.05	13.32
Controls	3.35	0.50	1.10
Instrumentations	6.71	1.00	2.21
Power	11.00	1.64	3.60
Quad-Rotor	7.98	1.19	2.65
Jet Engine Accessories.	8.79	1.31	2.88
Engine	10.46	1.56	3.50
Fuel (4.8 min @85-90% throttle)	11.13	1.66	3.67
Total	100	14.91	32.87

VI. Budget and Schedule

Budget and schedule constraints for this project were primarily dictated by the 1 academic year design cycle for the senior design class; and the initial funding provided by NASA ESMD. The final expenditures were approximately $4011 larger than the budget originally allocated for the project. This overage was primarily a result of higher hardware and materials expenditures ($22,146) than was originally anticipated ($18,000). The deficit was back-filled using discretionary funds from the faculty mentor for the project and course instructor.

This project was extremely ambitious, and achieving all of the design and test objectives was a daunting task. The schedule ran slightly longer than a single academic year with the complete design closure not occurring until the last week of March. Integration and verification testing spilled over into late May and the first flight did not occur until mid to late June. The academic year at Utah State University ended on May 8, 2010. Following the end of the academic year, testing and integration was performed by the faculty advisor, paid research assistants, and volunteer student help. Details of the flight tests will be documented in a separate flight test report. This test report will serve as a complement to the course handbook

Z. Budget

The NASA budget was augmented using several additional sources. These sources included cash donations from the USU Space Dynamics Laboratory (SDL), the Utah AIAA section, the USU College of Engineering, the NASA Space Grant Higher Education Project, and re-allocated salary from the faculty mentor. Altair Engineering of Draper Utah donated two student-license seats to its Hyperworks® structural optimization computer code. Petersen Engineering of Farr West, Utah donated more than 100 hours of Machine shop time. Both non-cash contributions were considered essential to the success of this project.

Expenditures associated with the project include 1.5-months faculty salary compensation, funding for 3 full time research/teaching assistants, student travel for training, faculty travel associated with the project and course material development, and of course the hardware components necessary to fabricate the vehicle. All undergraduate team members taking the class for design credit were unpaid. Table 15 itemizes the budget credits and expenditures.

Table 15. Budget Itemization.

Receipts	
From	**Total Amount**
NASA ESMD	$55,000
SDL	$5,000
USU College of Engineering	$5,000
Utah Section of AIAA	$1,500
Total	***$66,000***
Expenditures	
Item	**Amount**
Faculty Salary and Student Salaries	$23,738
Fringe benefits and Insurance	$8800
Travel and Training	$7400
Facilities and Administration (11.9%) of ESMD funds	$5477
Hardware and Materials	$22,146
Software and Licenses	$2450
Total	***$70,011***

AA. Project Schedule

Figure 39 shows the original proposed schedule, and shows the final schedule as it was updated at the end of the academic year.

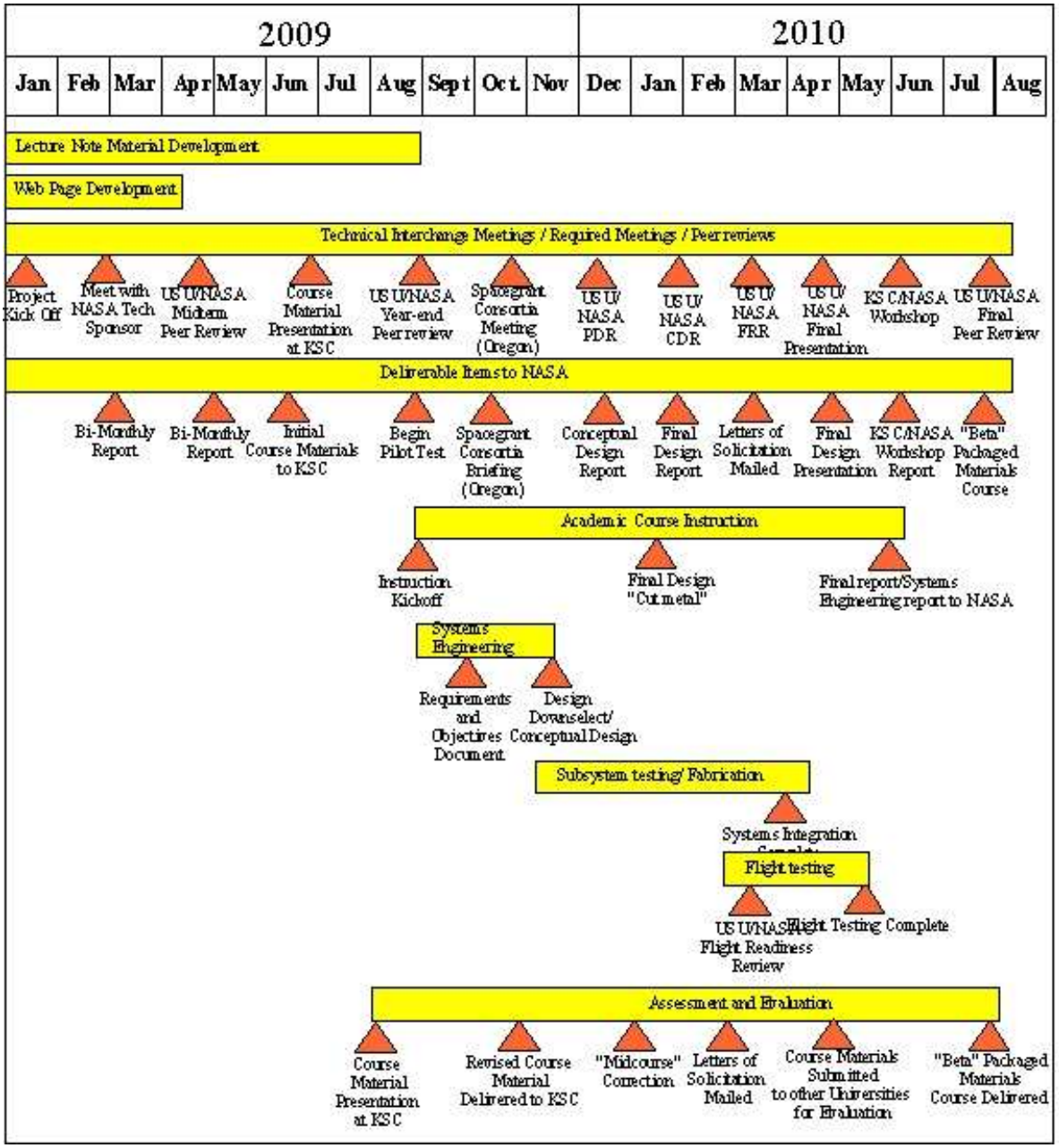

Figure 39. Original Proposed Project Flow and Milestone Schedule.

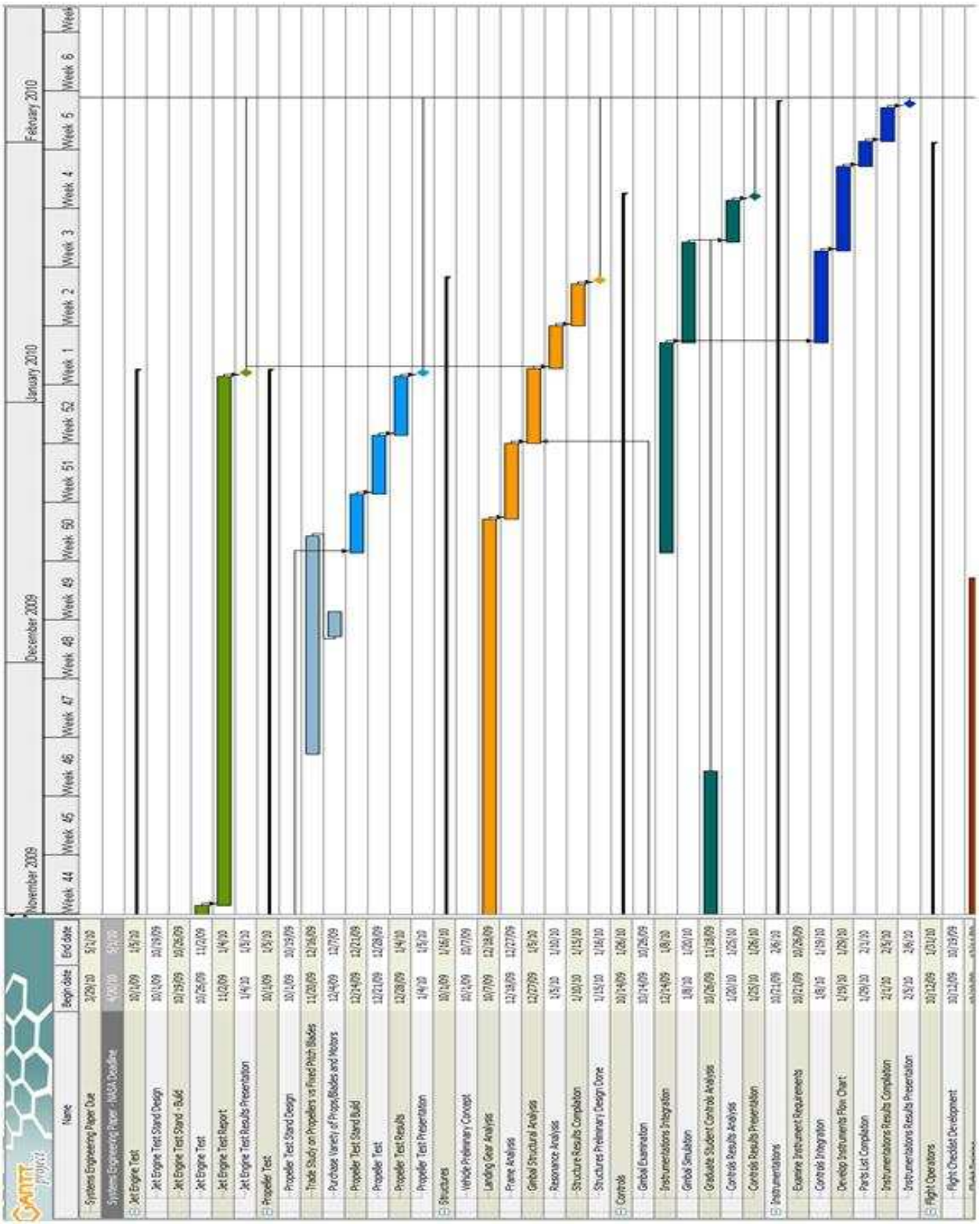

Figure 40. Final Project Flow and Milestone Schedule, May 5, 2010.

VII. Summary and Concluding Remarks

The Lunar and Planetary Surface Research Vehicle (LPSLRV) is a new senior project that was taught at Utah State University (USU) for Academic year 2009-2010. The two-semester sequence complements both the ESMD Senior Design and ESMD Faculty projects, and was developed as a "packaged" senior design course that can be incorporated into university curricula across the USA and Puerto Rico. The associated course materials described in this handbook detail the systems engineering processes that were developed, how these processes were applied, and the examples of results, outcomes, and measures of effectiveness are presented.

This project designed and built a free flying research vehicle that reproduces many of the capabilities demonstrated by the 1960s-era Lunar Landing Research and Training Vehicles (LLRV/LLTV). The approach for this project is – whenever possible – to replace 1960s-era analog designs with proven and reliable modern digital computer-aided technologies. This sub-scale vehicle simulates the reduced-gravity using a vertically-thrusting jet engine to partially offset the vehicle weight. The vehicle is formally designated as the Lunar or Planetary Surface Landing Research Vehicle (*LPSLRV*) and was nicknamed the "Flying Rhino."

This project includes elements of all four of the critical technology thrusts identified by ESMD as key for the future of space exploration. These areas include spacecraft systems, propulsion, lunar and planetary surface systems, and ground operations. The complexity of the design – building an actual flying vehicle – required a large interdisciplinary team to be assembled. The size of the team – 7 graduate research assistants, 19 undergraduate student design team members and a faculty mentor – required that system requirements and team roles and responsibilities were clearly defined. Formal systems engineering techniques were applied to facilitate this progress.

There are three primary structural features for the vehicle, 1) landing gear, 2) the outer platform, and 3) the inner platform. The landing system has spring-loaded legs to allow for soft landings when the vehicle doesn't necessarily make a smooth landing. The inner and outer platforms are connected by pitch and roll gimbals that transmit translational forces but no moments. This arrangement simulates the effect of flying in a reduced gravity environment,

Stability of each platform is controlled independently by two separate flight control systems. The outer gimbal-ring holds all of the maneuvering rotors, associated drive-train components and control system. The inner gimbal ring holds the jet engine and associated equipment. The inner platform pitch and roll angles are controlled by a thrust vectoring system featuring exhaust turning vanes. The fuel tank for the jet engine is integrated into the structure of the inner ring.

This project was extremely ambitious, and achieving all of the design and test objectives within the time and budget constraints of a university-based senior-design project was a major challenge. The schedule ran slightly longer than a single academic year with the complete design closure not occurring until early April. Integration and verification testing spilled over into late May and the first flight did not occur until mid to late June. The academic year at Utah State University ended on May 8, 2010. Following the end of the academic year, testing and integration was performed by the faculty advisor, paid research assistants, and volunteer student help.

The final expenditures were approximately $4011 larger than the budget originally allocated for the project. This overage was primarily a result of higher hardware and materials expenditures ($22,146) than was originally anticipated ($18,000). The deficit was back-filled using discretionary funds from the faculty mentor for the project and course instructor.

VIII. Appendix A: Ground Testing and Systems Verification

This section details the ground tests used to characterize and verify the vehicle maneuvering and gravity offset subsystems. The maneuvering system ground test apparatus and results will be briefly presented first. This subsection will be followed by a detailed description of the ground tests used to characterize the static thrust and thrust vectoring effectiveness of the gravity offset system. Finally results from ground combined system tests (CST) for the entire vehicle will be presented. The CST was performed on the entire vehicle configured for flight, but strapped to ground to keep the vehicle from lifting off.

BB. Rotor Static Thrust Tests

As mentioned earlier, a project-developed blade element/momentum theory computer code (derived in Appendix B) was used to determine the required size, pitch, and operating RPM for the rotors. The blade-element code was created to provide a starting point for selecting the rotors and drive motors. Additionally, this code was used to calculate the initial power requirements of the system. Analytical calculations allowed the suite of available propellers and drive systems to be reduced to a "short list." Rotors on this list were tested and characterized to allow down selection to the final rotor system as described in the previous section.

29. Rotor Static Thrust Stand Description

Figure 41 shows the test stand developed to characterize the rotors and drive mechanisms. On this stand 4 Omegadyne LCCA-25 load cells (25 lbf compressive or tensile load capacity) were used to measure the thrust from each of the 4 rotors, and a Shimpo DT-209X optical angular speed sensor was used to directly measure the RPM of the rotors as a function of the throttle setting. The current drawn by the motor was sensed using a Fluke i30 Inductive Clamp-type current-sensor. Loads, current clamp output, and motor lead input voltages were sensed using a stand-alone National Instruments 6009 14-bit Universal Serial Bus (USB) Data Acquisition (DAQ) device. DAQ outputs were recorded by a laptop computer. Relevant manufacturer's specifications for operating range and accuracy for each of these instruments is listed in Table 16.

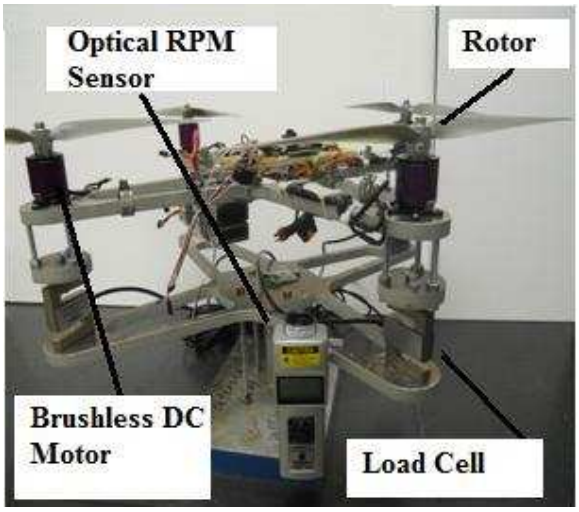

Figure 41. Rotor Static Test Stand.

Table 16. Manufacturer Specifications for Rotor Static Thrust Stand Instruments.

Instrument Model	Operating Range	Accuracy
LCCA-25 *(Thrust Loads)*	±25lbf (_111.2N)	±0.037% of Full Scale
Shimpo DT-209X *(RPM)*	6-99,999 RPM (0.63 – 20,943 rad/sec)	±0.0.006% of Reading
Fluke i30 *(Current)*	±0-40 Amp	±1% of Reading
USB-6009 *(Data Acquisition)*	±10V	±0.5 m VRMS, 14-bit resolution

30. Rotor Static Thrust and Braking Power Test Results

Figure 42 shows a typical time history of motor thrust and the current drawn by a single Hacker A30-10XL drive motor with the 13 x 6.5 in APC propeller installed. This profile shows the variation in current when the throttle command is varied from 0 to 100%, and back down. The maximum current load is approximately 38 amps. Sensed current and voltage were used to calculate power consumed as a function of throttle. Since direct drive gearing was used (assuming minimal power loss by the motors) the consumed power is equated to the braking power of the propeller.

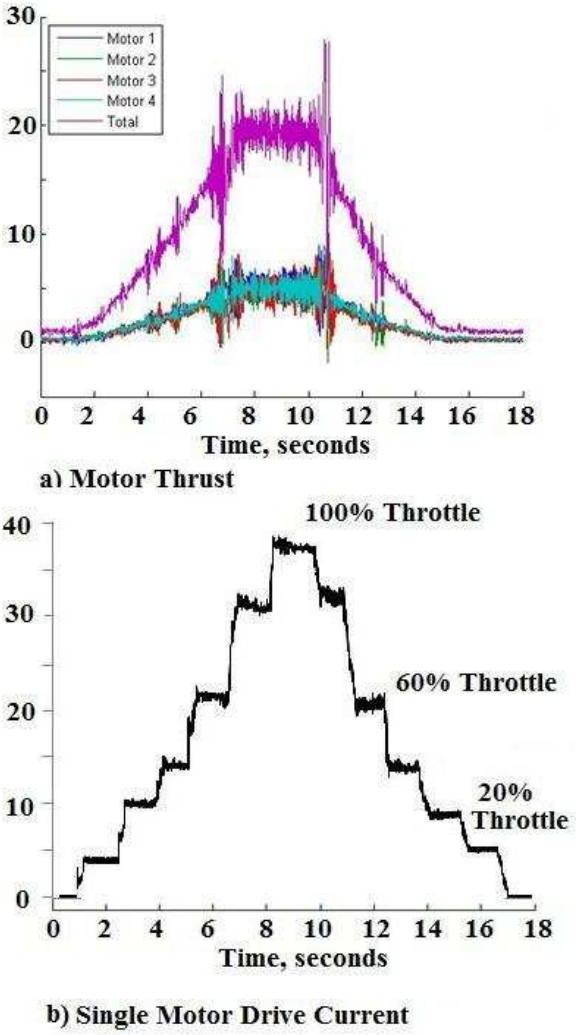

Figure 42. Thrust and Single-Motor Current for Throttle from 0 to 100%, 13 x 6.5 in. APC Propeller.

Figure 43 compares the predicted and measured thrust and direct-drive braking power for these propellers to the blade element code predictions. Figure 43a plots the thrust delivered by a single rotor, and Fig. 43b plots the braking power. The comparisons are very close and verify blade element calculations.

At full throttle, (~6400 RPM) the tip velocity of these propellers is approximately 100 m/sec so transonic tip-drag losses are not an issue. Operating at 50% throttle (~4800 RPM), each rotor is capable of lifting approximately 7.5 Newtons (1.69 lbs). Thus 4 rotors collected can lift approximately 30 Newtons (6.74 lbs). This lift capacity is 20-25% of the total vehicle weight. This excess lift capacity gives a wide margin for the QuadPowered Board's feedback control without fear of saturating a throttle control during maneuvering flight. The 80 watts of braking power required for each motor at 50% throttle is equivalent to approximately 19 amps of sustained current draw. This current draw equates to approximately 10 minutes flight time on the 3.25 amp-hour Li-Po batteries.

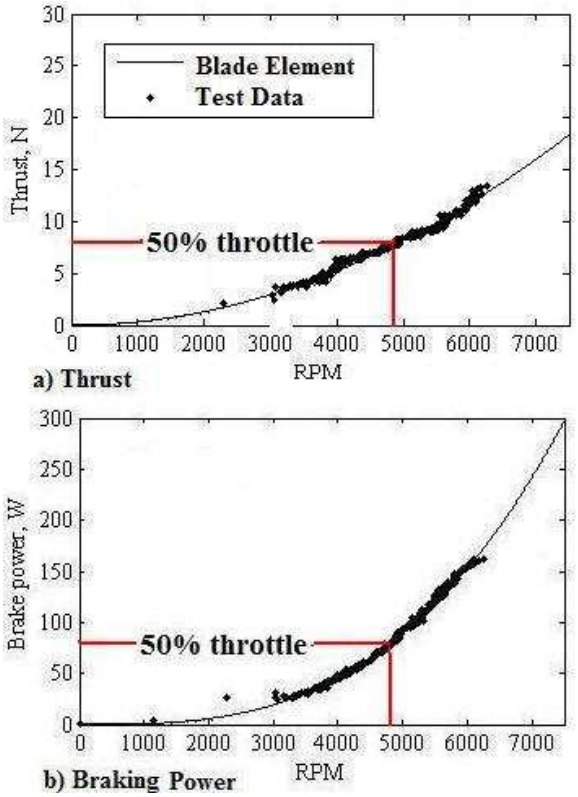

Figure 43. APC 13 x 16.5 in. Single Rotor Performance.

CC. Jet Engine Static Thrust Tests

The following sections discuss the static thrust and thrust-vectoring tests conducted to characterize the JF-170 engine. All engine static tests were performed in the Engineering Technology department's *Jet Engine Test Cell* on the Utah State University campus. For the jet-engine static thrust tests, commercially available test stands were examined and found to be excessively expensive and have structural support mechanism that were unsuitable for mounting to the JF-170 rhino geometry. Consequently, a custom-made, portable, test stand was designed and built to support the needs of the LPSLRV project.

31. Jet Engine Static Thrust Stand Overview

The test stand features a 6-degree-of-freedom (6-DOF) load balance, a traversing engine exit plume

Pitot probe, a static pressure port at the nozzle exit, and a digital scale to measure fuel consumption during the tests. Figure 44 shows an image of the test stand and defines the coordinate system. The thrust stand is designed so that the engine exhaust plume exits vertically, and the thrust acts downward into the test cart. Figure 45 shows the test support cart. The coordinate system is described in detail in the next section.

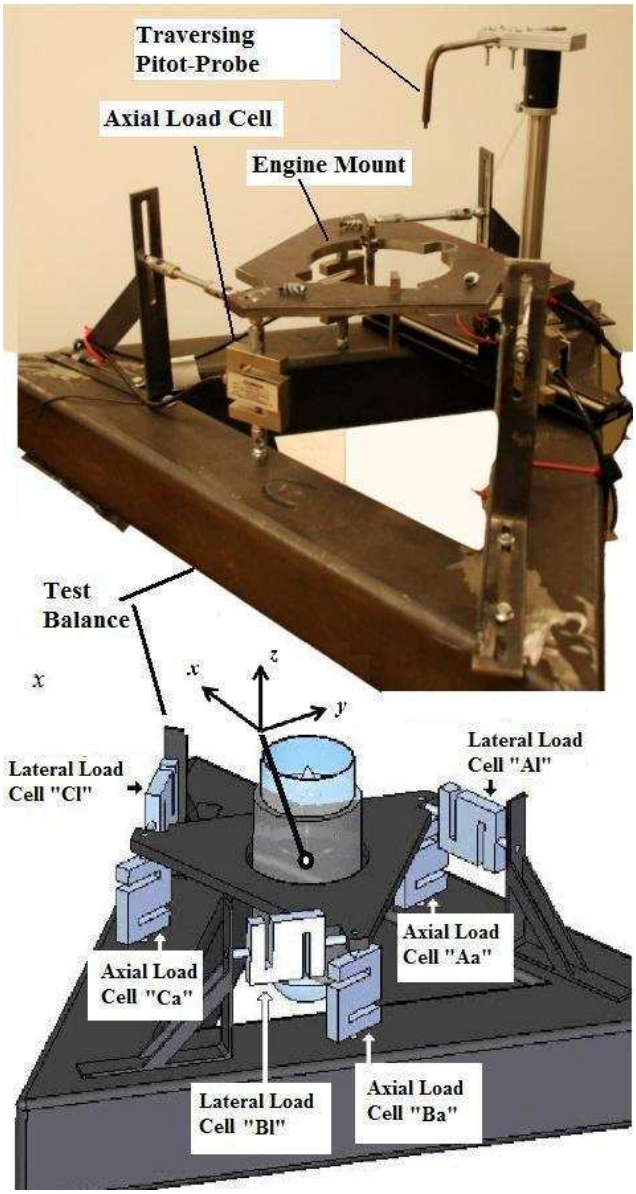

Figure 44. Jet Engine Thrust Stand.

Three axial and three lateral load cells are incorporated into the stand to facilitate the force measurements. Axial loads are sensed with three Omegadyne® model LCCD-100 load cells, while lateral loads are sensed with Omegadyne LCCA-25 load cells. The stagnation pressure from Pitot-probe is sensed with a 0-30 psia absolute Omegadyne PX-142 pressure transducer. The static pressure at the nozzle exit plane is sensed with an identical transducer ranged from 0-15 psia. The load cells and pressure transducers are connected to three National Instruments® model NI-USB-6009 14-bit stand-alone DAQ devices. Three DAQ devices are necessary to provide the required 6 differential and 2 single ended channels for the load cells and pressure transducers.

The fuel mass was measured using a Weighmax® model W-C03 scale. The RS-232C digital output from this scale was monitored during testing to provide a continuous measure of the fuel consumption rate. A laptop computer running NI Labview 9.0 was used to capture, synchronize, process, and log data from the load cells, pressure transducers, and serial output data from the scale. Relevant manufacturer's specifications for operating range and accuracy for each of these instruments is listed in Table 17.

Table 17. Manufacturer Specifications for Static Thrust Stand Instruments

Instrument Model	Operating Range	Accuracy
LCCA-25 *(Lateral Loads)*	±25lbf (_111:2N)	±0.037% of Full Scale
LCCD-100 *(Axial Loads)*	±100lbf (_444:8N)	±0.25% of Full Scale
USB-6009 *(Data Acquisition)*	±1.0V	±0.5mV RMS, 14-bit resolution
W-C03 0 *(Fuel Mass)*	0-3kgf (0-6:6lbf)	±0.0005 kgf (±0.0011lbf)
PX142-015A5V *(Nozzle Exit Static Pressure)*	0-15 psi absolute (103.5 kPa)	±0.15% of Full Scale
PX142-030A5V (*Nozzle Exit Stagnation Pressure*)	0-30 psi absolute (207.0 kPa)	±0.15% of Full Scale

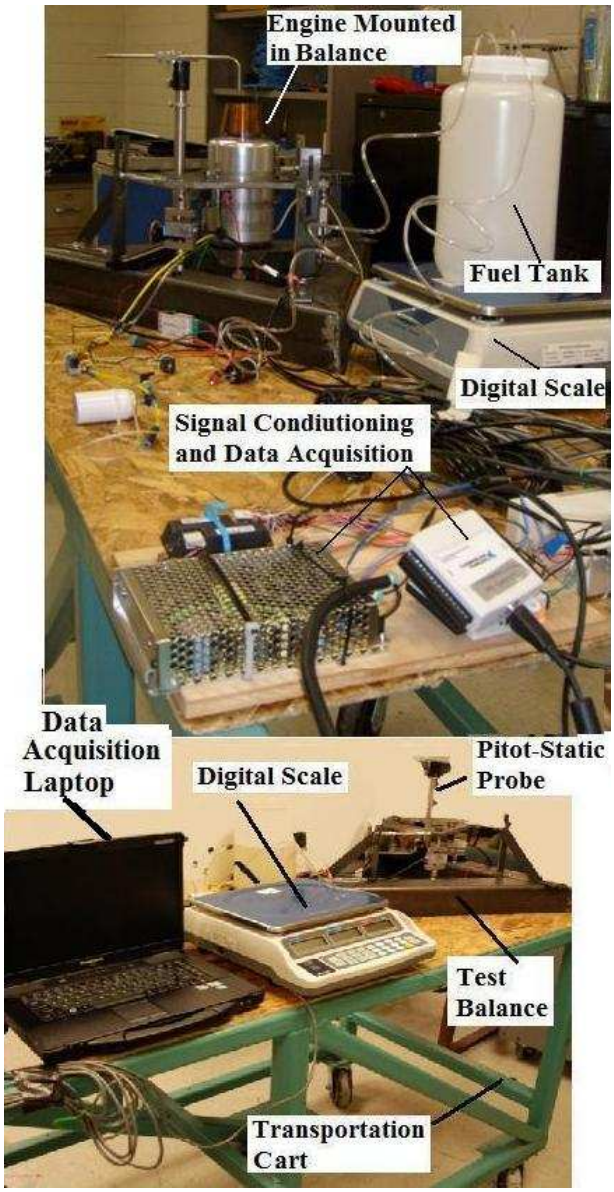

Figure 45. Test Support Cart for Jet Engine Thrust Stand.

32. Traversing Pitot Probe Description

The traversing probe was designed to sweep across the engine plume centerline and provided two-dimensional stagnation pressure, velocity, and mass flow distribution data very near the nozzle exit plane. A single axis position controller, mounted on a rack and pinion tracking system was used as the drive mechanism. Figure 46 shows this drive mechanism.

A 5-Watt motor is mounted on top of the traversing block. The motor gears mesh with two large external gears that carry the motor torque down into a shaft inside of the block. The shaft has teeth against the track. As the shaft rotates the mount moves. Linear position along the track is sensed by a ThinPot® linear potentiometer.[28]

This sensor is constructed from a polyester substrate mounted with pressure sensitive adhesive. As a contact wiper applies pressure as it moves with the mount, the linear potentiometer changes resistance. A commercial H-bridge circuit[29] is used to control the direction and traverse speed of the probe. Detailed design features regarding this traversing probe can be found in Ref. 7, Appendix F.

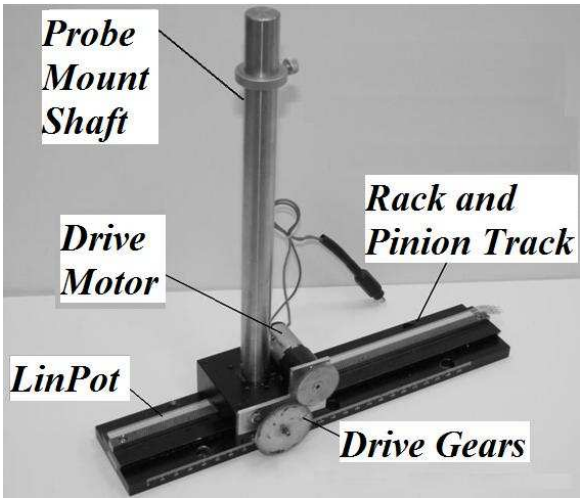

Figure 46. Pitot-Probe Drive Mechanism.

33. Jet Engine Thrust Stand Coordinate System Definition

As mentioned earlier, the thrust stand is designed so the engine exhaust plume exits vertically, and the thrust acts downward into the test cart. The load cells are divided into axial [*Aa, Ba,* and *Ca*] and lateral [*Al, Bl,* and *Cl*] groups based on the orientation of their sensing axes. The coordinate system for the thrust stand, pictured in Figure 44, is defined with *z-axis* acting vertically upward along the axial centerline of the engine. The thrust stand axis system is defined to be consistent with the coordinate system pictured in Figure 44. The thrust thus, acts in the negative z-direction. The *y-axis* runs perpendicular to and intersects the longitudinal axis of the axial load cell, *Aa*. The *x-axis* completes the system.

A rotational moment about the y-axis is equivalent to a positive pitching moment on the vehicle; a moment about the z-axis is equivalent to a positive yawing moment on the vehicle; and a moment about the *x-axis* is equivalent to a positive rolling moment on the vehicle. The origin of the coordinate system is centered in the plane of the engine mounts, and lies along the sensing axes of the lateral load cells.

34. Jet Engine Thrust Stand Calibration Procedure

Because of the geometric complexity of the test stand, the entire test stand was calibrated for output forces and moments as a function of the 6 load cell readings. For this calibration process, the test stand is mathematically modeled as a linear perturbation model of the form

$$\begin{bmatrix} F_x \\ F_y \\ F_z \\ M_x \\ M_y \\ M_z \end{bmatrix} = \begin{bmatrix} \frac{\partial F_x}{\partial V_{Aa}} & \frac{\partial F_x}{\partial V_{Ba}} & \frac{\partial F_x}{\partial V_{Ca}} & \frac{\partial F_x}{\partial V_{Al}} & \frac{\partial F_x}{\partial V_{Bl}} & \frac{\partial F_x}{\partial V_{Cl}} \\ \frac{\partial F_y}{\partial V_{Aa}} & \frac{\partial F_y}{\partial V_{Ba}} & \frac{\partial F_y}{\partial V_{Ca}} & \frac{\partial F_y}{\partial V_{Al}} & \frac{\partial F_y}{\partial V_{Bl}} & \frac{\partial F_y}{\partial V_{Cl}} \\ \frac{\partial F_z}{\partial V_{Aa}} & \frac{\partial F_z}{\partial V_{Ba}} & \frac{\partial F_z}{\partial V_{Ca}} & \frac{\partial F_z}{\partial V_{Al}} & \frac{\partial F_z}{\partial V_{Bl}} & \frac{\partial F_z}{\partial V_{Cl}} \\ \frac{\partial M_x}{\partial V_{Aa}} & \frac{\partial M_x}{\partial V_{Ba}} & \frac{\partial M_x}{\partial V_{Ca}} & \frac{\partial M_x}{\partial V_{Al}} & \frac{\partial M_x}{\partial V_{Bl}} & \frac{\partial M_x}{\partial V_{Cl}} \\ \frac{\partial M_y}{\partial V_{Aa}} & \frac{\partial M_y}{\partial V_{Ba}} & \frac{\partial M_y}{\partial V_{Ca}} & \frac{\partial M_y}{\partial V_{Al}} & \frac{\partial M_y}{\partial V_{Bl}} & \frac{\partial M_y}{\partial V_{Cl}} \\ \frac{\partial M_z}{\partial V_{Aa}} & \frac{\partial M_z}{\partial V_{Ba}} & \frac{\partial M_z}{\partial V_{Ca}} & \frac{\partial M_z}{\partial V_{Al}} & \frac{\partial M_z}{\partial V_{Bl}} & \frac{\partial M_z}{\partial V_{Cl}} \end{bmatrix} \begin{bmatrix} V_{Aa} \\ V_{Ba} \\ V_{Ca} \\ V_{Al} \\ V_{Bl} \\ V_{Cl} \end{bmatrix} \tag{7}$$

In Eq. (7) the vector $[F_x, F_y, F_z, M_x, M_y, M_z]$ has as components the desired forces and moments to be calculated when the force thrust stand is loaded. The vector $[V_{Aa}, V_{Ba}, V_{Ca}, V_{al}, V_{Bl}, V_{Cl}]$ has as components the output voltages from the six axial and lateral load cells. The linear system of Eq. (7) assumes that the voltage readings for the 6 load sensors have been adjusted so that zero-load on the thrust stand produces zero load cell output. The 36 elements of the Jacobian matrix define the externally applied forces and moments in terms of the sensed (and zeroed) load cell outputs. The calibration procedure reverses the process with multiple known external forces and moments applied to the thrust stand, and the corresponding sensor reading are logged. Assuming a set of N calibration inputs,

$$\tilde{F} = \left\{ \begin{bmatrix} F_x \\ F_y \\ F_z \\ M_x \\ M_y \\ M_z \end{bmatrix}_1 \begin{bmatrix} F_x \\ F_y \\ F_z \\ M_x \\ M_y \\ M_z \end{bmatrix}_2 \cdots \begin{bmatrix} F_x \\ F_y \\ F_z \\ M_x \\ M_y \\ M_z \end{bmatrix}_N \right\}, \tag{8}$$

and a corresponding set of sensor outputs

$$\tilde{V} = \left\{ \begin{bmatrix} V_{Aa} \\ V_{Ba} \\ V_{Ca} \\ V_{Al} \\ V_{Bl} \\ V_{Cl} \end{bmatrix}_1 \begin{bmatrix} V_{Aa} \\ V_{Ba} \\ V_{Ca} \\ V_{Al} \\ V_{Bl} \\ V_{Cl} \end{bmatrix}_2 \cdots \begin{bmatrix} V_{Aa} \\ V_{Ba} \\ V_{Ca} \\ V_{Al} \\ V_{Bl} \\ V_{Cl} \end{bmatrix}_N \right\}, \tag{9}$$

Eq. (7) can be written as the *6 x N* dimensioned matrix equation

$$\tilde{F} = J\ \tilde{V}. \tag{10}$$

In Eq. (10) J is the Jacobian matrix from Eq. (7). Post-multiplying both sides of Eq. (10) by $\tilde{V}^T$ produces the *6 x 6* dimensioned system

$$\tilde{F}\ \tilde{V}^T = J\left(\tilde{V}\ \tilde{V}^T\right). \tag{11}$$

Post multiplying both sides by $\left(\tilde{V}\ \tilde{V}^T\right)^{-1}$ gives the least squares estimate for the Jacobian matrix

$$\hat{J} = \tilde{F}\ \tilde{V}^T\left(\tilde{V}\ \tilde{V}^T\right)^{-1}. \tag{12}$$

Now given an arbitrary set of load cell readings (zeroed for the no load case), the force and moment outputs from the thrust stand can be calculated as

$$\begin{bmatrix} F_x \\ F_y \\ F_z \\ M_x \\ M_y \\ M_z \end{bmatrix} = \hat{J} \begin{bmatrix} V_{Aa} \\ V_{Ba} \\ V_{Ca} \\ V_{Al} \\ V_{Bl} \\ V_{Cl} \end{bmatrix}. \tag{13}$$

Calibration loads and moments are applied to the test stand using known calibration weights. Three axial and three lateral loads are applied at any one time, and the resulting forces and moments calculated using the known input geometry. The axial calibration weights are placed over 1/2 in (12.7mm) diameter steel alignment rods which are approximately 0.46m (18 in) in length. These rods are threaded onto the same threaded rod that holds the corresponding axial load cell to the engine mounting plate. The masses of these rods are included as part of the calibration load. The lateral calibration loads are applied by weights suspended on a lines routed through the pulleys and attached to the engine mounting plate. Figure 47 shows the location of the weights and pulleys used to apply the calibration inputs to the test stand.

In a typical calibration procedure system zeroes are determined by reading the load cell voltages for 10 seconds with no loads applied and averaging the time history results. These zeroes are analytically removed from the load cell voltage readings. next alignment rods are threaded on to each of the axial calibration load points. Each rod has a mass of approximately *0.8 kg* (*1.7 lb*). Next *3.0 kg* (*6.6 lbm*) masses are placed on each of the rods. This arrangement creates a total axial force of approximately 110.8 N (24:9 lbf). A 0.45 kg (1.0 lbm) mass is subsequently placed on the axial rod above load cell "Aa". The six load cell voltages and reference loads are logged.

The 0.45 kg mass is sequentially moved to the axial rods above load cell "Ba," and then load cell "Ca.". Voltages and loads are logged in each case. Next, a 0.57kg (1:25 lbm) mass is applied to lateral calibration load point "A" through pulley "A". Data are logged and the process is repeated for process is for lateral calibration points "B" and "C." The applied weights are sequentially increased to generate the calibration data set.

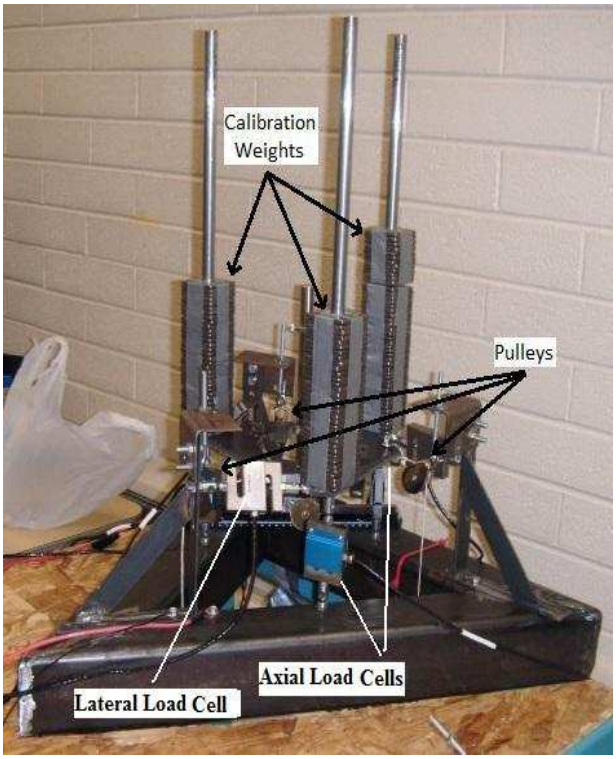

Figure 47. Apparatus used to Apply Calibration Inputs to Thrust Stand.

Table 18 shows a typical calibration matrix generated using this procedure. The rows of this matrix represent the sensitivity of the output loads and moments to the individual load cell milivolt readings, with rows 1-3 corresponding to F_x, F_y, and F_z, and rows 4-6 corresponding to M_x, M_y, and M_z. Notice that the matrix is not particularly sparse, indicating that all of the sensed loads on the load cells contribute to the over-all load and moment calculations.

Table 18. Typical Jet Engine Test Stand Calibration Matrix.

-14806.0236	-15058.9246	-15526.6969	-411.71890	-890.7967	-837.6023
38.5345	-890.1487	935.5346	-404.1727	-3137.2754	3390.6717
-663.4781	440.6172	327.8234	-3815.9789	2124.6036	1865.7721
-74.41130	-134.8726	-150.7640	-470.5827	-531.5757	-539.3858
-27.1716	1899.0908	-1778.5431	-22.6189	-3.9264	-23.6677
2063.5040	-1005.05431	-1046.5082	14.7288	25.2133	20.8681

Table 19 shows the normalized sensitivity of each load or moment to the individual load cell outputs. The values in this table were calculated for each row by taking the maximum absolute value of the six elements in the row, and dividing this value back into the element of the row. The magnitudes show the relative contribution of the load cell output to the force or moment calculation. For example, the major contributors to the yawing moment calculation, M_x (row (3), are the lateral load cell outputs (columns 4-6). Conversely, the pitching moment calculation M_y, is most sensitive to the output from the axial load cells "B" and 'C," and is almost completely insensitive to the outputs from the lateral load cells. As expected, the thrust ($-F_x$) is most sensitive to the outputs from the axial load cells, and almost completely insensitive to the lateral load cell outputs.

Table 19. Typical Jet Engine Test Stand Calibration, Normalized Sensitivity.

	Load Cell Aa	*Load Cell Ba*	*Load Cell Ca*	*Load Cell Al*	*Load Cell Bl*	*Load Cell Cl*
F_x	0.954	0.970	1.000	0.027	0.057	0.054
F_y	0.011	0.263	0.276	0.119	0.925	1.000
F_z	0.174	0.115	0.086	1.000	0.557	0.489
M_x	0.138	0.250	0.280	0.872	0.986	1.000
M_y,	0.014	1.000	0.937	0.012	0.002	0.012
M_z	1.000	0.487	0.507	0.007	0.012	0.010

35. Calibration Uncertainty Estimates

A total of 32 independent calibration data sets were generated. Collectively these data were used to calculate the inverse Jacobian (calibration) matrix for the system. Four of these load cases imparted identical forces and moments to the test stand and were used to estimate the statistical uncertainty of the calibration. Table 19 shows the statistical results from the 4 identical load cases. These data are used to estimate the accuracy of the test stand measurements.

Table 20. Statistical Evaluation of 4 Identical Load Calibration Cases.

	F_x (N)	***F_y (N)***	***F_z (N)***	***M_x (N-m)***	***M_y (N-m)***	***M_z (N-m)***
Applied Load	-10.5564	9.2343	-146.2732	1.5795	1.3984	-0.7730
Case 1	-10.4109	8.7975	-144.8075	1.5504	1.3641	-0.7144
Case 2	-10.0210	8.8739	-145.2573	1.5906	1.4094	-0.7168
Case 3	-10.2296	9.1023	-147.0431	1.7030	1.4112	-0.7285
Case 4	-10.0759	9.0838	-144.6441	1.7964	1.3039	-0.7290
Mean	-10.1844	8.9644	-145.4380	1.6601	1.3722	-0.7222
Standard Deviation	0.1749	0.1520	1.1010	0.1115	0.0504	0.0077
Error	0.3721	-0.2700	0.8352	0.0806	-0.0263	0.0108
Error (%)	3.65%	3.01%	0.57%	4.86%	1.91%	1.50%

When these sample statistics are used to approximate then 95% confidence interval on the mean error estimate using the confidence interval formula,[30]

$$S_{\bar{x}} = \frac{t_{95} \cdot \hat{\sigma}_x}{\sqrt{N}} \quad . \tag{14}$$

In Eq. (14) $S_{\bar{x}}$ is the mean error confidence level, $\hat{\sigma}_x$ is the sample standard deviation, and t_{95} is the t-distribution variable corresponding to a 0.95 double-ended probability corresponding and N-1 degrees of freedom. For the case of Table 21, t_{95}*=3.19 and N=4.* These intervals are shown in column 2of Table 21. The mean error is a systematic error and is subtracted from the results of calculations from Eq. (13). The confidence interval is the random uncertainty in the test-stand measurements.

Table 21. Test Stand Mean Measurement Error Uncertainty Estimates.

Measurement	Mean Error ± Confidence Interval	Total Measurement Uncertainty Estimate
F_x **(N)**	0.372 ± 0.278	±0.279 N (±2.64%)
F_y **(N)**	-0.270 ± 0.242	±0.242 N (±2.62%)
F_z **(N)**	0.835 ± 1.752	±1.752 N (±1.2%)
M_x **(N-m)**	0.081 ± 0.177	±0.177 N-m (±11.23 %)
M_y **(N-m)**	-0.263 ± 0.080	±0.082 N-m (±5.83 %)
M_z **(N-m)**	0.108 ± 0.012	±0.020 N-m (±2.59%)

The calibration weights were initially measured using the Weighmax W-C03 scale described in the previous section. The estimated scale error, based on manufacturer, is +0.005 kgf. The uncertainty in the moment arms points on the lateral load cells is estimated at 1/16th inch (±1.6 mm). Factoring in the uncertainty in the scale measurements and moment arm measurements as systematic errors; and root sum-squaring these errors with the random uncertainties from column 2 of Table 20, the total estimated test stand measurement uncertainty are calculated. These total measurement uncertainty estimates are listed in column 3 of Table 21

36. Total Static Thrust Measurements

Six different static thrust tests were performed to characterize the JF-170 Rhino Performance. Thrust data were plotted against engine RPM measured by the FADEC and curve fitting the data produce static thrust curves. With the thrust vectoring system installed, the engine produces approximately 30 lbf of thrust at full throttle (120,000 RPM). Figure 48 compares the original manufacturer's thrust/PRM profile (Ref. 13) against the measured thrust RPM profile with the vectoring system installed. The thrust vectoring installation reduces the available thrust by approximately 17-18%. The RPM (x-axis) is plotted in units of 1000's of RPM. The thrust vectoring system test results are described in detail in the next section. The fuel consumption rate of the JF-170 Rhino is very much dependent on the operating RPM of the engine.

Figure 49 shows the measured fuel mass flow consumption as a function of the engine throttle setting. Fuel consumption was derived by numerically differentiating the fuel mass time history profiles, plotting as a function of throttle, and curve-fitting the results. The vehicle design assumes a nominal flight thrusting level of 85% throttle for the gravity offset system.[§] When operating at an 85% throttle setting (115,000 RPM) produces approximately 26 lbf thrust. At this throttle setting the mass-flow rate is approximately 0.36 kg/min. At a sustained 85% throttle, one kg of fuel can produce approximately 3- minutes of flight time.

[§] The 85% throttle setting corresponds to operating at "Mil-power" in a military-style high performance fighter aircraft.

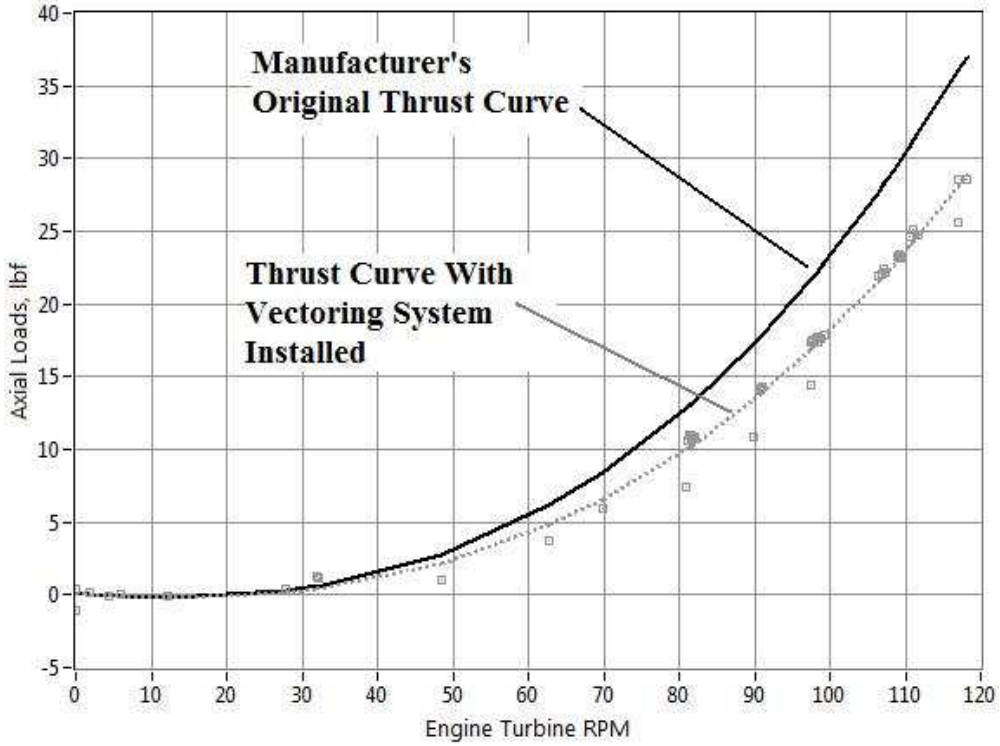

Figure 48. JF-170 Rhino Thrust/RPM Curve.

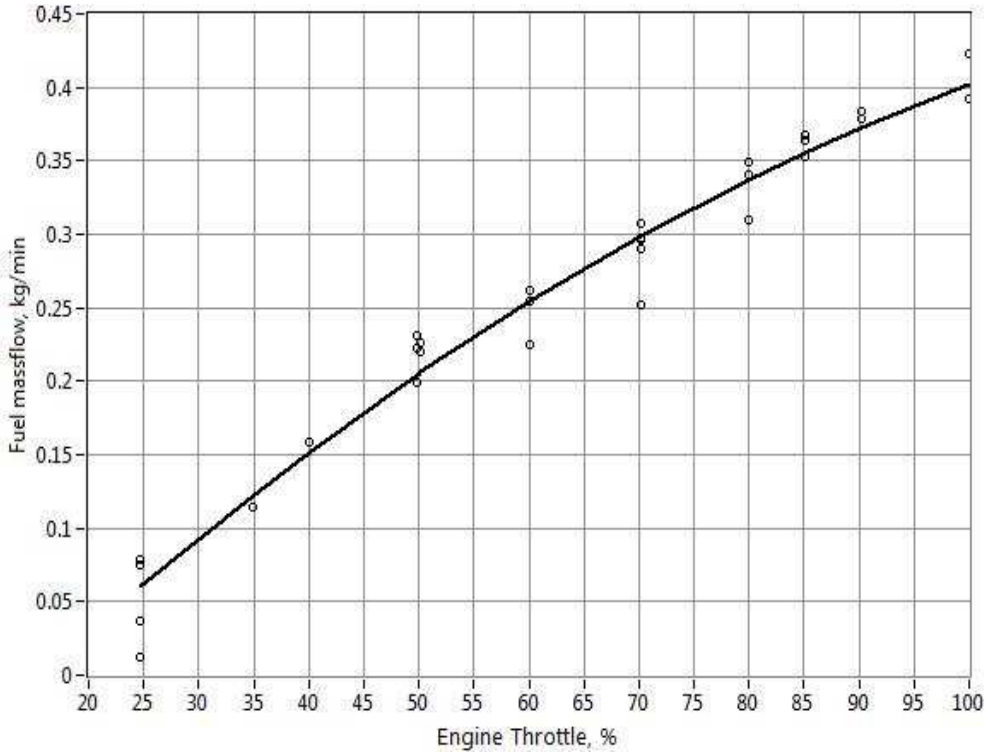

Figure 49. Measured Fuel Mass Flow Consumptions as Function of Throttle Setting.

37. Nozzle Exit Plane Profile

The JF-170 Rhino has an unusual exit plane velocity and Mach number distribution profile. This profile has a large momentum defect near the axial centerline. The source of this momentum defect is unclear, but it is possible that the "hole" is a result of flow separation off of the turbine's conical exit fairing. The exit fairing is short and blunt at the end, and even at 100% throttle setting the nozzle exit velocity is subsonic. In subsonic flow these types of aft-facing geometry features frequently lead to flow separation. Figure 50 pictures the nozzle and turbine exit fairing.

Figure 51 plots the exit plane Mach number distribution, calculated using the pitot-static pressure measurements. the data are plottted as a function of the radial distance from the axial centerline for 25%, 50%, 75%, 80% and 100% throttle settings. (Ref. 11) The span of the high-velocity flow is approximately 30 mm wide on either side of the momentum hole. The hole is approximately 12 mm wide. These exhaust plume features significantly affected the thrust vectoring vane design. To best take advantage of this flow distribution and to aid in manufacturability, the pitch and roll axis turning vanes were each divided into two sections each, with each section spanning approximately 33 mm with a 12 cm gap between sections. Due to the momentum hole in the center of the nozzle, the "gap" between airfoil sections eliminates pitch-vane and roll-vane interference, while having a minimal effect on the overall performance. The vanes are slightly oversized to extend beyond the edge of the exit jet-plume. This extension beyond the plume flow field helps to weaken the tip-vortex of wing and minimizes induced drag effects.

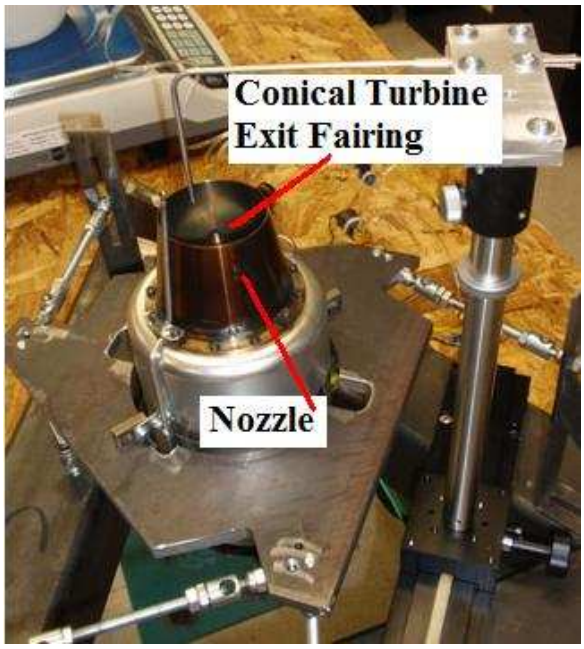

Figure 50. JF-170 Rhino Nozzle and Turbine Exit Fairing.

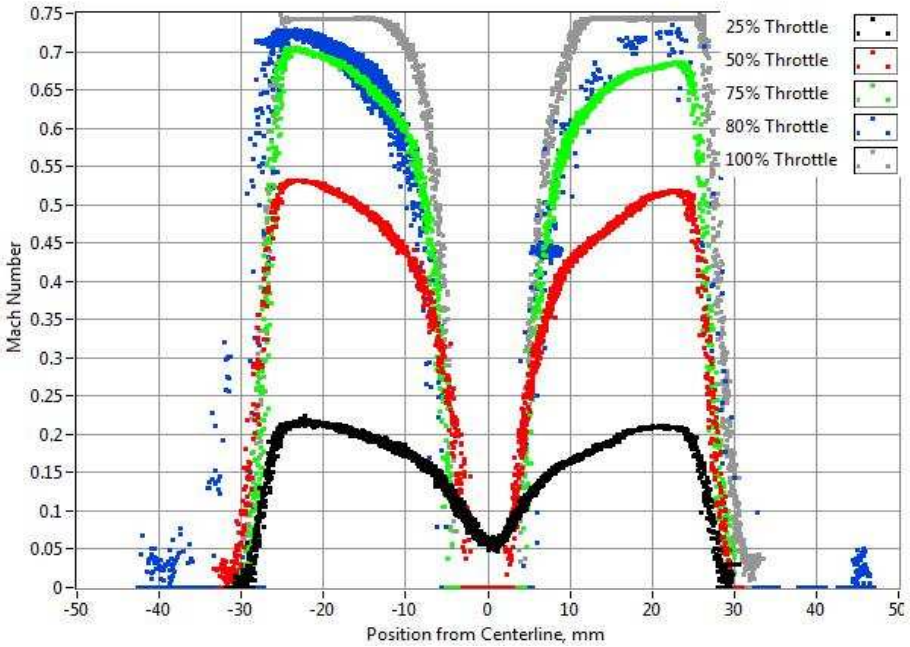

Figure 51. JF-170 Rhino Exit Plane Mach-Number Distribution for Various Throttle Settings.

38. Thrust Vectoring Side Force and Moment Measurements

A series of static tests were performed to verify the effectiveness of the thrust vectoring vanes. Results from these tests were also used to update the data presented in Figure 20. Figure 52 shows the load cell outputs for a typical test, adjusted for their initial zero offsets. In this test the throttle setting was increased from idle to 100%. At each throttle setting the pitch vane was swept through a deflection range from -9° through 9°. Figure 52a plots the load cell outputs. Figure 52b plots the vane deflections. The engine throttle settings are also indicated on the load graph. The vane deflections are clearly visible on all 6 load cell readings. A negative reading indicates the load cell is under compression, a positive reading indicates a tensile load on the sensor.

The level of the lateral load cell outputs drifts away from center as the throttle is increased. During each airfoil sweep, the airfoil paused at zero defection for a short time. These pauses can be seen in Figure 52a, and help to illustrate the manner in which the lateral voltages tend to drift as the axial forces increases. This drift is a test stand artifact, and is likely caused by deflections in the load cells and the test stand structure itself. To correct for this effect, each lateral load cell voltage was reduced by an amount directly proportional to the corresponding axial load cell voltage,

$$V_{\{I\}l_{adj}} = V_{\{I\}l} + k_{\{I\}} \cdot V_{\{I\}a} \qquad (15)$$

In Eq. (15) the index {I} corresponds to the load cell indices {A, B, C}, the subscript *l* implied a lateral load cell reading, and the subscript *a* implies an axial load cell reading. These coefficients were selected to minimize the drift of the mean lateral load signal away from the zero trim-line. Figure 53 compares the original (a) and adjusted (b) lateral load cell readings. The drift is dramatically reduced.

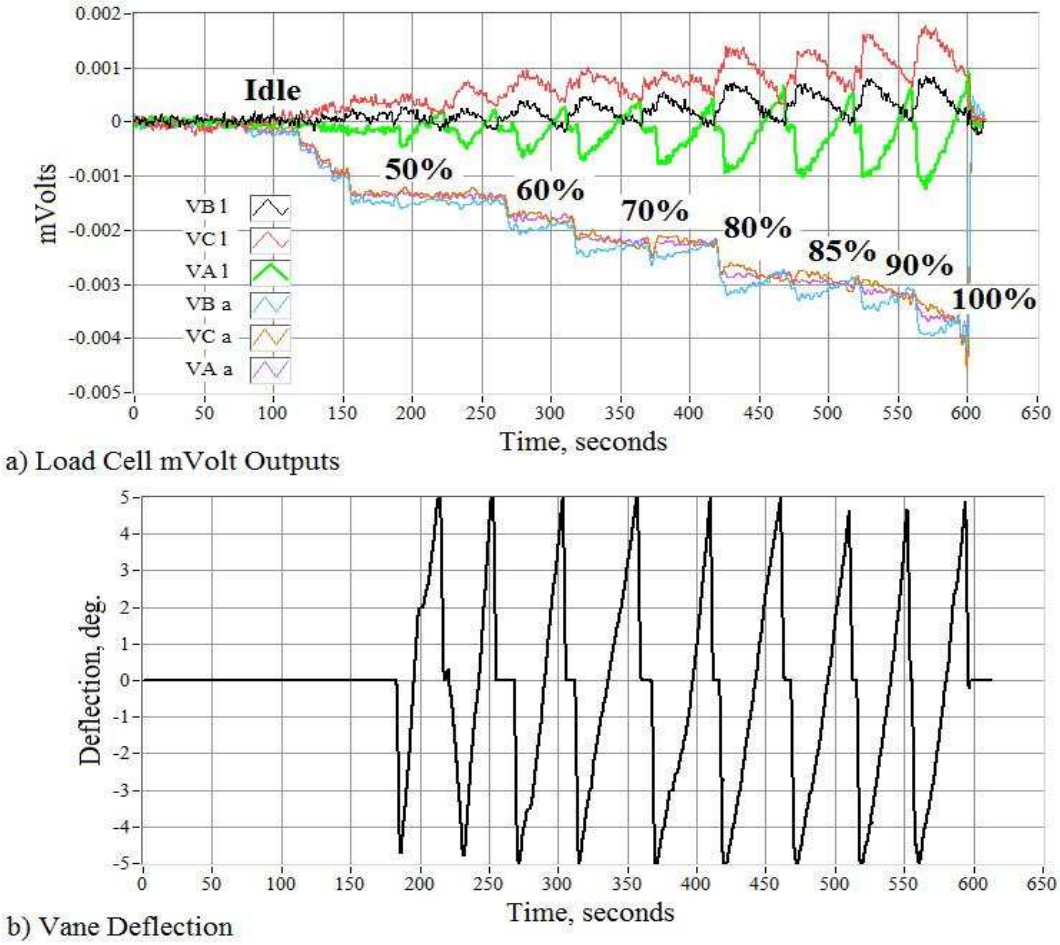

Figure 52. Load Cell mVolt Output for a Typical Thrust Vectoring Test Case.

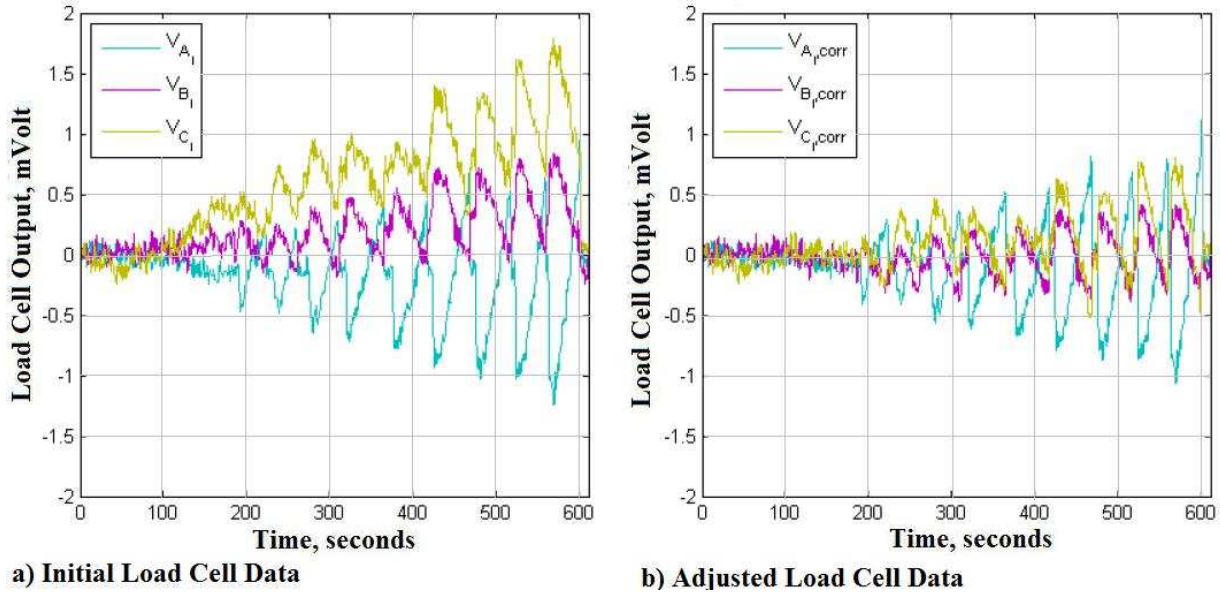

Figure 53. Comparison of Original and Adjusted Load Cell Readings

Figure 54 shows the vane forces calculated using the adjusted lateral load cell data. These calculations use the inverse Jacobian matrix calculated with all 32 calibrations load cases data, and also apply the test stand bias corrections from Table 21. There is very little van cross-talk remaining and, as expected the pitch van imparts a side force only along the direction of the x axis.

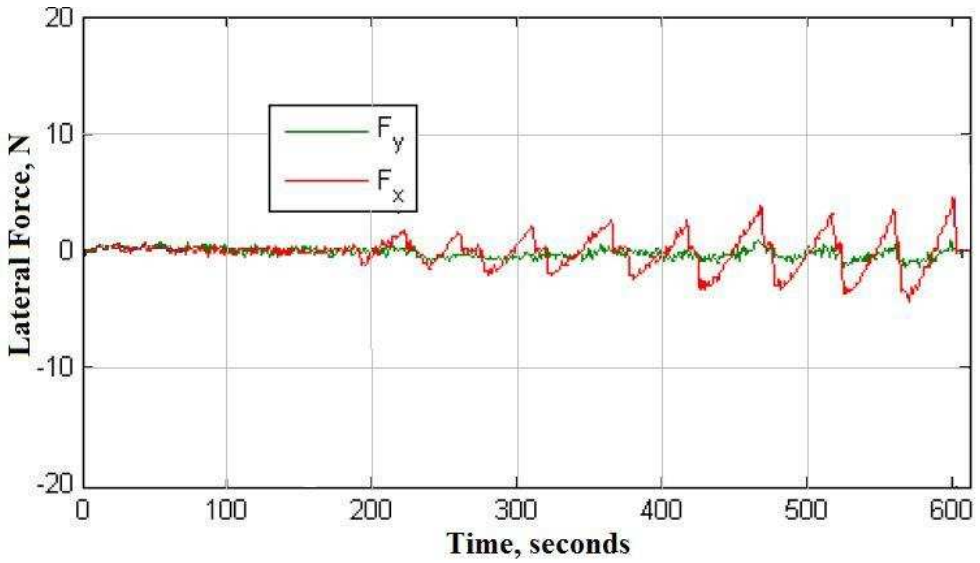

Figure 54. Lateral Vane Forces Calculated Using Adjusted Lateral Load Cell Data.

Figure 55 plots the forces and moment for all three axes using the adjusted load cell data. The F_z force data corresponds to a positive thrust level. Cross talk between the axes has been virtually eliminated; however, there is a slight pitching moment asymmetry, and is likely due to the exit plane wake asymmetry. The exit wake asymmetry can be clearly observed in Figure 18. The lower exit plane Mach number on the right hand side of the wake has the effect of reducing the vane effectiveness in that direction. The moment data of Figure 55 were curve fit to generate the look up table data presented in Figure 20. Similar data were generated for the vehicle roll axis.

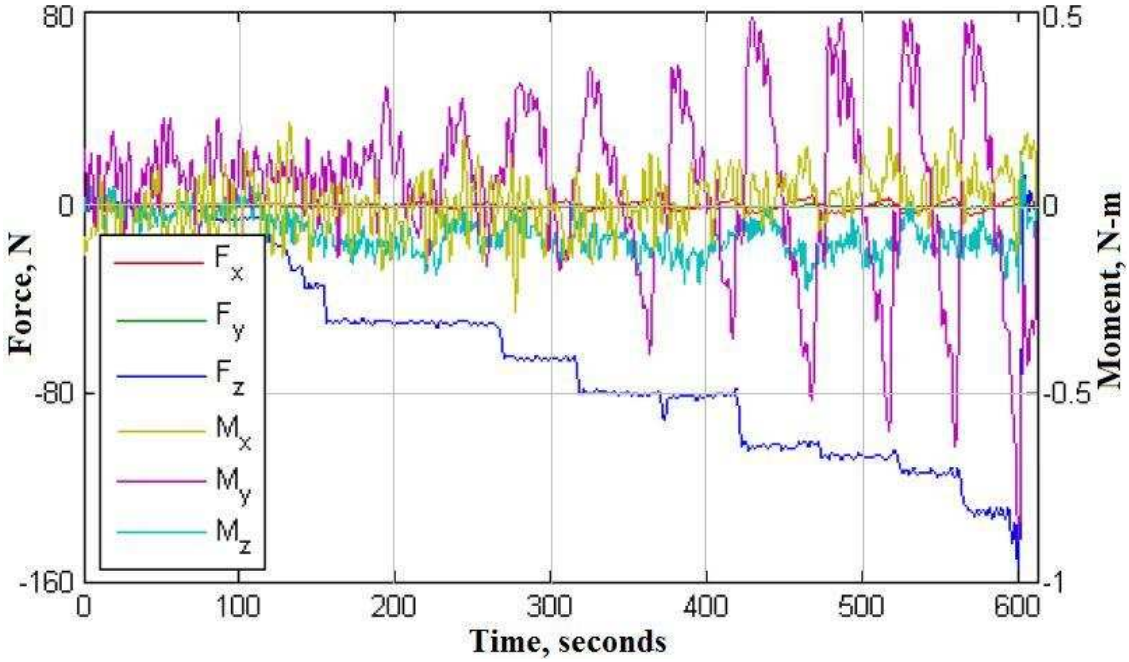

Figure 55. Calculated Forces and Moments Using Adjusted Load Cell Data.

DD. Jet Engine Vectoring, Free-Gimbal Ground Tests.

A series combined system tests (CTS) to evaluate the performance of the thrust vectoring controls were performed prior to the first hover flight test. The objectives of these free-gimbal tests were to verify the system stability, and also demonstrate that the thrust vectoring system can effectively control the pitch and roll angles of the inner platform. Figure 56 shows the test arrangement. Here the fully integrated vehicle was placed in the test cell on a steel grate that suspends the nozzle exit plane approximately 1 meter above the test cell floor.

The LPSLRV strut wheels were removed and the legs were safety wired to the grate to keep the vehicle from lifting off. The grate was supported on a frame and weighted down to prevent the vehicle from lifting the strand off of the ground. Depending on the test objective, the pitch and roll gimbals could be locked in place, or free to rotate. Tests with one gimbal locked and with both gimbals free to rotate were performed. The annular gas tank attached to the inner platform was fully fueled at the start of each test. The full fuel tank holds approximately *1.66 kg* of kerosene.

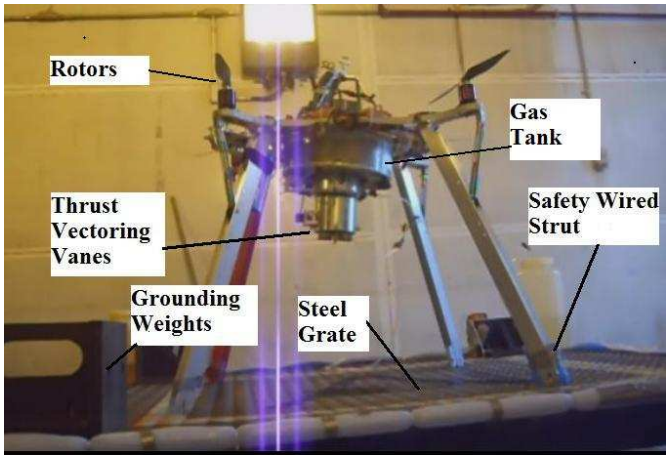

Figure 56. Test Setup for Ground Thrust Vectoring Gimbal Tests.

39. Inner Platform Natural frequency, Damping Ratio, and Moment of Inertia Measurements

Before the CST was performed it was essential to understand the rotational inertias, natural frequencies, and damping ratios for both the pitch and roll axes of the inner platform. Here a series of inertia swings were performed to estimate these parameters. The process follows the method outlined by Wolowicz and Yancey.[31] Here the platform dynamics for each axis was modeled as a simple linear pendulum. This second-order model is valid for small angle

approximations; and for the pitch axis can be written as

$$\ddot{\theta} + \frac{B}{I_{yy}} \cdot \dot{\theta} + \frac{K}{I_{yy}} \cdot \theta = \frac{M_y}{I_{yy}} \qquad (16)$$

An identical expression can be written for the roll axis. In Eq. (16) the parameter B is the rate damping term and K is the torsional spring constant. For the inertial swing tests, the platform was perturbed to a non-zero position and allowed to swing freely ($M_y = 0$) and the acceleration time histories along each axis were recorded by the inner-platform mounted IMU. The test setup utilizes the free-gimbal configuration depicted by Figure 56. Tests were performed with the fuel tank empty, partially full, and entirely full. Interestingly the response time histories showed almost no dependence on the fill level of the fuel tank. If the linear pendulum model is valid, this result is expected. Figure 57 shows typical responses for both the pitch and roll axes.

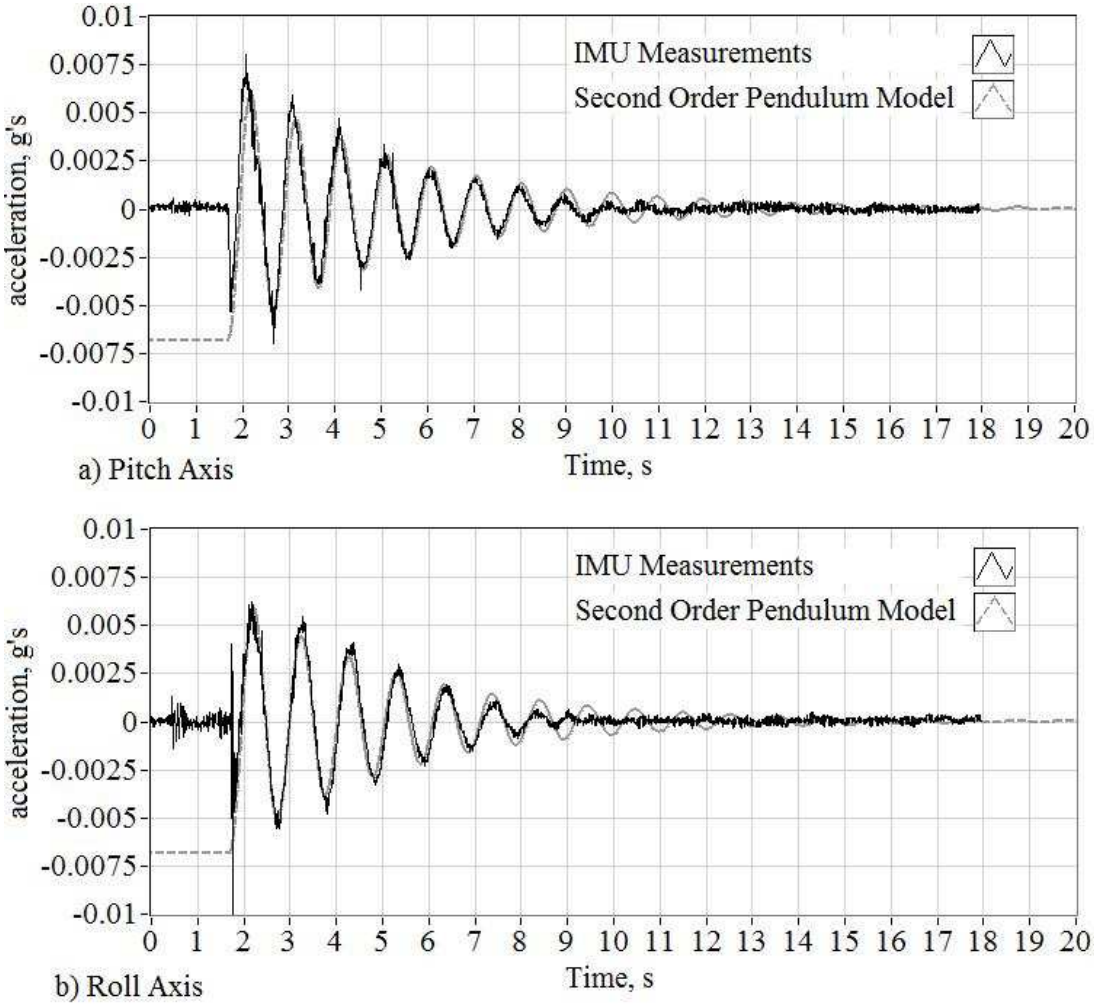

Figure 57. Unforced Response of Inner Platform Compared to Pendulum Model.

When written in terms of the natural frequency and damping ratio (Ref. 30, Chapt 3), the unforced response of the inner platform is

$$\ddot{\theta} + 2 \cdot \varsigma \cdot \omega_n \cdot \dot{\theta} + \omega_{n^2} \cdot \theta = 0\,, \qquad (17)$$

where the natural frequency and damping ratio are

$$\omega_n = \sqrt{\frac{K}{I_{yy}}}, \text{ and } \varsigma = \frac{B}{2 \cdot \sqrt{K \cdot I_{yy}}} \qquad (18)$$

The pendulum-model responses plotted in Figure 57 use the best-fit estimates of natural frequency and

damping ratio. Table 22 lists these parameters. The data presented in Figure 58 verify the best fit calculations for natural frequency. Here the power spectrum magnitude of the response time histories is plotted against cyclic frequency. For both axes there are distinct response peaks near 1.0 Hz. The secondary peak near 2 Hz on the pitch axis-plot is very likely due to fuel slosh in the tank. Clearly the system is very lightly damped, and any non-steady input has the potential to grow. Also, the natural response frequency, near *1 Hz* for both axes, must not be excited by the thrust vectoring, control algorithm. These considerations are of paramount importance when selecting the control law parameter values.

Table 22. Best-Fit Linear Pendulum Model Parameters for Inner Platform.

	ζ	ω_n *(rad/s)*	f_n *(Hz)*
Pitch Axis	0.04	6.44	1.025
Roll Axis	0.045	6.09	0.97

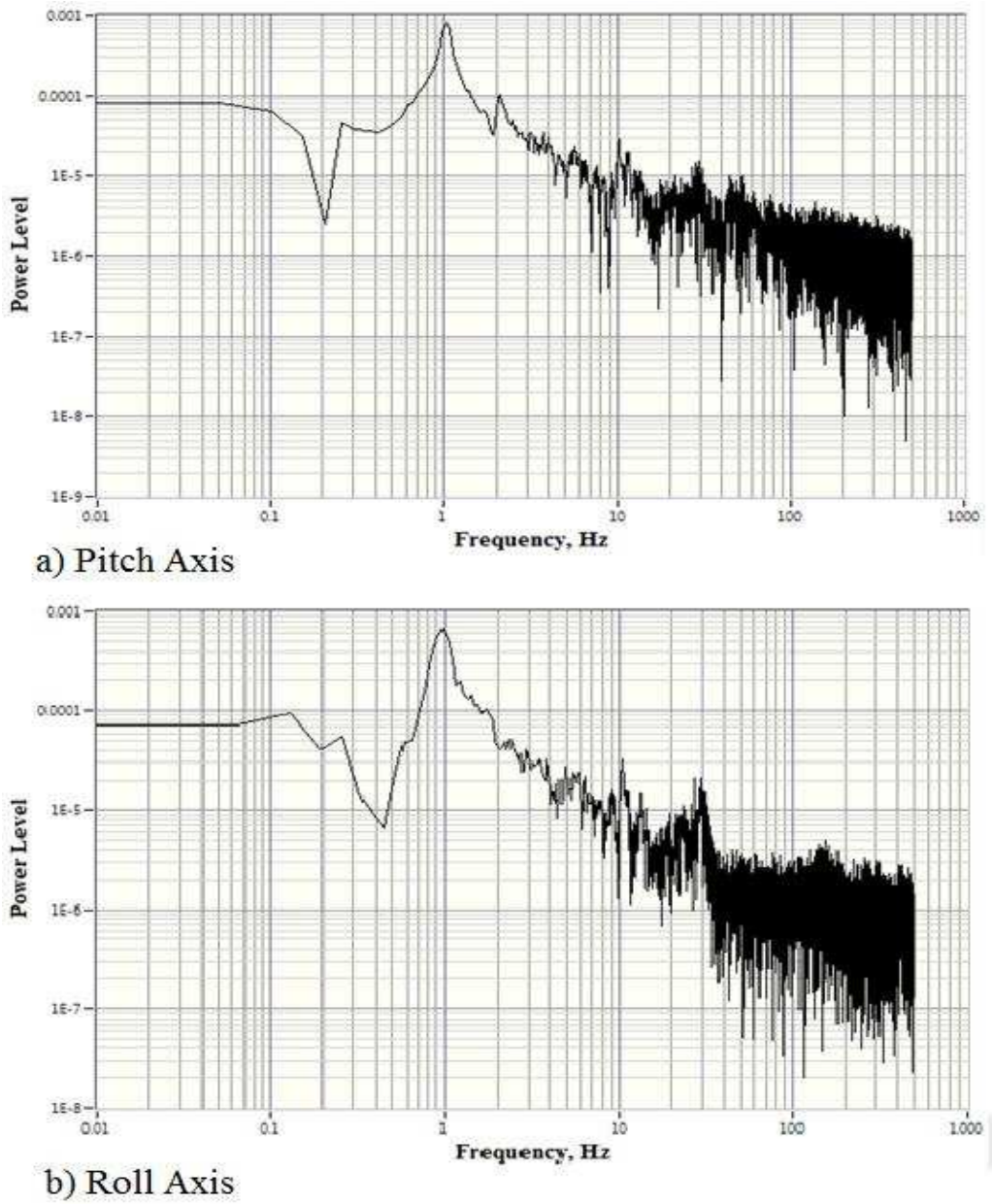

Figure 58. Inner Platform Unforced Response Spectrum Magnitude.

Assuming that the "spring force" that returns the inner platform to its vertical orientation is entirely due to the offset of the vertical of gravity from the gimbal pivot Z_{cg}; the torsional spring constant can be estimated as

$$K = \mathrm{m}_{inner} \cdot g \cdot Z_{cg} \tag{19}$$

Here m_{inner} is the mass attached to the inner platform and g is the acceleration of gravity. Using this expression, the principal rotational inertia of the inner platform about the pitch axis can be estimated by

$$I_{yy} = \frac{K}{\omega_n^{\,2}} = \frac{\mathrm{m}_{inner} \cdot g \cdot Z_{cg}}{\omega_n^{\,2}}. \tag{20}$$

A similar expression exists for the roll axis. Based on material and component weight estimates and the fuel mass, Table 23 shows the estimates of the moments of inertia and other accompanying parameters for full and empty fuel tanks. A linear interpolation based on the measured fuel consumption, 0.35 kg/min at 85% throttle (Figure 16), was used to schedule these values as a function of time. Figure 59 shows these inertia/burn time schedules. These inertia schedules were used in the control law formulations presented earlier in this paper.

Table 23. Inner Platform, Mass, Vertical Center of Gravity and Moment of Inertia Estimates.

Pitch Axis	***Dry Mass (kg)***	***Wet Mass (kg)***	***ω_n (rad/s)***	***Z_{cg} (cm)***	***Inertia (kg-m^2)***
Tank Empty	6.67	6.67	6.44	10.2	0.161
Tank Full	6.67	8.33	6.44	9.0	0.177
Roll Axis	***Dry Mass (kg)***	***Wet Mass (kg)***	***ω_n (rad/s)***	***Z_{cg} (cm)***	***Inertia (kg-m^2)***
Tank Empty	7.14	7.14	6.09	10.2	0.193
Tank Full	7.14	8.80	6.09	9.0	0.209

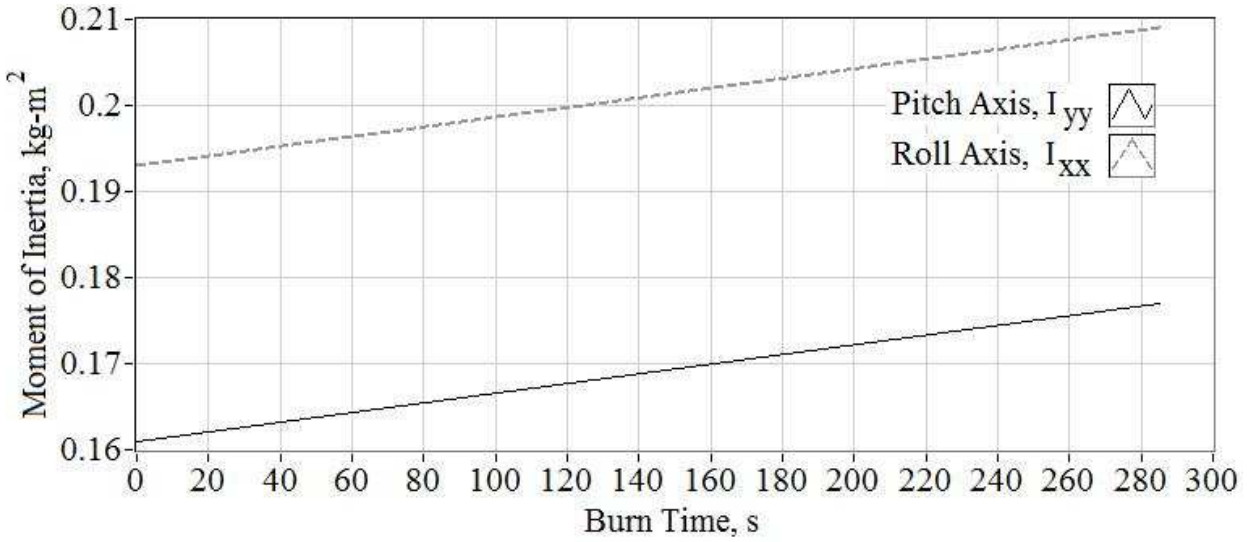

Figure 59. of Inertial Schedule for Control Law Implementations.

40. Free-Gimbal Test Results for Filtered, Proportional (Hover) Control Law.

At the writing of this paper, only the *Filtered, Proportional Hover Control Law* (Section V.18, pp 29) has successfully been implemented on the Gumstix hardware and verified as ready for testing. As mentioned previously, this interim control law was developed to expedite early flight testing in a near hover operational mode. Results of these free-gimbal tests are presented in this section. A thorough evaluation of the closed loop characteristics of the vehicle with this control law has yet to be performed.

The test procedure started with the vectoring control proportional gains set to zero for both pitch and roll axes. The initial damping ratio was set to 1.0 and the cyclic natural frequency was set to 0.1 Hz. The commanded reference control angles were set to zero. The engine was started, allowed to stabilize,

and ramped up to 35% throttle. The control gain was gradually increased until the vehicle began to demonstrate signs of oscillatory instability. The primary feature of this instability was a gyroscopic coupling between the pitch and roll axes. If not abated, this coupling would eventually cause the vehicle to become "rail-to-rail" unstable.

As the vehicle approached this incipient instability, the gain was halved and the pitch and yaw oscillations were allowed to damp. Once this "acceptable gain" was selected, then a similar approach was performed for the natural frequency of the filter. The filter frequencies were gradually increased until an incipient instability was one again encountered. At this point the frequency was halved, and the system was allowed to stabilize.

This process was performed repeatedly with the throttle gradually being increased to the desired 85% level. Once the 85% throttle level was reached, then the commanded pitch and roll angles were varied to place the engine in various orientations. This approach verified that the engine could be precisely pointed, and remain stable while maneuvering from one commanded angle set to another. The commanded angle limits varied from $\pm 10^o$. Figure 60 shows the engine being commanded to various pitch and roll angles. Each of the commanded orientations were held approximately 5 seconds before the next angle set was commanded.

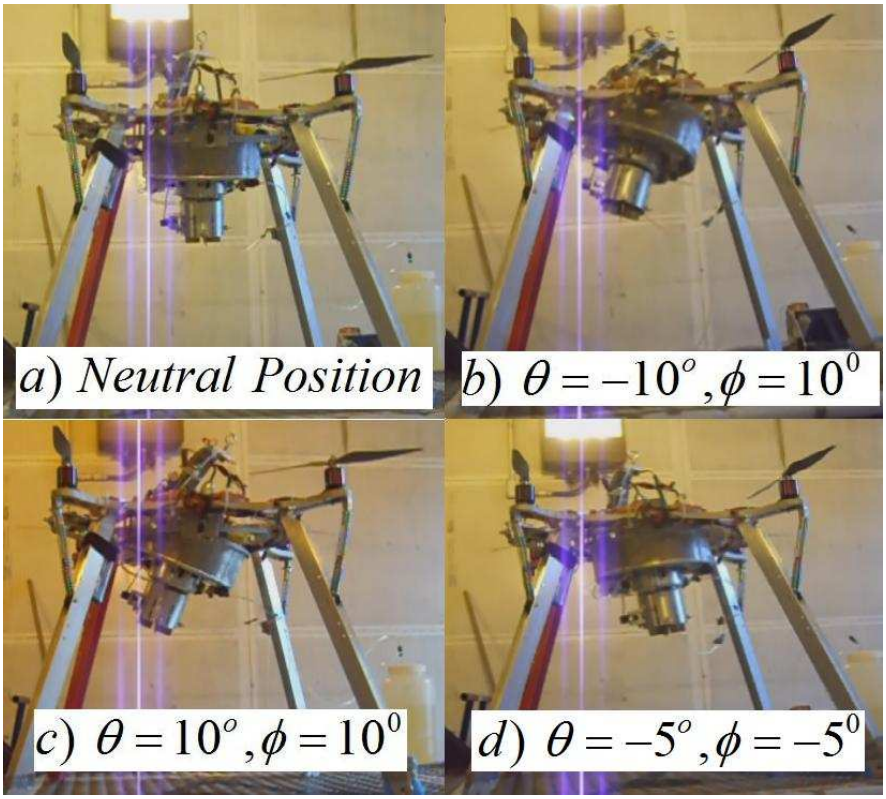

Figure 60. Vehicle Being Commanded to Each of 4 Pitch and Roll Quadrants at 85% Throttle.

For this test, Figure 61 plots the commanded angles versus the orientation angles sensed by the IMU. Graph (a) shows the pitch-axis response with the commanded attitude plotted on the abscissa, and the IMU-sensed response plotted on the ordinate. A second order curve fit to the data points and the +1-σ fit error bounds are also plotted. Graph (b) presents similar comparisons for the roll axis. The curves are reasonably linear, with standard deviations less than one-half degree. When this uncertainty about the zero-point (true vertical) is expressed in terms of uncontrolled jet-engine side thrust at 85% throttle; the values are quite small, 0.2 N for the pitch axis and 0.17 N for the roll axis. The outer platform maneuvering thrust can easily overcome these side forces. Details of the flight tests will be documented in a separate volume.

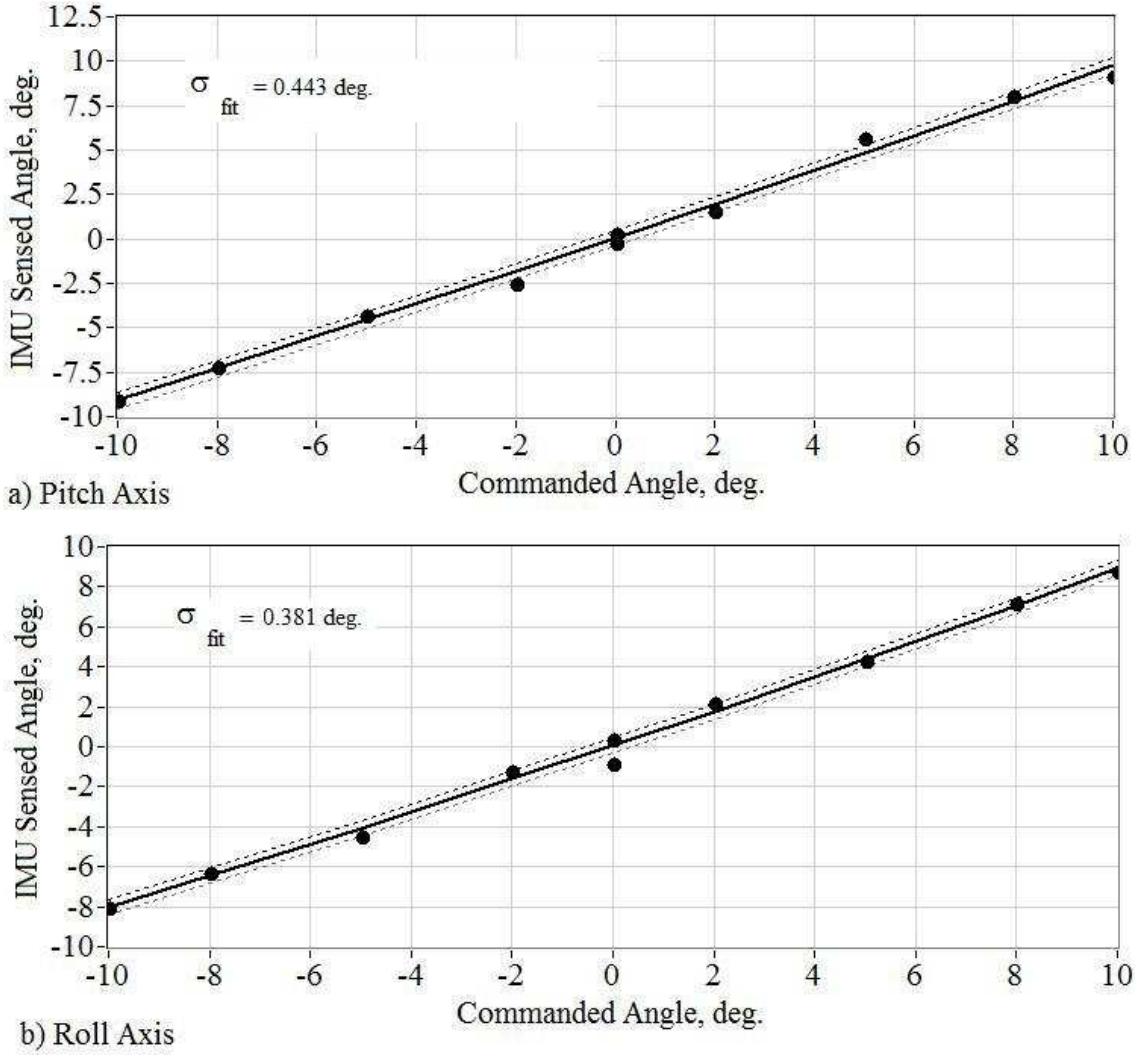

Figure 61. Commanded vs. IMU-Sensed Pitch and Roll Angles.

IX. Appendix B: Blade Element Code Development

Because of the small vehicle size, and the limited budget the team had to work with, all of the outer platform drive components were purchased from RC hobby stores. Unlike industrial or aerospace-based corporations, these hobby-based businesses do not rigorously keep performance data and specifications. Thus, much of the performance data for the vehicle components had to be generated by the project.

To support this data development and to meet academic objectives for the class, the student team developed a rotor/propeller performance code based on blade element and momentum theory.[32] The code was developed with sufficient generality to allow rotors of arbitrary size and pitch to be analyzed. Code outputs include thrust curves, braking power, and torque.

EE. Blade Element and Momentum Theory

The analysis of a propeller or rotor blade is similar to that of a finite wing. A rotors' thrust is nothing more than a rotating wing creating lift. Both the lift and drag on a rotor cross section are directly related to thrust and required torque on a spinning rotor. Figure 62 shows the velocity components and aerodynamic forces acting on a local airfoil section.

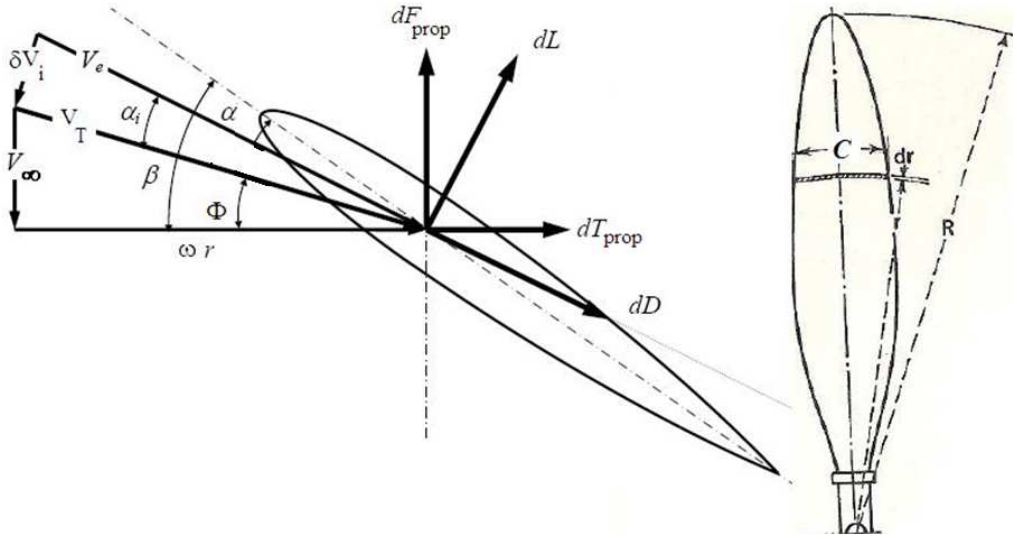

Figure 62. Velocity and Aerodynamic Forces on a Rotor Cross-Section

As shown on Figure 62, β is the local pitch angle at each rotor cross section. The pitch angle may or may not change along the radius of the rotor. Propeller pitch angles typically change along the blade, whereas helicopter rotors typically have a constant pitch angle. dF_{prop} is the thrust generated by the propeller blade element, and dT_{prop} is the lateral or "torque-force." In Figure 62 V_∞ is the forward airspeed of the rotor, ω is the angular velocity, and r is the local radius from the rotor hub to the blade element.

As a rotor turns the local section pushes air from the front of its rotation plane to the rear of the plane. The increase of velocity from fore to aft of the rotor is known as the induced velocity, V_i. Propeller momentum theory derives the relationship of the induced velocity to the total thrust produced by the propeller disk as

$$F_{prop} = 4 \cdot \left(\frac{\rho V_\infty^{\,2}}{2} \cdot A_{prop} \right) \left(1 + \frac{\delta V_i}{V_\infty} \right) \cdot \left(\frac{\delta V_i}{V_\infty} \right) \quad (19)$$

Differentiating this expression results in the incremental induced velocity in terms of the local thrust-force acting on the airfoil section

$$\delta V_i = -\frac{V_\infty}{2} \pm \sqrt{\left(\frac{V_\infty}{2} \right)^2 + \frac{dF_{prop}}{2 \cdot \rho \cdot 2\pi r \cdot dr}} \,. \quad (20)$$

The local induced angle of attack, shown on Figure 62, due to the induced velocity is

$$\alpha_i = \tan^{-1}\left(\frac{\delta V_i}{\sqrt{V_\infty{}^2 + (\omega \cdot r)^2}}\right) \tag{21}$$

The induced angle of attack is related to the local thrust and torque force by

$$\begin{aligned} dF_{prop} &= dL_{ift}\cos(\Phi+\alpha_i) - dD_{rag}\sin(\Phi+\alpha_i) \\ dT_{prop} &= dL_{ift}\sin(\Phi+\alpha_i) + dD_{rag}\cos(\Phi+\alpha_i) \end{aligned} \tag{22}$$

In Eq. (22) Φ is the blade helix angle, and is given by

$$\begin{aligned} \underline{\text{blade angle}} &= \underline{\text{Helix angle}} + \underline{\text{angle of attack}} \\ \beta &= \Phi + \alpha \end{aligned} \tag{23}$$

and

$$\alpha = \beta - (\alpha_i + \Phi) \tag{24}$$

Defining the sectional lift and drag coefficients as

$$\begin{aligned} dL_{ift} &= C_L \cdot \left(\frac{1}{2}\rho V_T{}^2\right)\cdot\left(\bar{C}_{(r)}\cdot dr\right) \\ dD_{rag} &= C_D \cdot \left(\frac{1}{2}\rho V_T{}^2\right)\cdot\left(\bar{C}_{(r)}\cdot dr\right) \end{aligned}, \tag{25}$$

and substituting into Eq. (22),

$$\begin{aligned} dF_{prop} &= \left(\frac{1}{2}\rho\left(V_\infty{}^2 + (\omega\cdot r)^2\right)\right)\times \\ &\left[C_L\cdot\cos(\Phi+\alpha_i) - C_D\cdot\sin(\Phi+\alpha_i)\right]\left(\bar{C}_{(r)}\cdot dr\right) \\ dT_{prop} &= \left(\frac{1}{2}\rho\left(V_\infty{}^2 + (\omega\cdot r)^2\right)\right)\times \\ &\left[C_D\cdot\cos(\Phi+\alpha_i) + C_L\cdot\sin(\Phi+\alpha_i)\right]\left(\bar{C}_{(r)}\cdot dr\right) \end{aligned} \tag{26}$$

Eqs (20)-(26) form a non-linear set of equations that are solved numerically to calculate the thrust and torque force on the blade section. The total thrust for the entire rotor is then calculated by integrating along the length of the blade

$$\begin{aligned} F_{prop} &= \\ &\frac{N\cdot\rho}{2}\left\{\int_0^R \left(V_\infty{}^2 + (\omega\cdot r)^2\right)\times \left[C_L\cdot\cos(\Phi+\alpha_i) - C_D\cdot\sin(\Phi+\alpha_i)\right]\left(\bar{C}_{(r)}\cdot dr\right)\right\} \\ T_{prop} &= \\ &\frac{N\cdot\rho}{2}\left\{\int_0^R \left(V_\infty{}^2 + (\omega\cdot r)^2\right)\times \left[C_D\cdot\cos(\Phi+\alpha_i) + C_L\cdot\sin(\Phi+\alpha_i)\right]\left(\bar{C}_{(r)}\cdot dr\right)\right\} \end{aligned} \tag{27}$$

In Eqs. (25)–(27) $\bar{C}_{(r)}$ is the local chord thickness, N is the number of blades on the rotor *(typically 2)*,and V_T is defined in Figure 62. The braking (direct drive) power of the rotor is given by

$$P_{brake} = \tau_{prop}\cdot\omega = \int dT_{prop}\cdot r\cdot\omega. \tag{28}$$

Consequently

$$\begin{aligned} P_{brake} &= \\ &\frac{N\cdot\rho}{2}\left\{\int_0^R \omega\cdot r\cdot\left(V_\infty{}^2 + (\omega\cdot r)^2\right)\times \left[C_D\cdot\cos(\Phi+\alpha_i) + C_L\cdot\sin(\Phi+\alpha_i)\right]\left(\bar{C}_{(r)}\cdot dr\right)\right\} \end{aligned}. \tag{29}$$

FF. Linear Airfoil Theory

Geenerally the lift and drag characteristics of hobby-class rotor and propellers are ill-defined, and the lift and drag coefficients are estimated using linear airfoil theory.[33] For the thin un-cambered rotors used in this project, the linear airfoil theory produces accurate results. Figure 63 shows typical lift and drag curves for a symmetrical airfoil. Linear airfoil theory is valid in the region where the slope of the lift coefficient curve is a straight line --before the blade stall point.

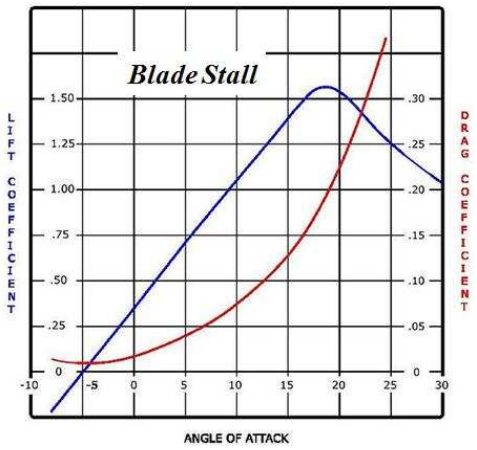

Figure 63. Typical Lift/Drag Coefficient Profile.

From linear-airfoil theory for an un-cambered (symmetrical) blade the lift coefficient is approximated by

$$C_L = C_{L_0} + \frac{\partial C_L}{\partial \alpha} \cdot \alpha \approx 2\pi \cdot \alpha_{radians} \ . \quad (29)$$

The drag coefficient is give by linear airfoil theory as

$$C_D = C_{D_0} + \frac{C_L{}^2}{\pi \cdot \varepsilon \cdot AR} \quad . \quad (30)$$

In Eq. (3) the Oswald efficiency factor ε, accounts for a finite wing span and typically varies from 0.85 to 0.95. This value is user selectable as an input to the program. *AR* is the aspect ratio of a single rotor blade. The parasite/skin drag coefficient, C_{D_0} is estimated using simple compressibility-adjusted, flat-plate skin-friction models (Ref. 16). The parasite drag coefficient is also a user selectable input to the code.

Figure 64 shows the typical blade dimensional inputs needed to perform an analysis. Either a fixed-pitch or variable pitch blades can be analyzed. The blade pitch angle inputs are input as tables to the code. Input operating conditions consist of incoming velocity, lateral velocity, rotor RPMs and altitude. As mentioned earlier, the Oswald efficiency factor and parasitic drag coefficient can also be input to the program. Figure 65 shows the tool used to measure the blade pitch angle distribution.

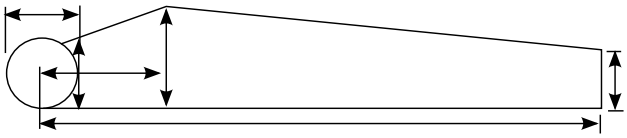

Figure 64. Generic shape of analyzed blades and dimensions required for input into

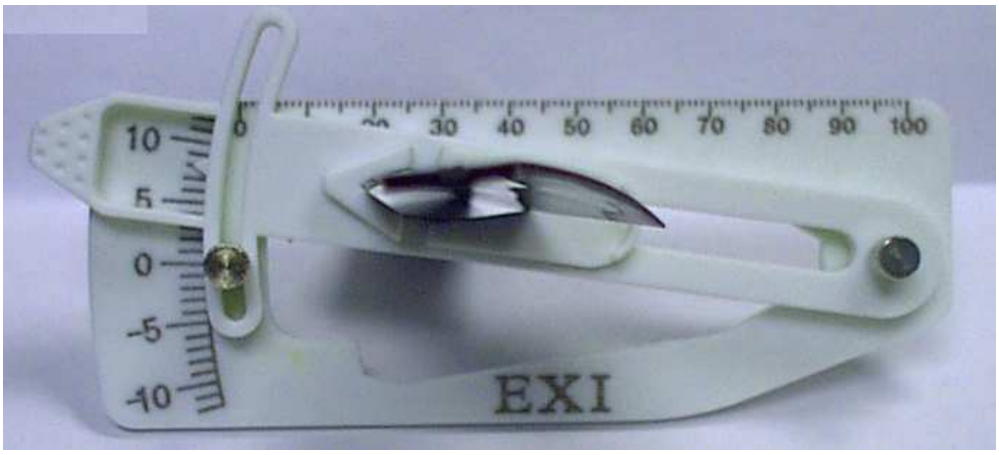

Figure 65. Rotor Pitch Blade Measurement Tool.

X. References

1 "Criteria for Accrediting Engineering Programs, 2008-2009, ABET Engineering Accreditation Commission," http://www.abet.org/Linked Documents-UPDATE/Criteria and PP/E001 0809 EAC Criteria 12-04-07.pdf, [retrieved September 4, 2008].

2 O'Bryan, T. C., and Hewes, D. E., "Operational Features of the Langley Lunar Landing Research Facility," NASA TN D-3828, 1967.

3 Nassiff, S. H., and Armstrong, N. A., "Apollo Flight Crew training in Lunar landing Simulators, AIAA Paper 68-254, Presented at the AIAA 2nd Flight Test, Simulation, and Support Conference, Los Angeles, CA, March 25-27, 1968.

4 Matranga, G. J., Ottinger, C. W., Jarvis, C. R., and Gelzer, D. C., "Unconventional, Contrary, and Ugly: The Lunar Landing Research Vehicle," NASA SP-2004-4535, 2005.

5 Ottinger, D/. W., ed., "Go For Lunar Landing Conference: From Terminal Descent to Touchdown," March 4th and 5th, 2008

Tempe, AZ, http://ser.sese.asu.edu/GO/, [cited 14 June 2010].

6 "Design and Testing of a Demonstration Prototype for Lunar/Planetary Surface Landing Research Vehicle (LPLSRV)," http://www.neng.usu.edu/classes/mae/5900/frameset_for_design_class_webpage, [retrieved 10 April, 2010].

7 "LPSRV, Revision 1396," LPLSRV Documents archival site, http://chimaera.usu.edu/svn/lpsrv/, [retrieved 10 April 2010].

8 John Kelly, Director of Exploration Projects, NASA Dryden Flight Research Center, Lunar Lander Training Vehicle Trade Study, Interim Report, October 10, 2008.

9 Strickland, S., "Apollo Lunar Descent and Ascent Trajectories", NASA technical memorandum, NASA TM X-58040, March 1970, AIAA 8th Aerospace Sciences Meeting, NY, NY, 19-21 January, 1970

10 Sellers, J., J., Understanding Space: An Introduction to Astronautics, 3rd Ed, McGraw-Hill, 2005.

11 Anon., "Volume I: Concept Development to Vehicle Integration and Testing," http://chimaera.usu.edu/svn/lpsrv/Final_Paper/LPSLRV_Final_Paper.doc, [retrieved 7 June 2010].

12 "Hyperworks, A Platform for Innovation," Altair Engineering, http://www.altairhyperworks.com, [retrieved 10 April 2008].

13 "Rhino Turbine," Jet Central Inc., http://www.jetcentral.com.mx/english/rhino.html, [retrieved 10 April 2010].

14 "NACA Airfoil Series," Aerospace Web, http://www.aerospaceweb.org/question/airfoils/q0041.shtml, [retrieved 7 June, 2010].

15 Drela, M., "XFOIL: An Analysis and Design System for Low Reynolds Number Airfoils," Proceedings from the Conference on Low Reynolds Number Airfoil Aerodynamics, University of Notre Dame, June 1989.

16 Sommer, S.C., and Short, B.J., "Free-Flight Measurements of Turbulent Boundary-Layer Skin Friction in the Presence of Severe Aerodynamic Heating at Mach Numbers From 2.8 to 7.0," NACA TN-3391, March, 1955.

17 "3DM-GX3-25, Miniature Attitude, heading Reference SWystem (AHRS), MicroStrain Inc., http://www.microstrain.com/3dm-gx3-25.aspx, [retrieved 8 June 2010].

18 Franklin, G. F., and Powell, J. D., Digital Control of Dynamic Systems, Addison Wesely Publishing Co. Inc., 1980, Chapt. 3.

19 "Gumstix, Dream, Design, Deliver," Gumstix, Inc., http://www.gumstix.com, [retrieved 10 April 2010].

20 "NI Labview," National Instruments, http://www.ni.com/labview, [retrieved 8 June 2010].

21 Prouty, R. W., Helicopter Performance, Stability, and Control, Krieger Publishing Company, Malabar, FL, 1990.

22 Hoffmann, G. M., Huang, H., Waslander, S. L., and Tomlin, C. J., "Quadrotor Helicopter Flight Dynamics and Control: Theory and Experiment," AIAA 2007-6461, AIAA Guidance, Navigation and Control Conference and Exhibit, Hilton Head, South Carolina. 20 - 23 August 2007.

23 Calvert, N., Basore, et. al., Design and Testing of a Quadrotor Aircraft, Senior Design Project Final Re[port, University of Colorado, Boulder, CO, 2008, http://aeroprojects.colorado.edu/08_09/valasaraptor/AIAA/AIAA_VALASARAPTOR.pdf, [retrieved 8 June 2010.]

24 APC Model Airplane Propellers, APC Corp, http://www.apcprop.com/v/index.html, [retrieved 8 June 2010].

25 "Hacker Brushless Motors," http://www.hacker-motor.com, [retrieved 9 June 2010].

26 Sapp, G., "Quadpower Precision Control Systems," http://www.quadpowered.com, [retrieved 9 June 2010].

27 "Hyperworks, A Platform for Innovation," Altair Engineering, http://www.altairhyperworks.com, [retrieved 10 June 2010].

28 "ThinPot Linear Position Sensor," http://mouser.com/catalog/specsheets/THINPOT_DATASHEET_REV_A1.pdf, [cited 18 June 2010].

29 McManis, C., "H-Bridges: Theory and Practice," http://www.mcmanis.com/chuck/robotics/tutorial/h-bridge/index.html, [cited 19 June 2010].

30 Beckwith, T. G., Marangoni, R. D., and Lienhard V, J. H., Mechanical Measurements, 6th Ed., Prentice Hall, 2006, pp.43-73.

31 Wolowicz, C. H., and Yancey, R. B., "Experimental Determination of Airplane Mass and Inertial Characteristics," NASA TR R-433, October 1974.

32 McCormick, B. W., Jr., "Aerodynamics of V/STOL Flight," Dover Publications, Inc., Mineola, NY, 1999, pp. 73-92.

33 Kuethe, A. M., and Chow, C. Y., Foundations of Aerodynamics: Bases of Aerodynamics design, 3rd ed.," John Wiley & Sons, Inc., New York, 1976, Chapt. 5.


NASA